Clarkson University

SIZE AND SHAPE OF UNIFORM PARTICLES PRECIPITATED IN HOMOGENEOUS SOLUTIONS

a dissertation

by

Igor V. Sevonkaev

department of physics

submitted in partial fulfillment of the requirements

for the degree of

doctor of philosophy

(Physics)

November 2009

Accepted by the Graduate School

Date DEAN

Abstract

The assembly of nanosize crystals into larger uniform colloids is a fundamental process that plays a critical role in the formation of a very broad range of fine-particles used in numerous applications in technology, medicine, and national security. It is widely accepted that, along with size, in most of these applications the shape of the particles represents a critical factor. In the current research, we investigate the size and shape control of uniform particles prepared by precipitation in homogeneous solutions.

In the first – theoretical – part a combinational mechanism of the shape control during particle growth was proposed and analyzed numerically. The main finding of our simulation is that a proper balance of two processes, preferential attachment of transported monomers at the protruding features of the growing cluster and monomer rearrangement at the cluster surface, can yield a well-defined particle shape that persist for sizes much larger than the original seed over a large interval of time.

In the experimental part, three chemically simple systems were selected MgF_2, $NaMgF_3$, and PbS for defining and evaluating the key parameters of the shape and size control of the precipitates. Thus, uniform dispersions of particles of different morphologies (spherical, cubic, platelet, and prismatic) were prepared by precipitation in aqueous solutions. The mechanisms of the formation of the resulting particles of different shapes are explained by the role of the pH, temperature, solubility, and ionic strength. Stages of particles growth were evaluated on short and long time scales,

which allowed to propose multistage mechanisms of $NaMgF_3$ growth and estimate induction time and critical nuclei size for MgF_2.

In addition, for prospective numerical modeling the surface tensions of spherical and platelet particles of MgF_2 were evaluated from the X-ray data by a lattice parameter change method.

Also, a new method for the evaluation of the variation in the density distribution in colloidal spherical particles was proposed. This method utilizes transmission electron microscopy without high resolution mode and processes acquired images. Suggested method eliminates the dependency of the image contrast on sample crystallinity. The advantage of such approach manifested by the short time sample preparation, fast instrument tune-up, rapid image acquisition and analysis, all of which shortens the processing time.

Acknowledgements

I am indebted to my advisors: Professor Egon Matijević and Professor Vladimir Privman for their guidance, wisdom, and support.

I am grateful to Professor Dan Goia for contributing valuable insights to my thesis work, and Professor Dipankar Roy and Professor Igor Sokolov for serving on the committee and fruitful comments on this study.

I also greatly appreciate useful discussions with professor David Morrison, who helped me to understand many aspects related to TEM and electron diffraction techniques. Many aspects of this study were discussed with Dr. Leonid Fedichkin, and Dr. Daniel T. Robb , also I appreciate technical support as from William and Christopher Plunkett as well as from Ted Champagne (a fair amount of all images has been taken with their help).

I gratefully acknowledge support of this research by the NSF under grant DMR-0509104, and earlier support under grant DMR-0102644.

Clarkson University Igor Sevonkaev November 11, 2009

Contents

List of Figures

List of Tables

Nomenclature

TEM	Transmission electron microscopy
SEM	Scanning electron microscopy
BF TEM	Bright field TEM
DF TEM	Dark field TEM
XRD	X-ray diffraction
SC	Simple cubic crystal lattice structure
BCC	Body-centered cubic crystal lattice structure
FCC	Face-centerd cubic crystal lattice structure
HCP	Hexagonal close-packed crystal lattice structure
PDF	Powder diffraction file
BSE	Back scattered electrons
AE	Auger electrons
LLE	Low loss electrons
SE	Secondary electrons

Chapter 1

General Introduction

1.1 Field overview

Initially colloid chemistry started only as a chapter of physical chemistry and over the decades developed into self-contained discipline that interprets experimental observations, measurements, and data. As a matter of fact, such empirical approach for solving practical challenges represents a gigantic benefit to the modern industry. Nowadays it is almost impossible to imagine a single industrial process that does not require any knowledge of colloid science.

Although colloid science as distinct branch originated only about 100 years ago, the properties of colloids were used by craftsmen for much longer time. Dying, coating of the surfaces, leather treatment — all of these were utilized by humans since the beginning of the times. However, since eighteenth century scientists had started to devote their interest to the characteristic properties of colloids. Thus, in 1745–1755 M. Lomonosov studied crystallization of colored glasses made with dispersions of metals., in 1777 C. Scheele and F. Fontana independently from each other discovered gas adsorption, and later, in 1785 T. Loviz discovered adsorption from the liquids,

and P. Laplace in 1806 acquired qualitative results for capillary effects.

In the 1840s, the Italian scientist F. Selmi noticed abnormal behavior of some solutions, which nowadays are considered colloidal systems. Solutions that were investigated by Selmi could strongly disperse light, cause precipitation by admixing even small amounts of salts that would not react chemically with the solution, precipitation and re-dispersing of a sediment did not cause any volume or temperature change (with is relevant in cases of formation and dissolution of crystalline materials). Selmi named such solutions "pseudosolutions", which were afterwards called *sols*.

Later – the middle of the nineteenth century – Thomas Graham was the first who performed broad solid and systematic study on the sols described by Selmi. Because Graham saw an analogy between such sols and typical glue ($\kappa o\lambda\lambda\alpha$ – in Greek) he named the solutions *colloids*. Needless to say, that his contribution in the field was Brobdingnagian. Thus, by the end of 1860s Graham differentiated many important properties that were specific only to colloids, such as:

1. All colloidal dispersions strongly disperse light – *opalize*. First the method was proposed by Tyndall (which thereafter was called the Tyndall effect). The principle of this method is in the shining of a converging beam of light through the dispersion while observing the opalization from the side. Intensive opalization reflects a strong evidence of the presence of multiple phases in the dispersion.

2. Diffusion of the colloidal particles in the solutions is a very tedious process.

3. Colloidal dispersions have very small osmotic pressure, which in some instance may be below an instrument's sensitivity.

4. Colloidal dispersions are favorable to the dialysis, in other words, with the semipermeability membrane they may be separated from the dopants of lower molar weight.

5. Colloidal dispersions are favorable to coagulation, which means that dispersed particles may easily aggregate under insignificant influence of external parameters.

6. Colloidal dispersions *almost* always display electrophoresis (particle transport towards preferred electrode).

Before the beginning of 20th century speculations about the structures of colloidal systems were based mostly on indirect experiments, due to the absence of appropriate tools and methods for the observation of fine particles in the solutions. Only when R. Zsigmondy and H. Siedentopf developed the ultramicroscope in 1903 it became possible to measure particles size distribution in the sols and consequently support theoretical model of Brownian motion developed by A. Einstein and M. Smoluchowski in 1905. Further investigations by Zsigmondy, Perrin, and Swedberg showed a strong correlation between properties of the colloidal systems and sizes of the dispersed particles. Thus, the size of the particles influences on the intensity of the Brownian motion, speed of sedimentation, and optical properties of a colloidal system.

Although, the new science was fully established by the beginning of the twenties century and obtained its mathematical substantiation in 1937 by B. Derjaguin, L. Landau, E. Verwey, and T. Overbeek theory [1], more improvements have been done to it based on newer empirical data and numerical opportunities. One of such developments was proposed by Barouch and Matijević [2, 3], which considers double-layer correction in interactions of unequal spheres, in contrast to the classical case of two parallel plates. In that study it was shown that the electrostatic energy decreases owing to the fact that a portion of the surfaces may be attractive even though the rest of the surfaces may be repulsive. That effect depends on the separation, as well as on the difference in the potentials and the sizes of the two spherical particles.

The major result of that finding was a substantial decrease in the peak height of the total interaction energy [3], which brought the theory and the experiment into closer agreement than the classical model.

1.2 Problem formulation

Properties of matter such as surface reactivity, magnetism, ductility, and conductivity are highly important in numerous applications. Understanding coarsening behavior and morphology evolution is critical for efficient material synthesis and quality control [4, 5].

Over the past several decades, a large number of dispersions consisting of uniform particles of simple and composite nature have been reported in literature [6–8]. In principle, the most versatile method to produce such dispersions is by precipitation in solutions. This process may involve different mechanisms of their formation such as polymerization [9] of solutes in solution, by diffusional growth [6] following the nucleation stage [10], or by aggregation of preformed nanosize precursors [9].

Many research groups [11–21] have tried to analyze different models of uniform particle formation, such as cadmium sulfide [11], titanium oxide [14], copper chloride [15], platinum [16], palladium [17], gold [18], iron oxide (α-Fe_2O_3) [19], and developed molecular dynamic simulations of depositions nanoparticles in liquids [22]. Also there was much time devoted to studying the nanocrystalline particle growth [23–26] with theoretical explanation [27–30] and computer modeling [31–34]. It has been well established that many monodispersed colloids of different shapes prepared by precipitation are built from nanosize subunits [6, 11]. Currently, there are two accepted mechanisms for the formation of uniform particles: aggregation of primary precursors [12,18,35] and, in contrast, growth of the nuclei by the attachment of constituent

solutes [10]. Some attempts in explanation of the mechanisms of growth of uniform colloid particles were done by S. Libert, *et. al.* [11].

One of the challenges in fine particle science is the prediction of their shape by precipitation in homogeneous solutions, which is possible to do in a limited number of cases. For example, amorphous spherical particles result as a rule by the polymerization of constituent solutes, such as in the hydrolysis of multivalent cations [9]. Furthermore, in some cases diffusion process may produce uniform crystals of a given habit characteristic of a given mineral. Particularly intriguing are processes where uniform colloidal particles are formed by aggregation, which can yield particles of different shapes including spheres. It is noteworthy that it has been proven the aggregation process to be more common than originally anticipated. A model was proposed that explains size selection of uniform polycrystalline spheres obtained by aggregation [12] and tested on examples of gold [18] and cadmium sulfide [11]. In contrast, there are no models available to explain the shape of particles different than spheres. The task is more difficult when particles of the same chemical composition could be produced in different shapes just by varying experimental conditions, such as the concentrations of the reactants. It was shown at least in the case of hematite ((α-Fe_2O_3) [36]) that the final particles' habit was related to the shape of the nanosize precursors [37], but no such relationship was found in other systems [38].

To evaluate these effects, it is necessary to deal with well-defined dispersions of fine particles. While different techniques have been used in the preparation of uniform particles, the precipitation in homogeneous solutions is advantageous, because of the experimental simplicity and versatility. The comprehensive volume, edited by Sugimoto [6], describes many such simple and composite finely dispersed matter of various shapes, modal sizes, and of different structures.

While the progress in the ability to obtain these materials is quite impressive, much

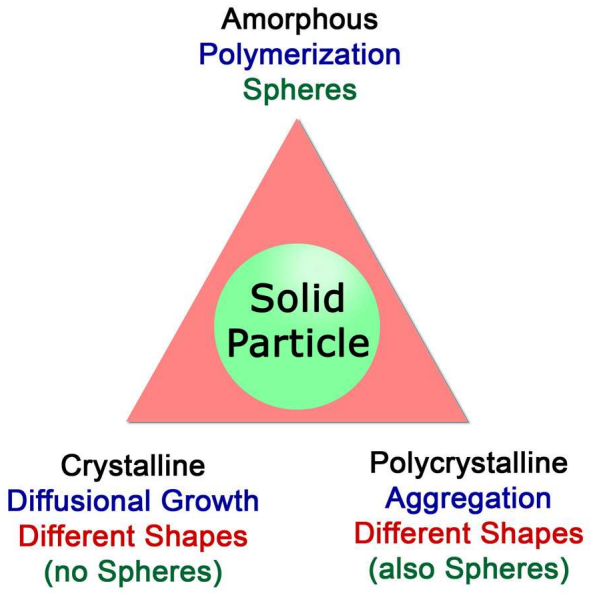

Figure 1.1: Schematic classification of mechanisms of particles formation [9]

less successful have been efforts to elucidate the mechanisms of their formation. As a result, the preparation of dispersions of specific chemical and physical characteristics still depends, to a great extant, on the skills of the experimentalists. The reason for this uncertainty is easily understood, because the properties of precipitated products are affected in a sensitive way on the complexation of the reactants in the liquid media. The latter may vary with the experimental parameters, including the concentration, solubility, pH, temperature, aging, additives (such as stabilizers), all of which also depend on the solvent used.

By considering a large number of reported "monodispersed" colloids [39–53], and taking into account specific preparation conditions, a general classification of mechanisms of particle formations was proposed [9], which is schematically given in Fig. 1.1.

The top of the triangle represents processes, in which the particles are formed by polymerization of solute monomers, as in the example of silica, produced by condensation of silicic acid molecules. In such cases the resulting particles are, as a rule,

amorphous spheres.

The left side of the triangle refers to the formation of particles by diffusion of constituent solutes onto nuclei. These precipitates appear as crystals of different shapes, except spherical, and can be uniform under certain conditions.

Finally, the right-hand side of the scheme refers to the mechanism, by which the final particles are made of small (nanosize) entities, which are formed first and subsequently aggregate to a larger size [7, 9, 54, 55]. This process can yield uniform particles of different shapes including spheres. There is ample experimental evidence demonstrating that great many dispersions of larger particles are formed by this process.

It is, therefore, of further interest to investigate the multistage growth mechanism, as it can yield particles of any shape. It is also an intriguing task to explain how countless small precursors can form identical large particles of a given shape. A model, which accounts for the formation of uniform spheres by aggregation, was developed and successfully tested for dispersions of metals and salts [7, 11, 12, 56, 57]. Still the size selection of particles of different shapes by aggregation remains an unresolved problem, presenting many challenges. To understand these complex issues, it is desirable to obtain experimental data on solids of simple chemical composition. It is also important that constituent ions show little tendency for complexion in reacting solution, and yield uniform particles of well defined shapes.

In order to develop some understanding of the shape produced by such a complex mechanism, it is necessary to examine the formation of dispersions of particles of a given shape carefully. It is also essential that such particles be of simple chemical composition, in order to avoid difficulties that occur when precipitation takes place in solutions of multiple solute complexes. Dealing with $NaMgF_3$, MgF_2, and PbS particles, fulfills the described conditions. The constituent ions do not form complexes

in aqueous solutions (except may be at higher pH), and the final products have rather simple crystalline structures. Furthermore, depending on the experimental conditions, the particles may appear in different shapes (spherical, cubic, prismatic, or plate-like), by mechanisms given in Fig. 1.1.

In addition, there is a permanent interest in multicomponent fluoride mixtures from the industrial sector. A high enthalpy of transformation per unit mass of fluoride systems appear to be perfect latent thermal storage materials [58, 59]. The potential applications of such mixtures are found, for example, in the space programs to provide electric power from solar thermal energy [60].

It is expected that this research could be helpful in clarifying some of the critical parameters applicable for the future theoretical models and numerical simulations of growth of well-defined particles.

1.3 Structure of this thesis

Current thesis is divided into several principal parts. First part is devoted to the introduction into the topic, evaluation of theoretical achievements, and recent theoretical model development in our group. In the second part, experimental segment of the research is depicted such as sample preparation, data acquisition, and material characterization methods. In the third part, the most essential results and conclusions of the present work are gathered. Final part concludes overall achievements of this study. The last chapter describes the design of a novel method, which was developed for the analysis of density distribution in spherical colloidal particles. In addition, all supplemental material such as C++ scripts, Excel and Origin files may be found on the enclosed DVD.

Chapter 2

Theoretical Background

2.1 Review of crystal growth theories

2.1.1 Homogeneous nucleation

Although practically every book on crystal growth [61–63] widely covers the nature and principles of primary nucleation, it is essential to summarize the most important aspects of homogeneous nucleation for further discussions in this study. Thus, in order to treat the nucleation phenomenon quantitatively, it is necessary to have some clear idea of the nature of the nucleus preceding crystal formation. In general, there are two mathematical analyses of nucleation, which are quite different. The first case may be represented in terms of a classical formulation resembling that proposed by Volmer and others; the second requires a nonclassical analysis which might be treated by kinetic or thermodynamic reasoning. Current discussion, however, will be limited to traditional theory of nucleation.

If a small, stationary, spherical nucleus of diameter l is created from immobile ions, the change in energy of the system is related to the ion "bonds" formed, leading to a heat of crystallization (negative) and the energy required to create the surface.

The standard free energy change may be represented approximately by

$$\Delta G^0 = \pi l^3 \Delta G_v/6 + \pi l^2 \sigma_{CL} \tag{2.1}$$

where ΔG_v is the volume free energy resulting from bond formation (and hence, by convention, is negative in sign), l is the nucleus size and σ_{CL} is the inter-facial energy per unit area of surface (Changes in the chemical composition of the system are typically deemed negligible.)

For large nuclei the volume term predominates; for small nuclei it is the surface term that predominates. Consequently, the maximum ΔG_0 with respect to l is given for a cubic nucleus by:

$$\Delta G^* = \pi l^2 \sigma_{CL}/3 = \frac{16\pi\sigma_{CL}^3}{3\Delta G_v^2} \tag{2.2}$$

where ΔG^* is the activation energy barrier to the nucleation process.

The volume free energy, ΔG_v, is obtained from the Gibbs-Kelvin equation as

$$\Delta G_v = \frac{mkT}{v} \ln s = \frac{4\sigma_{CL}}{l} \tag{2.3}$$

where m is the number of ions in the neutral molecule, v is the molecular volume, and s is the supersaturation. Hence

$$\Delta G^* = \frac{16\pi\sigma_{CL}^3 v^2}{3(mkT \ln s^*)^2} \tag{2.4}$$

In this manner it is possible to relate the activation energy barrier to the supersaturation, s.

Some of the difficulties in applying this treatment to real situations are often

glossed over. It is normally recognized that the interfacial energy σ_{CL} is not necessarily independent of cluster size, but less familiar is the fact that extra thermodynamic terms involving rotation, vibration, and translation of the clusters become rather important for small clusters. Changes in chemical composition of the system should also be considered. For small clusters the Gibbs-Kelvin equation (Eq. 2.3) is modified to

$$\Delta G_v = \frac{4\sigma_{CL}}{l} - \frac{1}{n} \tag{2.5}$$

where n is the number of molecules or ions in the cluster corresponding to ΔG^*. Furthermore, it seems unlikely that very small clusters can maintain thermodynamic equilibrium without gross fluctuations in σ_{CL}. These criticisms will be seen to be of importance when experimental precipitation data are examined.

The rate of nucleation dN/dt is usually written in the form (derived from the law of mass action)

$$dN/dt = J = A \exp[-\Delta G^0/kT] \tag{2.6}$$

or, from Eq. 2.4

$$J = A \exp[\frac{16\pi\sigma_{CL}^3 v^2}{3(mkT \ln s^*)^2}] \tag{2.7}$$

If J is plotted as a function of supersaturation, it can be seen that there is in essence a critical supersaturation, s^*, below which nucleation is very slow and above which nucleation is extremely fast. This critical supersaturation is usually chosen to correspond to a rate of one nucleus being formed per second per unit volume, in which case Eq. 2.7 becomes

$$\ln s^* = [\frac{32\sigma_{CL}^3 v^2}{m^2 k^3 T^3 \ln A}]^{1/2} \tag{2.8}$$

If the preexponential factor A is known, it is clear that the only unknown in Eq. 2.8 is the interfacial energy, σ_{CL}. Actually A can be resolved into a fairly complicated expression, but for present purposes it can be taken to be equal to 10^{25}. The theory predicts, then, a critical supersaturation s^* from which σ_{CL} can be calculated.

2.1.2 Surface energy theory

An isolated droplet of a fluid is most stable when its surface free energy, and thus its area, is a minimum. In 1878 Gibbs suggested that the growth of a crystal could be considered as a special case of this principle: the total free energy of a crystal in equilibrium with its surroundings at constant temperature and pressure would be a minimum for a given volume. If the volume free energy per unit volume is assumed to be constant throughout the crystal, then

$$\sum a_i g_i = minimum \tag{2.9}$$

where a_i is the area of the ith face of a crystal bounded by n faces, and g_i the surface free energy per unit area of the ith face. Therefore, if a crystal is allowed to grow in a supersaturated medium, it should develop into an "equilibrium" shape, i.e. the development of the various faces should be in such a manner as to ensure that the whole crystal has a minimum total surface free energy for a given volume. Of course, a liquid droplet is very different from a crystalline particle; in the former the constituent atoms or molecules are randomly dispersed, whereas in the latter they are regularly located in a lattice structure. Gibbs was fully aware of the limitations of his simple analogy, but in 1885 Curie found it a useful starting point for an attempt to evolve a general theory of crystal growth and in 1901 Wulff showed that the equilibrium shape of a crystal is related to the free energies of the faces. He suggested that the crystal

faces would grow at rates proportional to their respective surface energies.

The surface energy and the rate of growth of a face, however, should be inversely proportional to the reticular or lattice density of the respective lattice plane, so that faces having low reticular densities would grow rapidly and eventually disappear. In other words, high index faces grow faster than low.

In practice, a crystal does not always maintain geometric similarity during growth; the smaller, faster-growing faces are often eliminated, and this mode of crystal growth is known as "overlapping". Fig. 2.1 shows the various stages of growth of such a crystal. The smaller B faces, which grow much faster than the A faces, gradually disappear from the pattern.

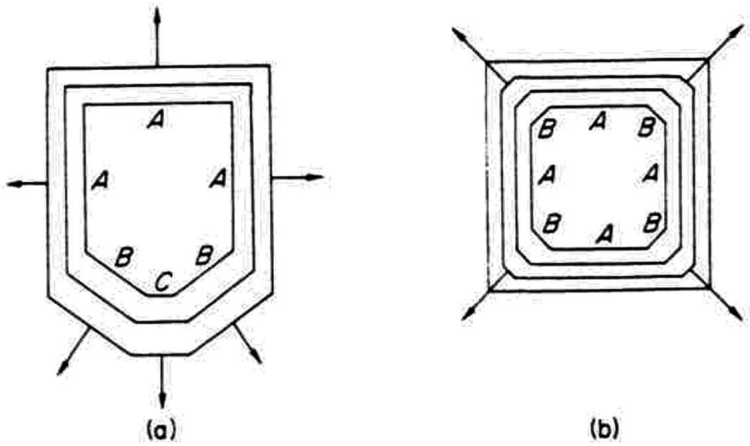

Figure 2.1: Velocities of crystal growth faces: (a) invariant crystal; (b) overlapping [61]

So far there is no general acceptance of the surface energy theories of crystal growth, since there is little quantitative evidence to support them. These theories, however, still continue to attract attention, but their main defect is their failure to explain the well-known effects of supersaturation and solution movement on the

crystal growth rate.

2.1.3 Adsorption layer theory

The concept of a crystal growth mechanism based on the existence of an adsorbed layer of solute atoms or molecules on a crystal face was first suggested by Volmer (1939). Volmer's theory is based on thermodynamic reasoning. When units of the crystallizing substance arrive at the crystal face they are not immediately integrated into the lattice, but merely lose one degree of freedom and are free to migrate over the crystal face (surface diffusion). There will, therefore, be a loosely adsorbed layer of integrating units at the interface, and a dynamic equilibrium is established between this layer and the bulk solution. The adsorption layer plays an important role in crystal growth and secondary nucleation. The thickness of the adsorption layer probably does not exceed 10 nm, and may even be nearer 1 nm.

Atoms, ions or molecules will link into the lattice in positions where the attractive forces are greatest, i.e. at the "active-centers", and under ideal conditions this stepwise build-up will continue until the whole plane face is completed. Before the crystal face can continue to grow, i.e. before a further layer can commence, a "center of crystallization" must come into existence on the plane surface, and in the Volmer theory it is suggested that a monolayer island nucleus, usually called a two-dimensional nucleus, is created.

Expressions for the energy requirement of two-dimensional nucleation and the critical size of a two-dimensional nucleus may be derived in a similar manner to those for homogeneous three-dimensional nucleation, yielding:

$$\Delta G_{crit} = \frac{\pi h \sigma_{CL}^2 v}{kT \ln s} \tag{2.10}$$

where v is a volume of a nucleus and h its thickness.

The rate of two-dimensional nucleation, J, can be expressed in the form of the Arrhenius reaction velocity equation:

$$J = B \exp[-\frac{\pi h v \sigma_{CL}^2}{k^2 T^2 \ln s}] \tag{2.11}$$

The Kossel (1934) model of a growing crystal face envisages that an apparently flat crystal surface is in fact made up of moving layers (steps) of monatomic height, which may contain one or more kinks. Growth units are most easily incorporated into the crystal at a kink; the kink moves along the step and the face is eventually completed. A fresh step could be created by surface nucleation, and this frequently commences at the corners.

Frank (1949) postulated that few crystals ever grow in the ideal layer-by-layer fashion without some imperfection occurring in the pattern. Most crystals contain dislocations, which cause steps to be formed on the faces and promote growth. Of these the screw dislocation is considered to be important for crystal growth, since it obviates the necessity for surface nucleation. Once a screw dislocation has been formed, the crystal face can grow perpetually "up a spiral staircase." Quite often very complex spirals develop, especially when several screw dislocations grow together.

As a completely smooth face never appears under conditions of spiral growth, surface nucleation is not necessary and the crystal grows as if the surface were covered with kinks. Growth continues uninterrupted at near the maximum theoretical rate for the given level of supersaturation. The behavior of a crystal face with many dislocations is practically the same as that of a crystal face containing just one.

2.1.4 Diffusion theories

The origin of the diffusion theories dates back to the work of Noyes and Whitney (1897) who considered that the deposition of a solid on the face of a growing crystal was essentially a diffusional process. They also assumed that crystallization was the reverse of dissolution, and that the rates of both processes were governed by the difference between concentration at the solid surface and in the bulk of the solution. An equation for crystallization was proposed in the form

$$dm/dt = k_m A(c - c^*) \tag{2.12}$$

where m is a mass of solid deposited in time t, A is a surface area of the crystal, c is the solute concentration in the solution (supersaturated), c^* is the equilibrium saturation concentration, and k_m is the coefficient of mass transfer.

On the assumption that there would be a thin stagnant film of liquid adjacent to the growing crystal face, through which molecules of the solute would have to diffuse, Nernst (1904) modified equation 6.14 to the form

$$\frac{dm}{dt} = \frac{D}{\delta} A(c - c^*) \tag{2.13}$$

here D is the diffusion coefficient of the solute, and δ is the length of the diffusion path.

The thickness δ of the stagnant film would obviously depend on the relative solid-liquid velocity, i.e. on the degree of agitation of the system. Film thicknesses up to 150 μm have been measured on stationary crystals in stagnant aqueous solution, but the values drop rapidly to virtually zero in vigorously agitated systems. As the latter could imply an almost infinite rate of growth in agitated systems, it is obvious that the concept of film diffusion alone is not sufficient to explain the mechanism of crystal

growth. Furthermore, crystallization is not necessarily the reverse of dissolution. A substance generally dissolves at a faster rate than it crystallizes at, under the same conditions of temperature and concentration.

2.1.5 Kinematic theory

Two processes are involved in the layer growth of crystals: the generation of steps at some source on the crystal face followed by the movement of layers across the face. Consideration of the movement of macrosteps of unequal distance apart led Frank (1958) to develop a "kinematic" theory of crystal growth. The step velocity, u, depends on the proximity of the other steps since all steps are competing units. Thus

$$u = q/n \tag{2.14}$$

where q is the step flux (the number of steps passing a given point per unit time) and n is the step density (the number of steps per unit length in a given region). The distance between steps, $\lambda = n^{-1}$. The slope of the surface, p, with reference to the close packed surfaces is given by

$$p = \tan\theta = hn \tag{2.15}$$

and the face growth rate, v, normal to the reference surface by

$$v = hg = hnu \tag{2.16}$$

where $h$is the step height.

If the steps are far apart ($\theta \rightarrow 0$), and the diffusion fields do not interfere with one another, the velocity of each step, u, will be a maximum. As the step spacings

decrease and the slope increases, u decreases to a minimum at $hn = 1$ ($\theta = 45°$), in other words the face growth velocity v approaches a flat maximum and then decreases to zero.

2.1.6 Birth and spread theory

Several growth models based on crystal surface (two-dimensional) nucleation, followed by the spread of the monolayers have been developed by O'Hara and Reid, 1973; van der Eerden, Bennema and Cherepanova, 1978. As depicted in Fig. 2.2, growth develops from surface nucleation that can occur at the edges, corners and on the faces of a crystal. Further surface nuclei can develop on the monolayer nuclei as they spread across the crystal face.

The Birth and Spread model results in a face growth velocity-supersaturation relationship of the form

$$v = A_1 \sigma^{5/6} \exp(A_2/\sigma) \tag{2.17}$$

where A_1 and A_2 are system-related constants. Eq. 2.17 is interesting in that it describes the only growth model that allows a growth order, g, greater than 2.

2.1.7 Self-assembly of nanocrystals

In 1999 Privman, Goia, Park, and Matijević [12] proposed a model of formation of monodispersed colloids, which was significantly improved by subsequent studies [54, 55, 64]. The concept of this approach is that the nanoparticles are synthesized as nanocrystals by burst nucleation from solution with following self-assemblence by aggregation. The two kinetic processes are coupled, and both are driven by diffusional transport. The interrelation of the two processes allows for the formation of narrow size distribution colloid dispersions.

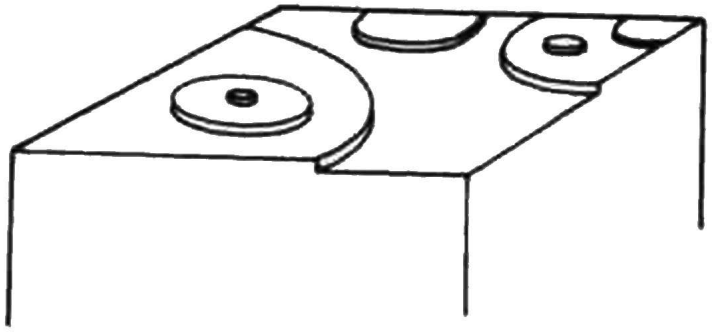

Figure 2.2: Development of polynuclear growth by the birth and spread mechanism [61]

Thus, employing assumption that the concentration of the solutes is depleted solely due to irreversible formation of the critical-size nuclei Privman [64] obtained the rate of supercritical particle production:

$$\rho(t) = \frac{32(\pi c)^2 a^3 \sigma D_a}{3kT \ln(c/c_0)} \exp[\frac{256(\pi a^2 \sigma)^3}{(3kT)^3 [ln(c/c_0)]^2}] \tag{2.18}$$

where D_a is the diffusion constant, a is a monomer size, σ is the surface tension of a crystal, c_0 is an equilibrium concentration of monomers, and c is a monomer concentration.

2.2 Modeling of particle shape formation

Introduction

In this section we address a long-standing problem in colloid and nanoparticle science: particle shape selection in solution synthesis [31, 65]. Our main finding is that a proper balance of two processes, preferential attachment of transported monomers at

the protruding features of the growing cluster and monomer rearrangement at the cluster surface, can yield a well-defined particle shape for a large interval of times, and persisting for sizes much larger than the original seed.

Precipitation in homogeneous solutions has been widely used in preparation of uniform particles because of its experimental versatility [9, 66–70]. Therefore, an important theoretical challenge has been to understand the mechanisms of diffusional growth of well-defined particles [6, 12, 29, 34, 54, 57, 64, 69, 71–85]. Specifically, first advances have been reported [9, 12, 64, 71] in understanding particle size selection, i.e., narrow size distribution in polycrystalline colloid synthesis by aggregation of nanosize precursors and in nanoparticle formation by burst nucleation.

Particle shape selection, however, has not been generally understood. The main difficulty has been classifying and modeling the relevant dynamical processes that combine to yield the shape and morphology. Specifically, in properly designed experiments [9, 66–70], evenly proportioned polycrystalline colloids were obtained with faces corresponding to densely-packed, low-index crystal planes [65].

Several dynamical processes play a role in fast growth by aggregation of diffusionally transported monomers. These include monomer diffusion in solution, their attachment at and detachment from the growing cluster surface, and monomer motion on the surface. The latter process, as well as detachment-reattachment, ultimately lead to the formation of a compact structures of density close to that of the bulk material. In addition, processes that involve more than a single cluster and transport of entities larger than monomers should also be accounted for.

In this chapter we selected two key dynamical mechanisms: deposition of monomers at exact lattice locations defined by the original seed of cubic/square shape, and their rearrangement on the surface of the growing cluster [31]. The process of diffusional transport is replaced by an artificial mechanism of monomer flux with preferential

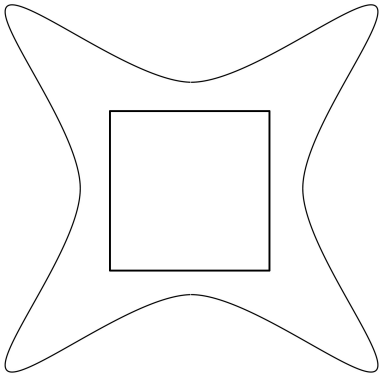

Figure 2.3: Gaussian Distribution Function with the peaks that correspond to the edges of the initial particle

attachment along directions of the seed corners. This approximation was tested in two and three dimensions (2d and 3d). A more sophisticated model with particle diffusion properly treated in a continuum 3d space, and with only the lattice structure imposed by the original seed, has recently been treated in [65]. The main conclusion of both studies has been that cluster growth without development of large defects can yield well-defined particle shapes.

2.2.1 Numerical approach

Our simulations were carried out by the standard Monte Carlo approach for 2d and 3d systems. The script was interpreted on C++, and operated with the implemented random number function *rand()*; the "seed" for this function was chosen as a computer timer (that eliminated reproducibility of random number generator). Tests of this function showed it to produce random data evenly.

The arriving monomers were assumed to deposit irreversibly at the cluster surface according to a Gaussian distribution function (GDF), (Fig. 2.3), simulated by a "polar coordinate" approach [86], with the standard deviation σ. The rate of rearrangement

of monomers at the surface vs. their deposition was controlled by the parameter ρ, defined below.

It is important to note that physical properties of the media and properties of particles motion were ignored in the current numerical model. Also, the surface of the initial seed particle can not be destroyed or rearranged during ongoing simulation. In addition to that, the movement of the deposited subunits is limited to the rectilinear trajectories with some random oscillations near them in the direction towards the center of the seed. Consequently, rearrangement of a building block may only happen when distance between selected unit and the center of the core is larger then the distance between its new position on the surface and the center of the seed. In other words, radius-vector of a building block may not increase under any circumstances. Thus, in the present model the effects of the properties of the media and of the monomer and cluster motion were concentrated on σ and ρ parameters.

2.2.2 2D modeling

For each choice of σ and ρ, a uniform random number $0 \leq r \leq 1$ is generated. For $r < \rho$, a new monomer is deposited at the surface of the cluster, at the polar direction selected according to the GDF. The motion of this monomer toward the center of the cluster is then carried out along a rectilinear trajectory (with random oscillations about it).

For $r > \rho$, a surface monomer, randomly selected from among those earlier deposited, was rearranged (transported) on the cluster surface by a similar process, until it either collided with another monomer or reached a position at the closest possible distance to the center.

The model was first tested in 2d, for a 6000×6000 square lattice. As a typical initial square seed we took a 28×28 particle, placed at the center of the space. After

space initialization, building blocks were generated at rate ρ with coordinates obtained from GDF. The simulations ran for 500,000 iterations. Three different values of σ and ρ (0.3, 0.5, 0.8), i.e., total 9 possible combinations, were tested. The results of 2d modeling with $\rho = 0.3$ are shown in Figs. 2.4, 2.5, and 2.6. As one can see from these figures, σ has a strong effect on formation of particles corners. Thus, $\sigma = 0.3$ independently from values of ρ forced square seed to grow into 4 petal object (Figs. 2.4(a), 2.5(a), 2.6(a)). On the other hand, $\sigma = 0.8$ was responsible for formation of circular particle (Figs. 2.4(c), 2.5(c), 2.6(c)). As seen in Figs. 2.4(b), 2.5(b), 2.6(b) for the case $\sigma = 0.5$, with a proper balance of the two dynamical processes the shape of the initial seed is maintained by the growing cluster up to a large size (as compared to the initial seed), over the simulation time scales.

The two balanced processes were represented by the deposition rate, which favors growth along the directions of the corners of the initial seed, and the rate of the on-surface motion which tends to smooth out the monomer arrangement, driving the cluster shape towards circular. If the processes are not balanced, then one of them "wins" and the cluster either growth protrusions along the preferred directions or becomes circular, as seen in Figure 2.4.

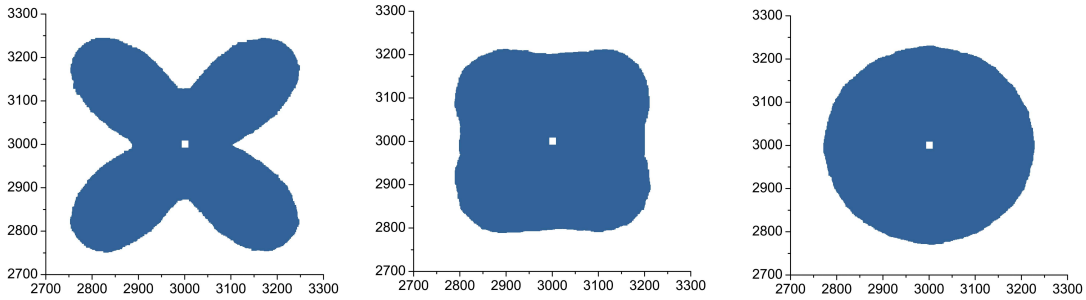

(a) $\sigma = 0.3$ and $\rho = 0.3$ (b) $\sigma = 0.5$ and $\rho = 0.3$ (c) $\sigma = 0.8$ and $\rho = 0.3$

Figure 2.4: Growth of two dimensional particles lasted for 500,000 iterations each, with different parameters of σ and $\rho = 0.3$. Note that white spot at the center of each plot represents initial square seed

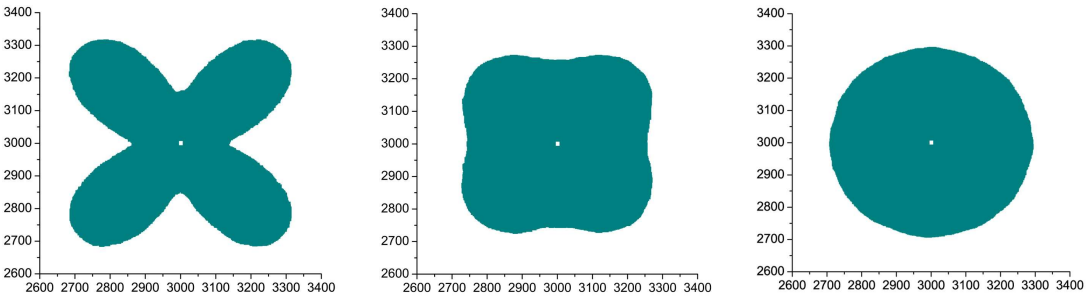

(a) $\sigma = 0.3$ and $\rho = 0.5$ (b) $\sigma = 0.5$ and $\rho = 0.5$ (c) $\sigma = 0.8$ and $\rho = 0.5$

Figure 2.5: Growth of two dimensional particles lasted for 500,000 iterations each, with different parameters of σ and $\rho = 0.5$

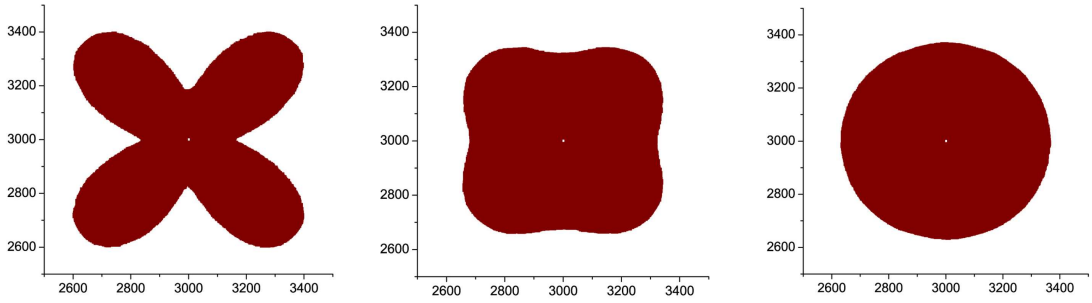

(a) $\sigma = 0.3$ and $\rho = 0.8$ (b) $\sigma = 0.5$ and $\rho = 0.8$ (c) $\sigma = 0.8$ and $\rho = 0.8$

Figure 2.6: Growth of two dimensional particles lasted for 500,000 iterations each, with different parameters of σ and $\rho = 0.8$

2.2.3 3D modeling

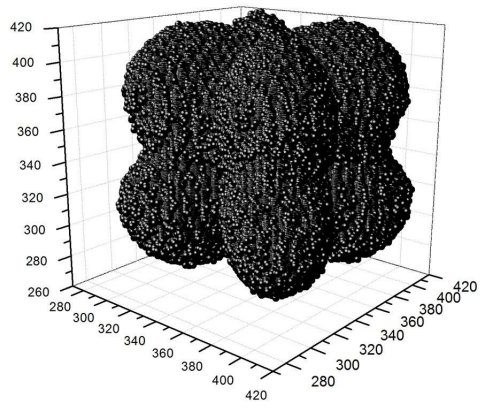

(a) $\sigma = 0.3$ and $\rho = 0.5$

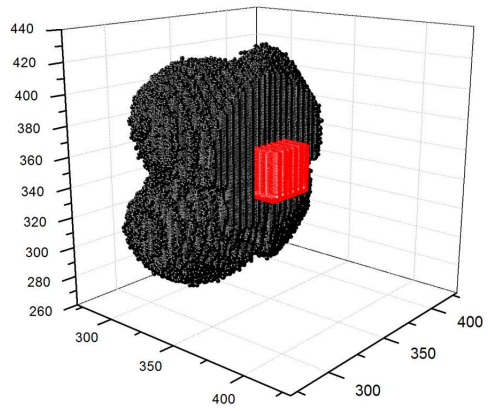

(b) $\sigma = 0.3$ and $\rho = 0.5$

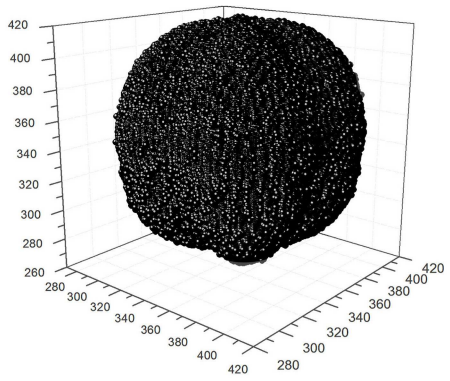

(c) $\sigma = 0.5$ and $\rho = 0.5$

Figure 2.8: Testing of various $\sigma - \rho$ combinations on three dimensional cubic particles, which lasted for 2,500,000 iterations; (a) full particle displayed and (b) its half with seed in red

The 3d simulations were similar, but due to computational resource limitations, we used a $700 \times 700 \times 700$ lattice, again with a $28 \times 28 \times 28$ cubic seed placed at the center. The total number of iterations varied between 20,000 and 40,000,000 in Figs. 2.7 and 2.8. Initial run with standard deviation of 0.3 is reflected in Fig.2.7(a).

Combinations of $\sigma = 0.2$ $\rho = 0.5$ (Fig. 2.7(b)) and $\sigma = 0.5$ $\rho = 0.5$ (Fig. 2.8(c))

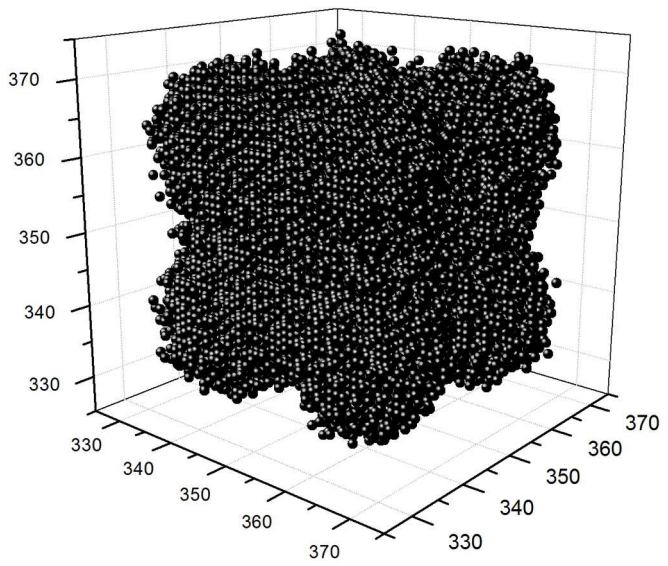

(a) $\sigma = 0.3$ and $\rho = 1$

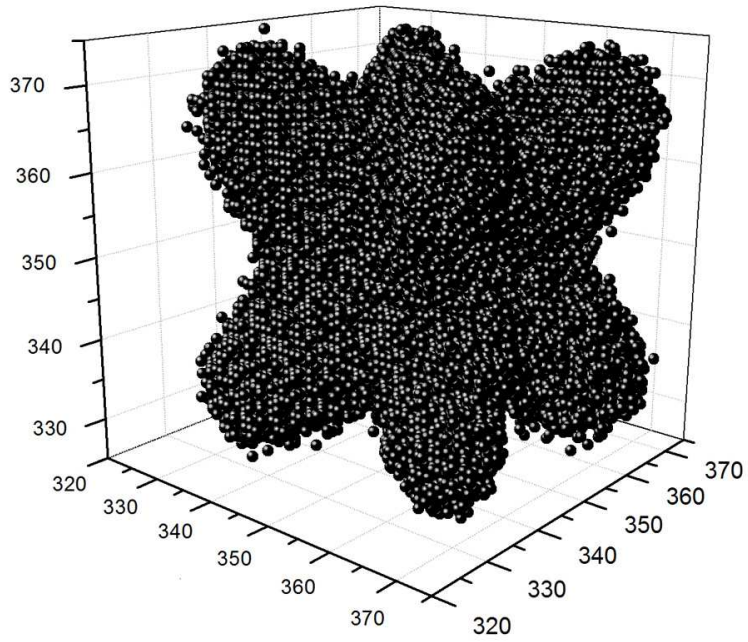

(b) $\sigma = 0.2$ and $\rho = 0.5$

Figure 2.7: Numerical simulation of three dimensional particle lasted for (a) 20,000 iterations and (b) 40,000 iterations; with different parameters of σ and ρ. The "floaters" (clearly visible in both figures) are due to the depiction of the cubic lattice points by spheres which are smaller than the lattice spacing

illustrate cluster growth with protrusions or with tendency to become spherical, depending on which process "wins". Our 3d results depicted in Figs. 2.8(a), and (b) with $\sigma = 0.3$ $\rho = 0.5$ show the same cluster grown with properly balanced dynamical processes and as a result approximately maintaining the shape "imprinted" by the original seed. Therefore, current model is much more sensitive in 3 dimensions to the selected parameters, which should be tuned very accurately.

2.2.4 Conclusion

In 2d, the core shape was maintained up to sizes approximately two orders of magnitude larger than the initial seed. In 3d, the size ratios tested were much smaller, up to $\times 4$, due to CPU time limitations. Nevertheless, the results clearly indicate that the model is much more sensitive to the choice of the values of σ and ρ in 3d than in 2d, which might imply that it could be easier to maintain regimes of well-defined particle growth on 2d substrates than in 3d solutions.

In conclusion, we comment that for general particle growth, the present simplified approach is artificial in the least, because the spatial transport is modeled by a distribution controlled by the initial seed rather than by the growing cluster shape. However, as long as the cluster shape follows the original core, we get a glimpse of a possible shape-persistence mechanism over long times and for a range of cluster sizes: the balance of monomer deposition which is sensitive to the shape features and of on-surface monomer rearrangements that favor spherical shapes.

More sophisticated modeling, likely requiring large-scale simulations, is needed to lend credence to this mechanism, which can at best be only approximate because there are other well known modes for cluster shape destabilization. More importantly, further studies are needed to understand the limits of applying such simple rate-balancing expectations and estimate the ranges of time scales and cluster sizes for

which shape persistence can be expected.

A step towards a more comprehensive treatment is reported by Gorshkov et.al. [65]. In this work authors report 3d numerical investigation on diffusive growth of fine particles with different crystal lattices (SC, BCC, FCC and HCP see Nomenclature). The key new feature of the proposed model is the focus on the growth of a single cluster, emerging as a crystalline core, without development of defects that could control large-scale growth modes. Such single, defect-free core growth was constrained by the specific dynamical rules. Obtained results offered a possible explanation of the experimentally observed shape uniformity, i.e., fixed, approximately even-sized proportions in the synthesis of uniform colloids and nanoparticles. As demonstrated it was possible to achieve several different shapes for a particle with a given crystal structure. Formation of shapes that followed the crystal symmetry and are uniform, could be a result of the nonequilibrium nature of the growth processes. The shape of a growing particle was controlled by varying the relative rates of kinetic processes, as well as by adjusting the concentration of monomers in the surrounding medium.

2.3 Experimental design statements

Recently some theoretical groups came up with significant improvements to the classical theories of aggregation, which may be calculated and compared directly with the experimental results. Thus, Privman [64] suggested and successfully evaluated diffusional nucleation of nanocrystals and their self-assembly into uniform colloids. The most essential conclusions of which are summarized in Sec. 2.1. Farjoun [87] presented a new model of homogeneous aggregation that enhances Becker-Döring and Lifshitz-Slyovoz models. The new model is valid for large and small nuclei, and, therefore, represents a complete description of the nucleation process. Barlow et. al. [88] demonstrated rules governing the average size of crystals precipitated from a supersaturated solution. The attractiveness of these studies is in the ability to substitute experimental parameters into suggested models and justify the results.

In [87] the three distinguished limits that correspond to the eras: "nucleation", "growth", and "coarsening" are resolved . Effective initial conditions for the growth era follow from matching with the tail of the nucleation era, and the tail of the growth era similarly provides initial conditions for the coarsening era.

During the nucleation era, almost all supercritical clusters are created. It lasts until the Zeldovich [89] creation rate decreases to a small fraction of its initial value. Therefore, the characteristic cluster size k and characteristic time of formation t are:

$$k = (\frac{d\eta_*^4}{\Omega\sigma^3\Lambda}e^g)^{3/5} \tag{2.19}$$

$$t = (\frac{\eta_*}{d\sigma^2})^{3/5}(\frac{e^g}{\Omega\Lambda})^{2/5} \tag{2.20}$$

here d, Ω, and Λ are constants, η_* supersaturation, σ is a surface energy constant, R integral of flux, $g = \sigma^3/2\eta_*^2$.

The growth era begins when the nucleation of additional clusters becomes negligible. The continued expansion of the existing clusters depletes the super-saturation, which in turn slows their further expansion. The "tail" of the growth era is characterized by low super-saturation, $0 < \eta \leq 1$, and a narrow, almost steady distribution of cluster sizes. Mathematically the characteristic time, t_{growth}, of the growth era is:

$$t_{growth} \sim (\frac{\eta_*}{d\sigma^2})^{3/5}(\frac{e^g}{\Omega\Lambda})^{2/5}\frac{\sigma^2}{(R\eta_*^2)^{2/3}} \tag{2.21}$$

and the characteristic cluster size is:

$$k_{growth} \sim (\frac{d\eta_*^4}{\Omega\sigma^3\Lambda}e^g)^{3/5}\frac{\sigma^3}{R\eta_*^2} \tag{2.22}$$

where the clusters all have approximately the same size, k_{growth}.

Within the growth era approximation, the cluster distribution has a definite limit as $t \to \infty$ where the super-saturation vanishes. However, an asymptotic solution predicts the emergence of a distribution of clusters where for the size of the clusters k_c, and the time of their formation, t_c are given by:

$$t_c \sim (\frac{\eta_*^4 de^g}{\sigma^3\Omega\Lambda})^{3/5}(R\eta_*^2)^{-1/3} \tag{2.23}$$

$$k_c \sim (\frac{d\eta_*^4}{\sigma^3\Omega\Lambda}e^g)^{3/5}\frac{\sigma^3}{R\eta_*^2} \tag{2.24}$$

Therefore, neighborite, galena and sellaite systems will be tested in terms of critical nuclei size and rate of growth, and compared to the suggested theories (Sec. 2.1).

Chapter 3

Experimental Techniques

3.1 Experimental tools, setups and characterization methods

As was concluded before, it is desirable to work with chemically simple systems of predictable kinetics. The candidates selected to study precipitation in aqueous solutions were neighborite ($NaMgF_3$) [66, 90], sellaite (MgF_2) [67, 90], and galena (PbS) [91]. Manipulating chemical and physical parameters, such as pH, media temperature, reactant concentrations and solubility, etc., made it possible, to some extent, to control final shapes and sizes of the precipitated particles. In Chapter 4 the initial reference experiments are described for each of the three selected systems. The effects of different parameters are tested there as well.

There are numerous techniques and methods available for fine particles and surfaces characterization. However, only the most important and appropriate of those for this particular study will be evaluated in this chapter. Due to specifics of the research topic, it was essential to utilize instruments that allowed to evaluate crystal structure, to investigate surface and internal morphologies, to obtain elemental

compositional data, and to measure the size distribution and surface charge of the investigated materials. Many of these techniques are described in the literature, nevertheless, numerous challenges related to the selected systems arose after samples preparation. Thus, the main goal of this chapter is to describe specifics of samples characterization.

3.1.1 Transmission electron microscopy

The TEM [92–94] is commonly used for studying the internal structure of samples with a thickness that transmit electrons with relatively little loss of energy. Maximum thickness depends on average atomic number of the material and should be roughly 300 nm or less at 200 keV. Transmission microscopy occupies an important niche in materials studies, particularly, being combined to scanning microscopy techniques Sec. 3.1.3. TEM provides high resolving power (down to angstroms), ability to obtain diffraction data, and the association of analytical measurements like EELS (electron energy loss spectroscopy) with surfaces. As a brief summery conventional modes of the TEM are listed below (all of them had been utilized for purposes of this research):

Bright-field (BF)(Fig. 3.1(a))

- objective aperture passes the transmitted beam;
- intermediate aperture is removed;
- picture is made of the image plane of the objective lens.

Dark-field (DF)(Fig. 3.1(b))

- same as bright-field except objective aperture passes a diffracted beam.

Diffraction contrast(Fig. 3.1(c))

- regions that diffract appear bright in the appropriate DF, dark in BF;
- regions that do not diffract appear dark in DF, bright in BF.

Selected area diffraction (SAD)(Fig. 3.1(d))

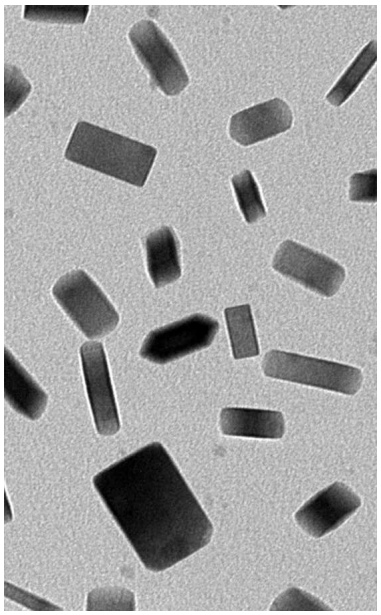

(a) Example of the bright field TEM image of PbS particles

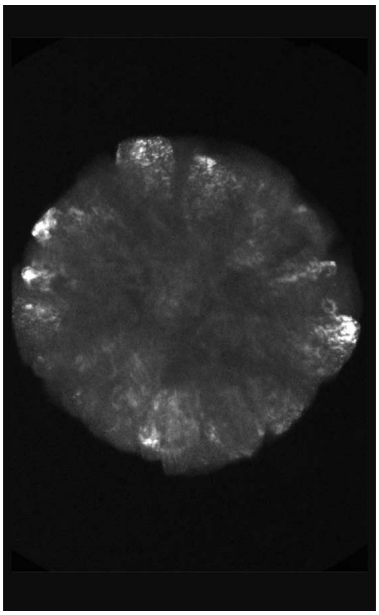

(b) Example of the dark field TEM image of MgF_2 spherical particles with distinct bright areas corresponding to individual crystallites

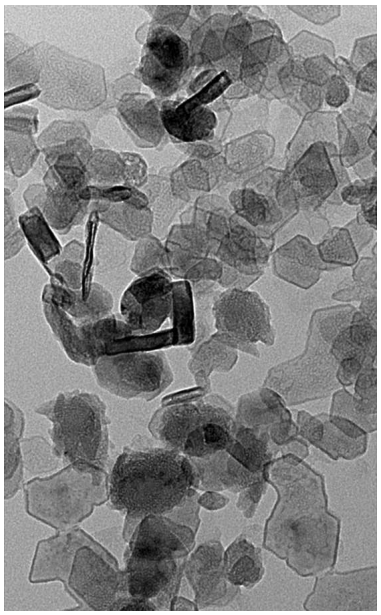

(c) Example of contrast variation of MgF_2 platelets in the bright field TEM mode

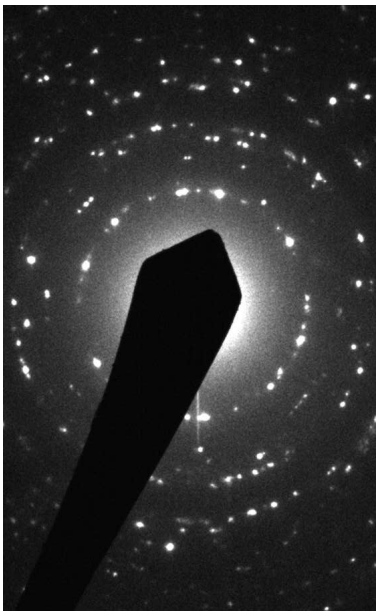

(d) Example of selected area diffraction image of MgF_2 platelets from the Fig. (c)

Figure 3.1: Typical conventional modes of TEM

- objective aperture is removed;
- intermediate aperture passes the image of a selected region;
- image is made of the back focal plane of the objective lens.

3.1.2 Selected area diffraction

The wavelength associated with a particle of mass m grams and a charge q traveling with a velocity of v m/sec, accelerated by a potential V volts is

$$\lambda = \frac{h}{\sqrt{2mqV}} \quad \mathring{A} \tag{3.1}$$

Thus the wavelength of 120 keV electrons is 0.35 Å. Electrons incident on a thin sample are diffracted though angles of the order of 10^{-2} radian; the resulting electron diffraction pattern can be observed by imaging the back focal plane of the objective lens [92, 93, 95]. Using an aperture at the level of the first image (the "selected area aperture"), diffraction data from areas down to about 300 nm can be obtained (Fig. 3.2).

Diffraction pattern of an amorphous film or polycrystalline material shows broad rings (Fig. 3.3), with maximum intensity corresponding to the most probable interatomic spacings. Crystalline materials, in contrast, show the sharp spots corresponding to Bragg diffraction by the periodic lattice (Fig. 3.2(b)). Thus, information about the degree of crystallinity, the orientation and crystal structure of individual grains, etc., can be obtained from the electron diffraction patterns. Although the dominant features of the patterns will arise from the bulk crystal, weak diffraction spots arising from surface structures can often be detected, and may be used to form dark field images of the corresponding surface detail (Fig. 3.1(b)). The most useful formula, therefore, relates interatomic spacing of a material with camera parameter and image

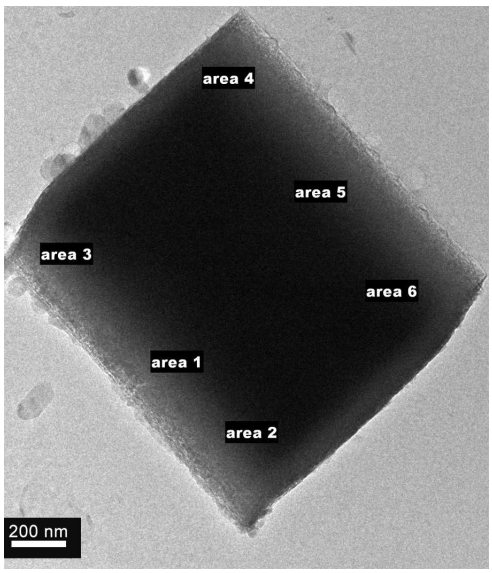

(a) Only edges of the cubic particle are translucent to TEM beam

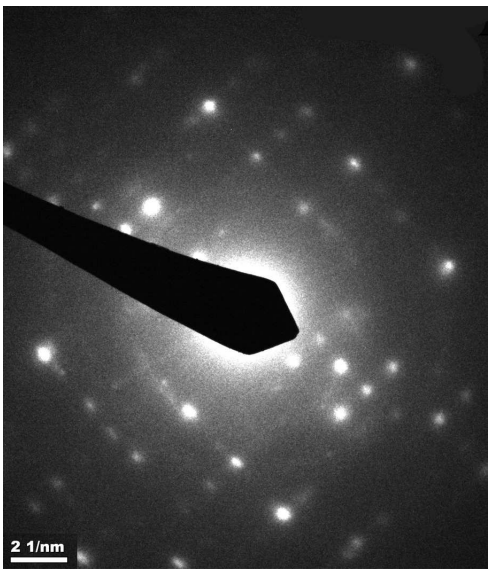

(b) Electron diffraction obtained from six areas on the left image

Figure 3.2: An example of TEM beam permeability through $NaMgF_3$ cubic particle of $\sim$1 μm

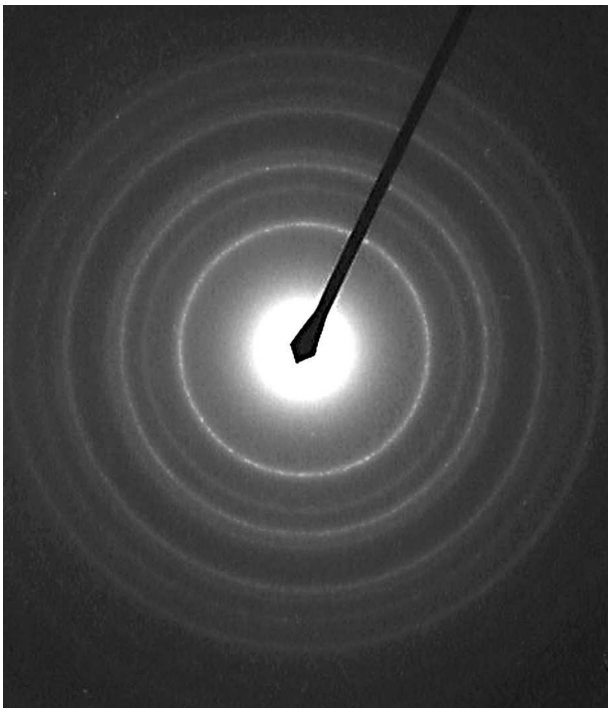

Figure 3.3: Electron diffraction of multiple $NaMgF_3$ cubic particles results in ring patterns

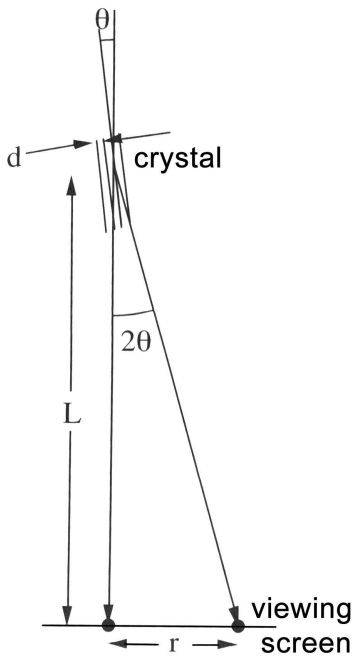

Figure 3.4: Geometry for electron diffraction and definition of camera-length, L. The electron wavelength is λ, and the camera constant of 3.2 is λL [93]

of the diffraction pattern:

$$d = \lambda \times L/r \tag{3.2}$$

here λ - wavelength of an incident electron (in the order of picometers), L - camera length (usually in the order of decimeters), and r - distance from the center of the micrograph to a diffraction spot of arc (in the order of centimeters). Geometrical meanings of the parameters may be seen in Figure 3.4.

Indexing electron diffraction patterns

While identifying electron diffractions, particular importance should be devoted to the proper indexing routine [93]. Although indexing polycrystalline micrographs may be almost trivial and predictable procedure, working on diffractograms from individual crystals from non-cubic systems, appears to be a challenging task.

Simple procedure for indexing ring patterns

(a) When identity of substance is known:

- Measure the diameters *2r* (refer to Fig. 3.4) of the rings.
- Convert these distances into interplanar d values via the camera constant.
- Compare the measured d values with standard ones for the particular substance (see Appendix D).
- Each ring can then be indexed. Confirmatory X-ray work where possible or necessary should be performed.

(b) When identity of substance is unknown:

- Measure the diameters *2r* of the rings.
- Convert these distances into interplanar d values via the camera constant.
- The arrangement of diffraction rings may indicate a certain recognizable crystal structure or type.
- Use PDF data (Appendix D) to match interplanar spacing.
- Use sample for confirmatory X-ray diffraction where possible or necessary.

Summary of simple practical procedures for indexing single-crystal patterns.

Any 2-D section of a reciprocal lattice can be defined by two vectors r_1, r_2 so one only needs to index 2 spots. All others can be deduced by vector addition.

If the crystal structure is known, the ratio procedure for indexing is:

- Choose one spot to be the origin; it does not matter which spot is chosen.
- Measure the spacings of two prominent non-collinear spots, r_1, r_2. For greater accuracy, it is advisable to measure across several spots in a line and average their spacings.
- Measure the angle ϕ between the spots.
- Prepare a table giving the ratios of the spacings of permitted diffraction planes in the known structure (refer to Table B.2).
- Take the measured ratio r_1/r_2 and locate a value close to this in the table.
- Assign the more widely-spaced plane (usually with lower indices) to the shorter r value.

- Calculate the angle between a pair of planes of the type you have indexed (refer to the Table B.2).
- If the experimental angle, ϕ, agrees with one of the possible values – accept the indexing. If not, revisit the table and select another possible pair of planes.
- Finish indexing the pattern by vector addition.

3.1.3 Scanning electron microscopy

When an electron is incident on the surface of a thick specimen, several signals can be detected [92, 96]. The primary electron results in ionization of atoms along its path in the solid, which, in turn, can result in the ejection from the surface of secondary electrons (SE) of low energy (0–20 eV) very close to the incident beam position (Fig. 3.5).

On the other hand, primary electrons can be deflected at large angles and emerge as backscattered electrons (BSE) with high energy, from a region surrounding the incident probe. Where these backscattered electrons emerge from the surface, secondary electrons are generated, so that a component of the secondary signal is proportional to the backscattered yield.

The resolution of the backscattered electron image is typically of the order of 0.1–1 μm, being determined by the volume within the sample from which comes the most of the detected BSE signal. However, in some cases it is possible to image regions showing compositional contrast at resolutions down to 2–3 nm.

When samples are loaded in the instrument, it is easy to observe a so called charging effect (Fig. 3.6). Plot 3.7 shows the ratio of SE emitted from sample to the amount of incoming electrons from the primary beam. In order to operate the SEM without charging the sample, one must operate at unity (1 electron in gets 1 electron out). If more electrons emit than come in, the sample will charge positively (area in the image will look dark). If more electrons enter than emit the sample

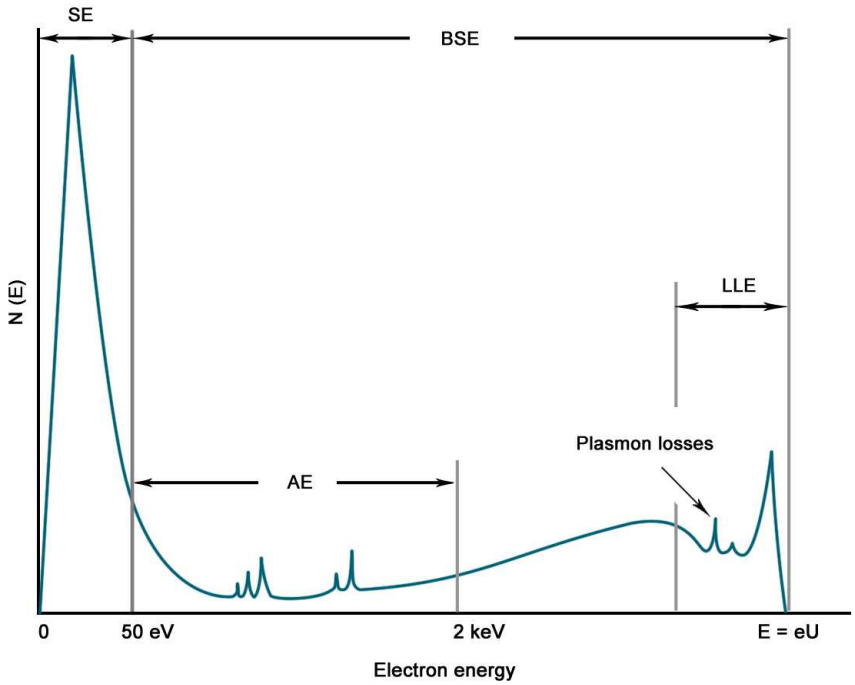

Figure 3.5: Schematic energy spectrum of emitted electrons consisting of secondary electrons (SE) with $E_{SE} \leq 50$ eV, low loss electron (LLE) with energy losses of a few hundreds of eV, backscattered electrons (BSE) with $E_{BSE} \geq 50$ eV and peaks of Auger electrons (AE) [97]

will charge negatively (areas in the image will look bright) (Fig. 3.6). Due to the effect that this will have on the electron beam, the most stable operating point is E_2 (Fig. 3.7), which is typically between 0.5 and 5 keV for most non metallic samples. It is important, however, to realize that operating SEM at low accelerating voltages requires delicate skills and very well maintained equipment. Specifics of JEOL-7400, related to the electron gun, are such that at low voltage the electron beam produces spatially metastable current flow. This current may be displaced in space under the influence of the surface charge, resulting in drifting images on the detector. In JEOL-7400 we noticed such behavior when accelerating voltage was below 0.9 keV hence, most of the current SEM observations were performed at voltages above this value.

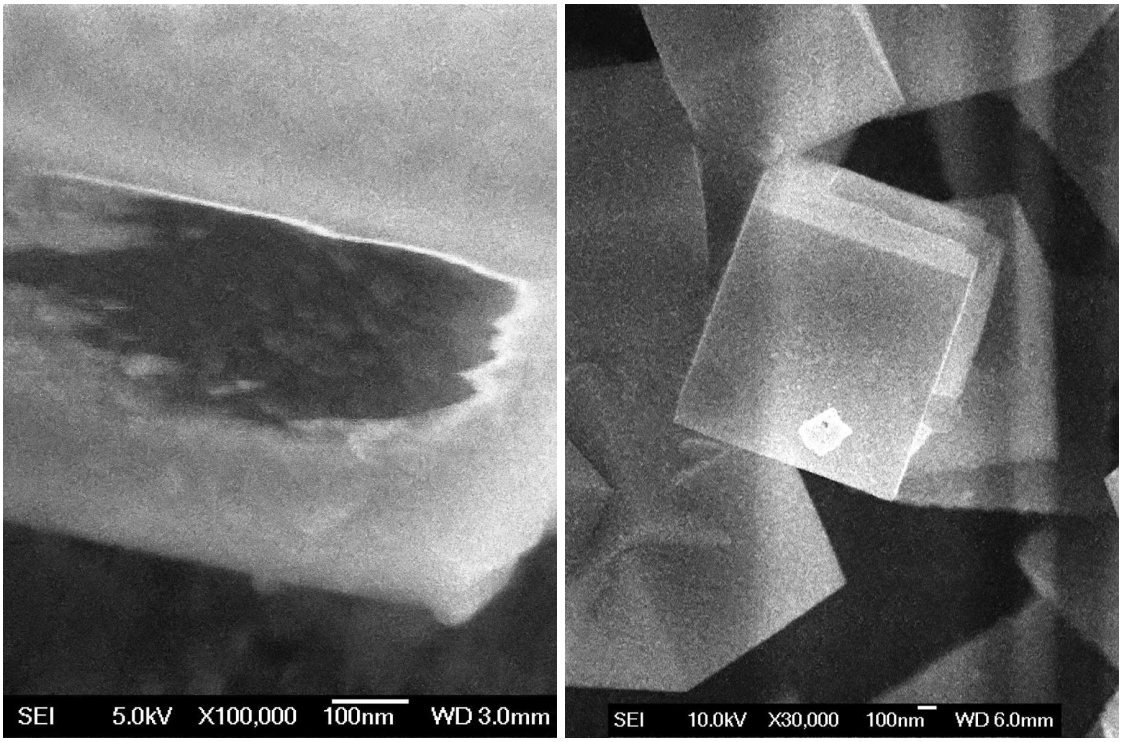

Figure 3.6: Bright and dark areas of glare formed due to uneven charging of $NaMgF_3$ particles. Usually the effect may be eliminated by proper selection of Probe current/Voltage acceleration couple

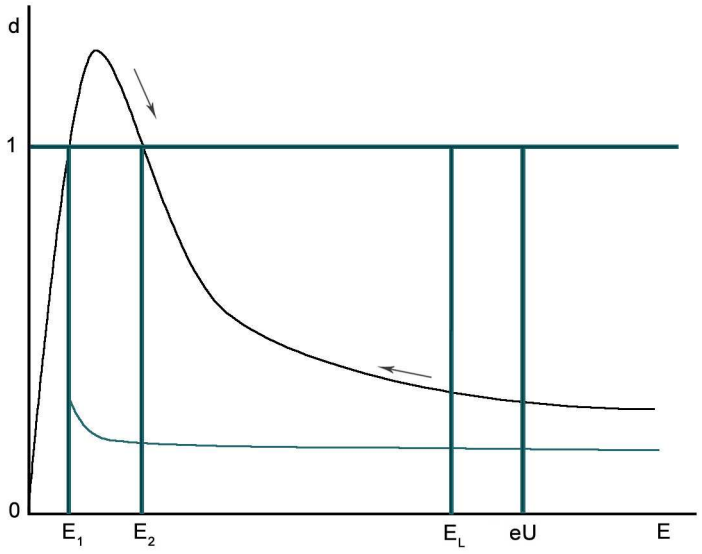

Figure 3.7: The plot of the ratio of SE emitted from sample in the amount of incoming electrons from the primary beam [97]. The electron beam, the most stable operating point is E_2, which is typically between 0.5 and 5 keV for most samples

3.1.4 Energy dispersive X-ray analysis

X-rays are generated by the incident probe within a volume similar to, but rather larger than, that for the backscattered electrons (Fig. 3.5). Peaks at energies characteristic of the elements within that volume can be identified and the concentrations of the elements can be calculated [92, 93]. Thus, the bulk composition of the sample, and of the individual grains in a polycrystalline sample may be determined for comparison with surface analytical data (Fig. 3.8).

The dimension of the interaction volume depends on the mean atomic number, the density of the material, the beam energy, and the emitted X-ray energy. Diameters range from 30 nm to several microns [96]. Thus, conventional EDX spectrometry will not reveal compositional changes due to surface segregation. It is possible, however, by analyzing a point at several different beam energies, to determine the thicknesses and compositions of layers on substrates, and hence determine the composition of those surface layers [98], although this particular method was never utilized in this study.

For our purposes EDX analysis was always employed to estimate the presence of the expected chemical elements in a sample. Depending on the signal feedback if expected elements were detected (i.e. Na. Mg, F, Pb, or S), further – more scrutinized – analyses were performed to acquire quantitative data (for example XRD, TGA, high resolution TEM, etc.)

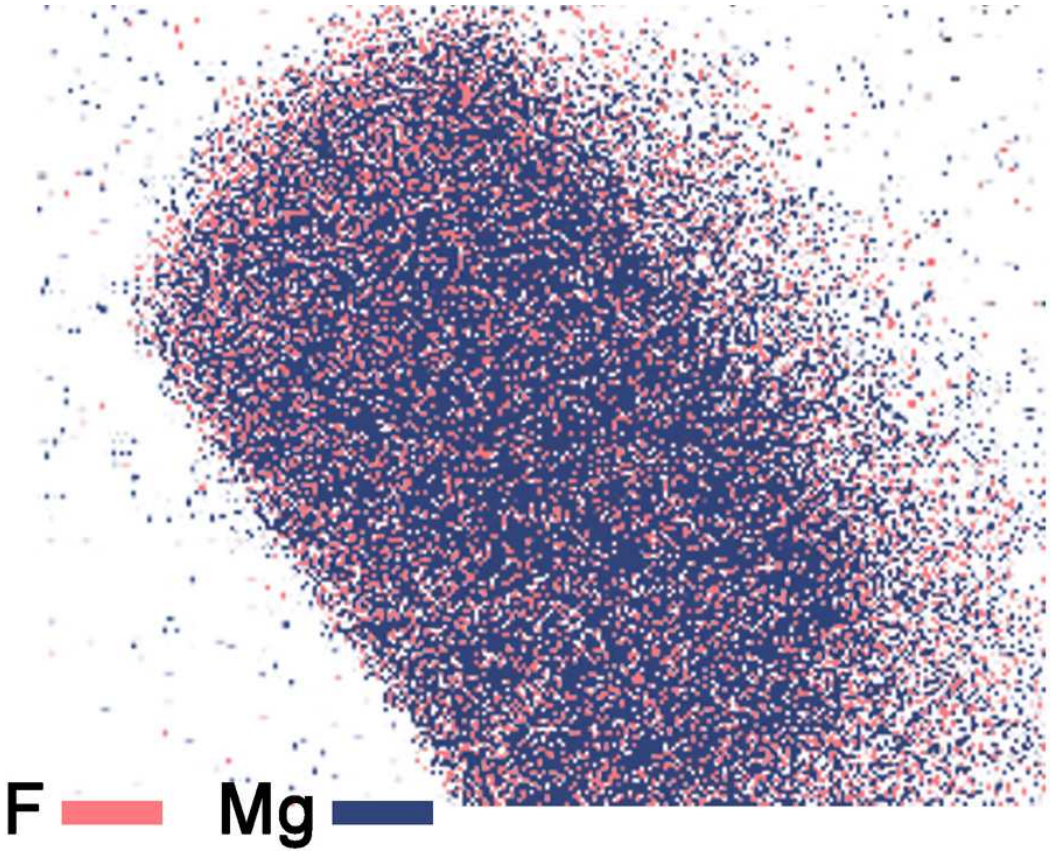

Figure 3.8: EDX element mapping of MgF_2 prismatic particle in scanning TEM mode indicates only two elements: magnesium and fluorine

3.1.5 X-Ray powder diffraction

X-Ray diffraction method is based on the utilization of high-energy electromagnetic radiation (Table B.1). This allows to conduct studies of the materials at the level of interatomic spacings, which is typically about 2Å [99].

Particularly:

- crystal structure determination;
- precise lattice parameter measurement;
- phase diagram determination;
- detection of long range ordering;
- determination of crystallite size and lattice strain;
- quantitative analysis of powder mixtures;
- identification of unknown specimen.

Understanding of Bragg's law and Miller indices are the most essential concepts used in crystal structure analysis. Thus, Bragg's law relates the wavelength λ of the incident radiation to the spacing of the atomic planes of a material:

$$\lambda = 2dsin\theta \tag{3.3}$$

Miller indices provide the way of uniquely described different crystal planes in a lattice of any plane in any crystal system, whether cubic, orthorhombic, or triclinic.

Broadening due to small crystallite size

X-ray powder diffraction method applied in this study was used mainly for the determination of crystallite size and sometimes for phase quantification. Thus, Scherrer expression [100] for broadening of X-ray diffraction peaks due only to small crystalline size (Fig. 3.9) was used:

$$D_{cryst} = \frac{k\lambda}{Lcos\theta} \qquad [rad] \tag{3.4}$$

where D is so called full width at half maximum (FWHM), λ (nm) is the wavelength of the X-rays used, θ is the Bragg angle, L (nm) is the "average" crystallite size measured in a direction perpendicular to the surface of the specimen, and k is a constant. Equation 3.4 is commonly known as the Scherrer equation and was derived based on the assumptions of Gaussian line profiles and small cubic crystals of uniform size (for which $k = 0.94$). However, this equation is now frequently used to estimate the crystallite sizes of both cubic and noncubic materials. The constant k in Eq. 3.4 has been determined to vary between 0.89 and 1.39, but is usually taken as close to unity, since the precision of crystallite size analysis by this method is, at best, about $\pm 10\%$.

Broadening due to Strain

The lattice strain in the material also causes broadening of the diffraction peaks, which can be represented by the relationship:

$$D_{strain} = \eta \times tan\theta \tag{3.5}$$

where η is the strain in the material.

Combining Eq. 3.4 and Eq. 3.5, we obtain total width of diffraction peaks:

$$D_{total} = \frac{k\lambda}{Lcos\theta} + \eta \times tan\theta \tag{3.6}$$

It is clear from Eq. 3.6 that peak broadening due to crystallite size and lattice strain increases rapidly with increasing θ, but the separation between these two is clearer at smaller angles, as shown in Fig. 3.10. Since materials may contain both small crystallite sizes and lattice strains, it is desirable to use peaks at smaller diffraction angles to separate these two effects.

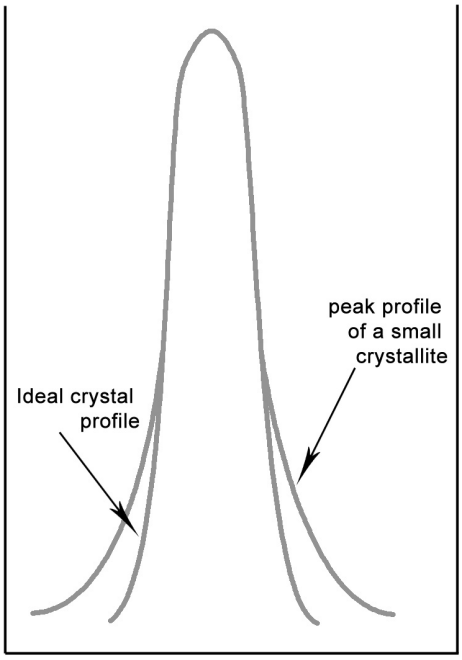

Figure 3.9: Comparison of ideal peak profile and its broadening due to small crystallite size

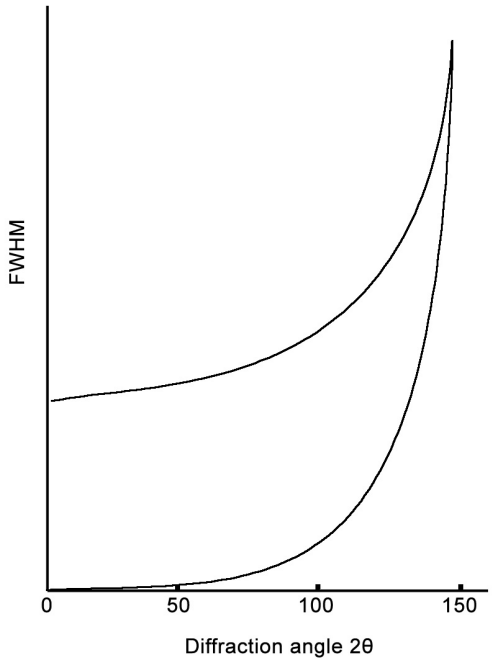

Figure 3.10: Dependence of full width at half maximum (FWHM) caused by crystallite size and lattice strain on the diffraction angle. Even though both widths increase rapidly with diffraction angle, the separation between them is large at small diffraction angles

Multiplying Eq. 3.6 by $cos\theta$ gives:

$$D_{total}\ cos\theta = \frac{k\lambda}{L} + \eta \times sin\theta \tag{3.7}$$

It is clear from this equation that function $D_{total}\ cos\theta$ against $sin\theta$ will result in a straight line with slope η, which defines the strain, and intercept $k\lambda/L$, which denotes crystallite size..

Lattice parameter measurement

Precise values of lattice parameter of materials carry essential information for accurate calculations of many physical parameters, i.e. true density values, compressibilities, solubilities, bond energies etc. Consideration of possible measurement and calculation errors, led to the development of two most common extrapolation functions:

- $f(a) = cos^2\theta$ – Bradley-Jay
- $f(a) = \frac{cos^2\theta}{sin\theta} + \frac{cos^2\theta}{\theta}$ – Nelson-Riley

where a is lattice parameter. Thus, true values of lattice parameter may be found from the intercept when plotted against extrapolation function. To utilize either of suggested functions one can make arbitrary selection. Although, Bradley-Jay function is faster to calculate and plot, Nelson-Riley relationship provides better precision in wider range of angles. In this study we used latter – more universal – extrapolation function.

3.1.6 Light scattering

Particles Size Distribution

Of the many techniques available for particle sizing, light scattering being non-destructive method offers many advantages, such as: small sample size, high speed and

short time of measurement, and versatility. The random motion of small particles in a liquid gives rise to fluctuations in the time intensity of the scattered light [101–104]. The fluctuating signal is processed by forming the autocorrelation function, C(t):

$$C(t) = Ae^{-2\Gamma t} + B \tag{3.8}$$

where A is an optical constant determined by the instrument design, B is a constant background, and Γ is related to the relaxation of the fluctuations by:

$$\Gamma = Dq^2 \tag{3.9}$$

The value of q is calculated from the scattering angle θ (commonly 90°), the wavelength of the laser light λ_0 (eg. 0.635 μm), and the index of refraction n (eg. 1.33) of the suspending liquid. The equation relating these quantities is:

$$q = \frac{2\pi n}{\lambda_0} 2sin(\theta/2) \tag{3.10}$$

Particle size is related to D [cm^2/sec] for simple common shapes like a sphere, ellipsoid, cylinder and random coil. Of these, the assumption of a sphere is the most useful in many cases:

$$D = \frac{k_B T}{3\pi\eta(t)d} \tag{3.11}$$

where k_B is Boltzmann's constant, T is the temperature in K, $\eta(t)$ is the viscosity of the liquid in which the particle is moving, and d is the particle diameter. This equation assumes that the particles are moving independently of one another.

3.1.7 Zeta potential calculation

The double layer is formed in order to neutralize the charge on the particles and, in turn, causes an electrokinetic potential between their surface and any point in the suspending liquid. This potential difference is on the order of millivolts and is referred to as the "surface potential". The magnitude of the surface potential is related to the surface charge and the thickness of the double layer.

According to electrophoresis phenomenon, a charged particle will move with a fixed velocity in the electric field. The particles mobility is related to the dielectric constant, viscosity of the suspending liquid, and on the electrical potential at the boundary between the moving particle and the liquid. This boundary is called the slip plane and is usually defined as the point where the Stern layer and the diffuse layer meet (Fig. 3.11). The Stern layer is considered to be rigidly attached to the colloid, while the diffuse layer is not. As a result, the electrical potential at this junction is related to the mobility of the particle and is called the "zeta potential" (ξ-potential) and may be expressed in different forms according to the appropriate approximation theory.

It is important to mention that in electrophoretic techniques only velocity of the colloid particles is measured, but mobility and the ξ-potential are calculated. The relationship between ξ-potential and mobility depends on the appropriate approximation model. There is no standard substance with a certified zeta potential, nor is there any known method of calculating the ξ-potential independent of a mobility measurement when using the electrokinetic technique.

There are two classic approximation models that correlate mobility μ and ξ-potential: the Smoluchowski and the Huckel models. The selection of each limit is dictated by the ka parameter (here k is the Debye length at a given concentration

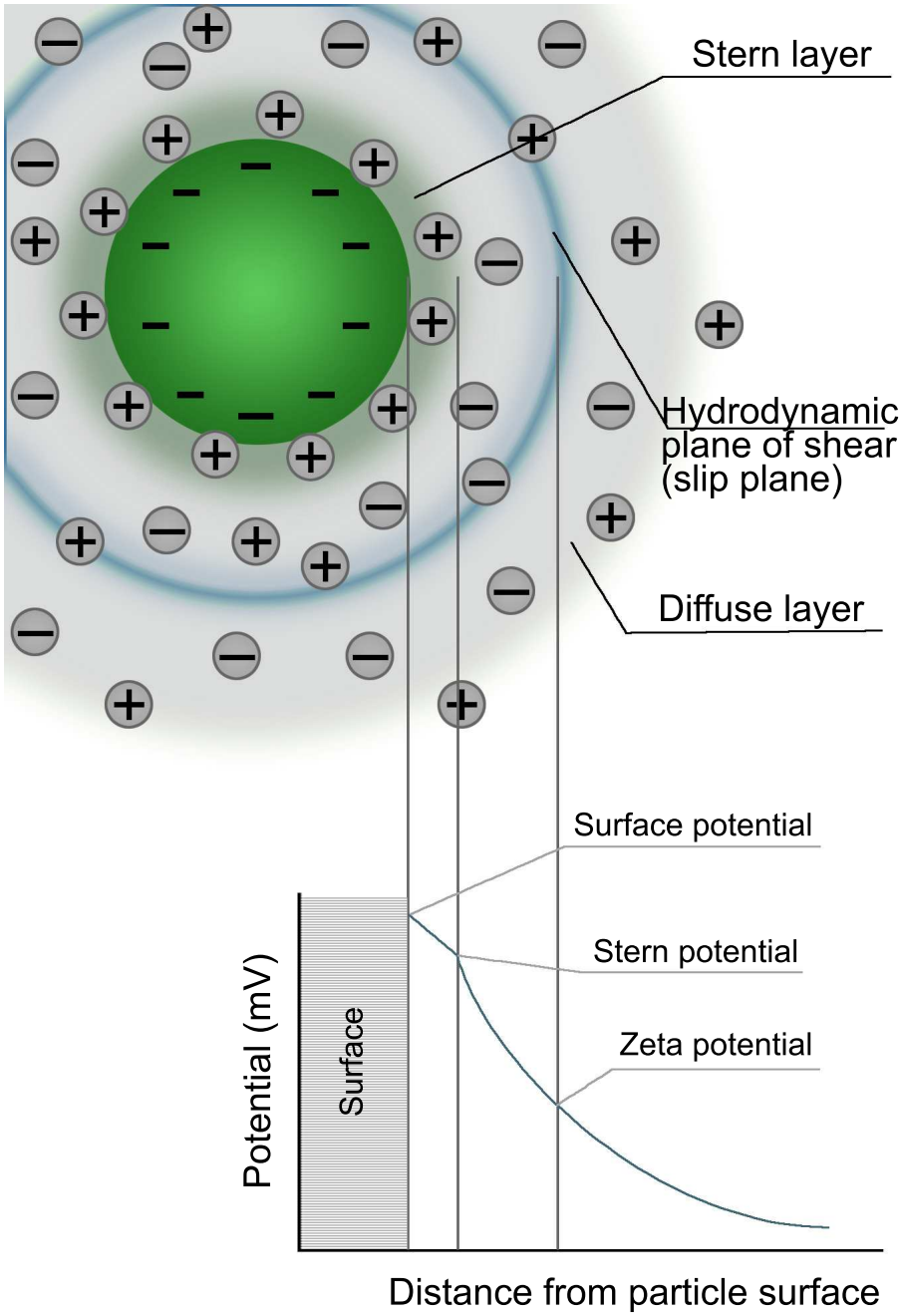

Figure 3.11: Schematic structure of the double layer of a particle

(refer to Appendix C) and a – a particle's radius). Thus, for $ka \ll 1$ Huckel approximation (3.12) should be considered, and for $ka \gg 1$ – Smoluchowski equation (3.13) should be used.

$$\mu_H = 2\epsilon\epsilon_0\xi/3\eta \quad Huckel \;\; eqaution \tag{3.12}$$

$$\mu_S = \epsilon\epsilon_0\xi/\eta \quad Smoluchowski \;\; eqaution \tag{3.13}$$

where η is the viscosity of the suspending liquid, ϵ is media dielectric constant, and ϵ_0 is permittivity of free space.

For most colloidal particles of interest, dispersed in water or highly polar liquids, it is nearly impossible to satisfy the Huckel limit; and, yet, it is not easy to completely satisfy the Smoluchowski limit either. For example, most colloids range in size from 100 nm to 1 μm; in 10^{-3} M KCl, so ka will vary between 10 and 100. Thus, in general, mobility may be related to the ξ-potential by the following equation:

$$\mu = f(\xi, ka)2\epsilon\epsilon_0\xi/3\eta \quad General \;\; form \tag{3.14}$$

where function $f(\xi, ka)$ should be constructed for the specific conditions of the measurement. For example, in the simplest – Henry-model, for 1:1 electrolytes, $f(\xi, ka) = f(ka) = 3/2 - 4.5/(ka) + 37.5/(ka)^2 - 330/(ka)^3, \quad for \;\; ka > 1$

3.1.8 Short time reaction setup

As it has been discussed earlier (Sec. 2.3), it would be essential to design experimental procedures for further utilization of data in the theoretical models. For these purposes the most useful are systems with simple chemical reaction kinetics, such as sellaite

and neighborite. It was established that particles of selected systems precipitate and grow in a very short time. To investigate their growth at early stages several methods were employed.

Freeze-and-dry

In this method an investigated dispersion rapidly freezes after specific time intervals. The shortest possible intervals achieved were 10 sec. Then frozen sample is being melted and simultaneously dried on a filter membrane. Later, resulting solids are being inspected in terms of chemical composition and crystal structure. This method was successfully applied on the neighborite system (see Sec. 4.1).

Stopped-Flow Comparatively to the freeze-and-dry method a *stopped-flow* technique provides finer time intervals. One second intervals were achieved in our studies. In this method two or more reactants were rapidly combined in a tube to initiate a fast reaction, and the resultant solution was then collected into a cell or on a membrane for further analysis. An advantage of this approach is in the possibility to vary flow rates of the reactants, their volumes, concentrations, etc., which allows for precise control of the reaction over very short times.. The principal scheme of the setup, employed in this study, is sketched in Fig. 3.12. The pumps maintained the flow of the reactants at a preset rate with reactants intensively mixed in a tube of predefined length. Resultant solution was then sprayed from the nuzzle onto a filtering membrane, which was connected to a low pressure unit (that provided "instant" drying of the resulting solids.) This method was successfully utilized on the sellaite system (see Sec. 5.2)

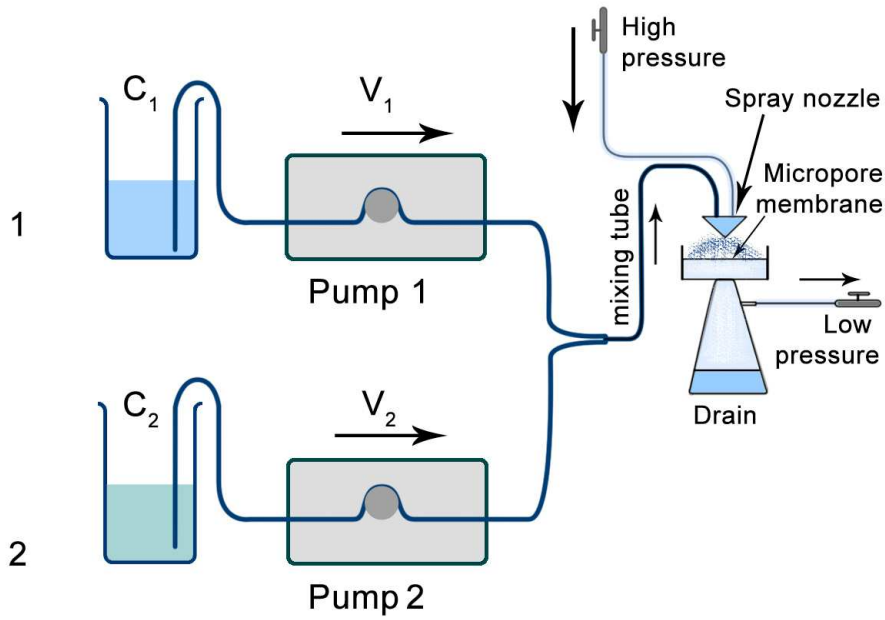

Figure 3.12: Experimental setup for early stage particle time evolution. Two stock solutions, supplied with the pumps, are combined in mixing tube. Mixed reactants are sprayed from the nuzzle onto a filtering membrane, which is connected to a low pressure unit for "instant" sample drying

3.2 Sample preparation

Below a cursory review on appropriate sample preparation for different instruments is given. Three systems – neighborite, sellaite, and galena – resulting in precipitation of the *particles only* has been studied. Therefore, most of the preparation techniques were identical for all systems.

3.2.1 X-Ray diffraction

Particles, precipitated in aqueous solutions were filtered and thoroughly washed in most cases on 0.1 μm micropore membrane. Washing is an essential stage, because it removes excess ions from the surface of the membrane, and prevents both secondary precipitation of the primary material and additional – different – chemical compounds. For example, $NaMgF_3$ cubic particles precipitate at higher concentrations of Na^+ and F^-, while MgF_2 forms film on a surface at low concentrations of those ions. Therefore, if not properly washed, after drying one may obtain both salts ($NaMgF_3$ and MgF_2) on a single substrate (Fig. 3.13), which subsequently leads to misinterpretation of X-Ray diffractograms.

After filtration, moist membrane should be placed in a desiccator for an extended period to remove all moisture from the sample. Dried particles then should be collected into a mortar, crushed into fine powder, and densely packed onto the sample holder as shown in Fig. 3.14.

In this study the resulting solids were inspected by Bruker-AXS D8 Focus under following conditions. Optimal slits for three selected materials were found to be 2, 0.6 and 1 mm, step interval—0.05° and step time—5 sec.

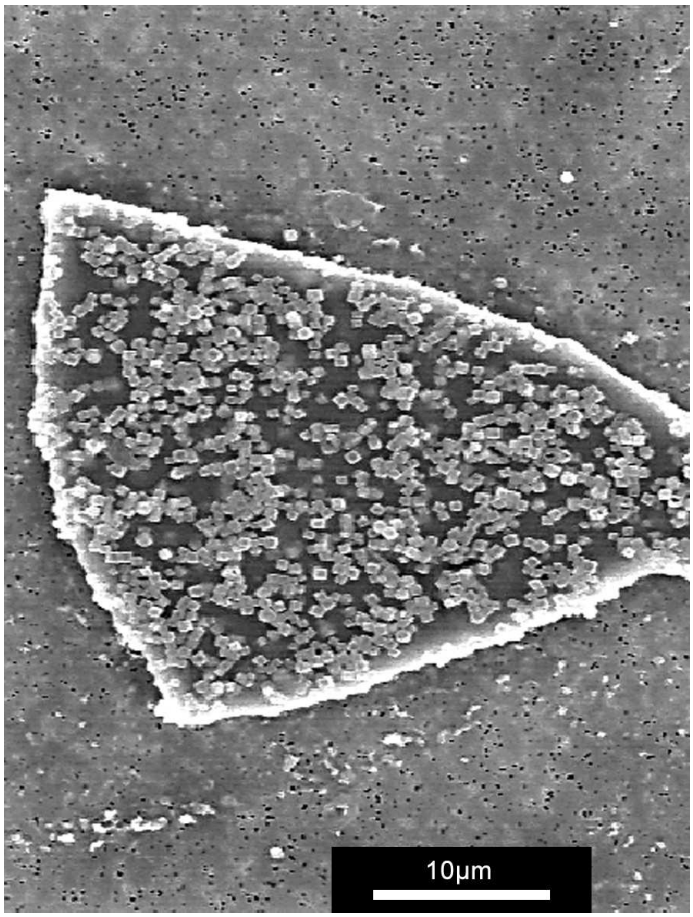

Figure 3.13: Neighborite cubic particles on top of MgF_2 film resting on 100 nm micropore filtering membrane. Sample obtained after filtration, skipping the washing procedure

3.2.2 Scanning electron microscopy and energy dispersive X-ray

Two methods were utilized to prepare SEM samples. One was performed through washing and filtration of the particles on a filtering membrane, a piece of which was then cut out and attached onto the SEM holder.

Another method was utilized by placing a droplet with precipitated particles onto the holder. Several minutes were given to allow particles to settle on the surface of the stub from the droplet. Then, the supernatant solution was removed from the

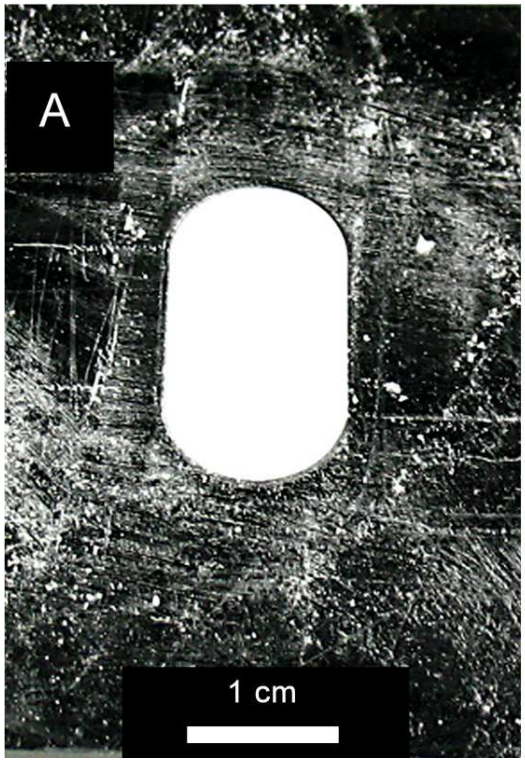

Figure 3.14: Packed sample prepared for XRD analysis

holder with the syringe and the stub was placed into the desiccator.

Materials investigated in this study were not conductive by nature. This means that a thick layer of a sample on the SEM holder results in charging effects (Sec. 3.1.3). Latter were removed either by gold sputtering (Fig. 3.15) or by accelerating voltage manipulations (Sec. 3.1.3).

All solids were inspected by FESEM JEOL-7400 in most cases between 5 and 15 keV.

3.2.3 TEM and selected area diffraction

Similarly to routines performed for SEM samples, particles may be prepared and washed for TEM. At the particle deposition stage TEM grid was placed in a tube with the dispersion of already washed particles, and was centrifuged at low RPMs

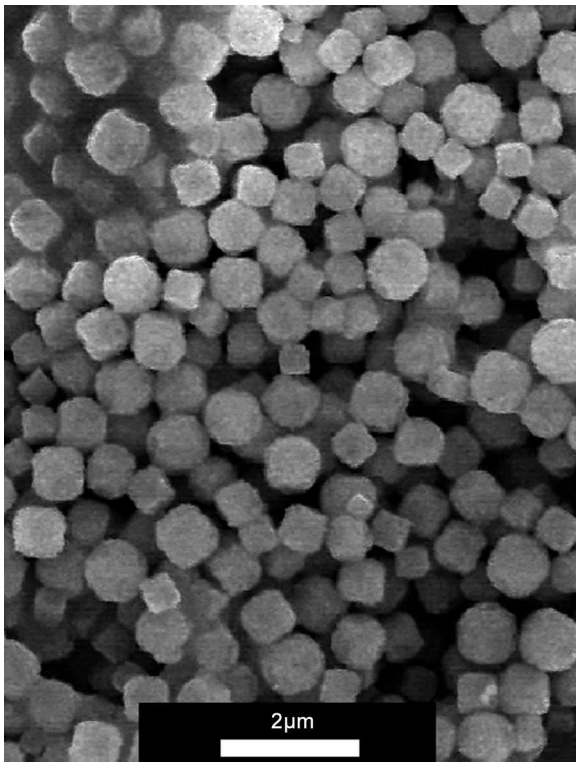

Figure 3.15: Charging effect removed by vapor deposition of nanolayer of gold on the surface of neighborite particles

(<1000) for as long as 20–30 mins. It was noticed that higher rotation rates severely damaged carbon film of the mesh. The resulting solids were inspected by TEM JEM-2010 mainly under default voltage conditions.

3.2.4 Zeta potential analyzer and particle sizing

For size distribution determination samples may be prepared in two different ways: as concentrated suspensions and dry powders, but only dispersions were analyzed in this study. For particle sizing and ξ-potential (zeta-potential) analysis, dispersions were either diluted or concentrated, if necessary, for stable data readings. To dilute dispersion a supernatant liquid was used. This prevented alternation of the chemical equilibrium between the particle surface and the solution. To concentrate a sample

the centrifugation was utilized.

Zeta potential of the dispersions was determined by Brookhaven Instruments ZetaPlus. The size distribution of the dispersions was determined by laser diffraction either Mastersizer 2000 with HYDRO 2000 accessories or Brookhaven Instruments 90Plus.

3.2.5 Freeze and dry

Several polystyrene cups with SEM holders were filled with liquid nitrogen. After chemicals had been mixed, several milliliters of the sample were rapidly deposited every ten seconds onto the freezing surface of each stub.

Each frozen droplet of the sample was then placed on individual micropore filtering membrane connected to the low pressure unit. As soon as the frozen droplet started to melt, liquid was instantly filtered, and particles, that were formed before freezing, became trapped on the membrane. When the entire sample was melted through, the membrane was washed.

Chapter 4

Materials and Particles Preparation

Materials

All systems were prepared by precipitation in homogenous solutions. The properties of precipitated products are affected in a sensitive way on the complexation of the reactants in the liquid media. The latter may be altered by the experimental parameters, including the concentration, solubility, pH, temperature, aging, all of which are also sensitive to the solvent used. In order to avoid multiple oxidation states and formation of different solute complexes, particles of simple chemical composition were selected, i.e. $NaMgF_3$, MgF_2, and PbS. The constituent ions of which do not form complexes in aqueous solutions (except at higher pH).

All reactants used for particle preparation were of the highest purity grade from Fisher.

4.1 Preparation of neighborite ($NaMgF_3$) particles

Neighborite colloidal particles were prepared by precipitation in homogenous solutions using NaF and $MgCl_2$ at concentrations given in Table 4.1. Specifically, the reactant stock solutions were preheated to 80 °C in a water bath, and rapidly mixed at different predetermined molar ratios. The mixture was then continued to age at 80 °C for three hours. During that time, samples with the dispersion were periodically removed with a pipet for characterizations in terms of their particles size, internal structure, morphology, and chemical composition (Fig. 4.1). A white precipitate appeared essentially immediately after combining the reactants, and the particles settled within ∼30 min. However, on agitation the sediment readily redispersed. In most cases resulting solids were separated by filtration, washed repeatedly with water, and dried in a vacuum.

This system was tested over a wide range of reactant concentrations [90] (Table 4.2) and showed good consistency in terms of its final particles size distribution and morphology. Additional parameters that were evaluated on $NaMgF_3$ system are listed in Tables 5.1–5.9. For example, replacing magnesium chloride with magnesium acetate (Table 5.1 B) showed that the anions played no role in the used method. Also, the effect of different cations was tested with K, Rb, and Cs salts (Table 5.1 C–E). Additional experiments were carried out to evaluate the effects of solubility (Table 5.3 F–H), viscosity (Table 5.5 K) and temperature (Table 5.7 L). The former was achieved by adding either ethanol or polyethylglycol (PEG) into the reactant solutions. In the case of viscosity effect, different amounts of pentane were used. Temperature control experiments were conducted over the range of 25–80 °C. Finally, stages of growth of investigated precipitates were evaluated on short-time and long-time scales (Table 5.8–5.9).

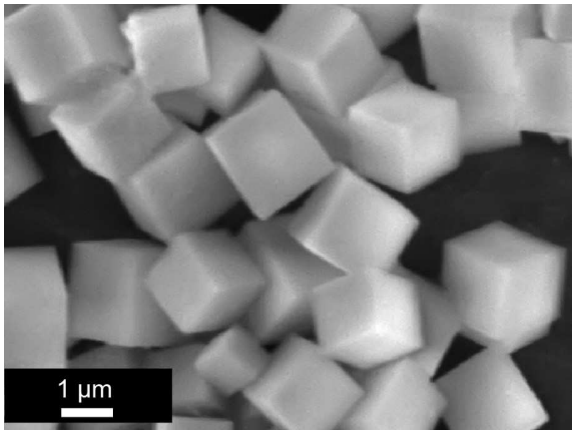

(a) Typical SEM indicates smooth surface morphology

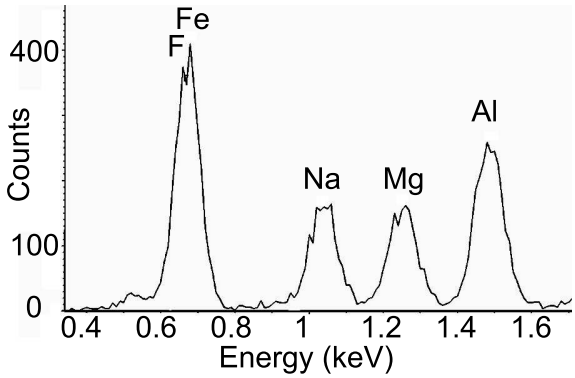

(b) Typical EDX identifies chemical composition

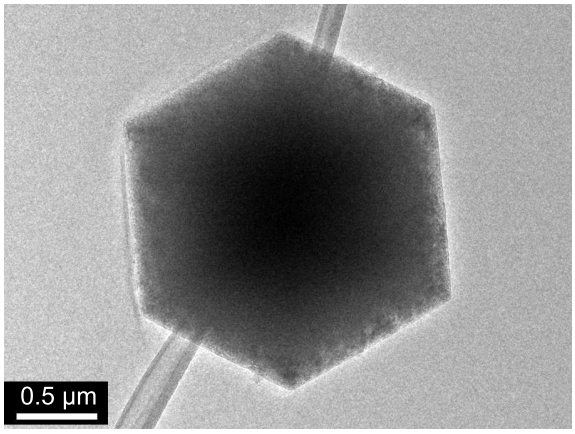

(c) Typical TEM micrograph oriented through the central diagonal of the particle

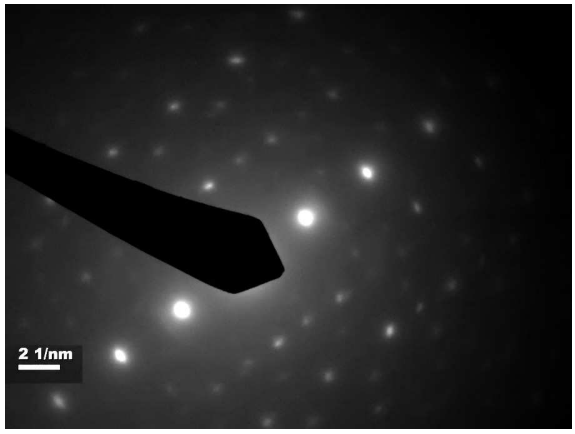

(d) Electron diffraction acquired from the particle in Fig. 4.1(e)

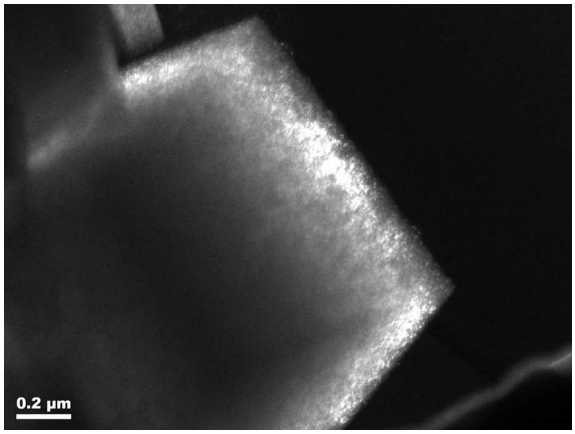

(e) Dark field TEM mode of a single particle

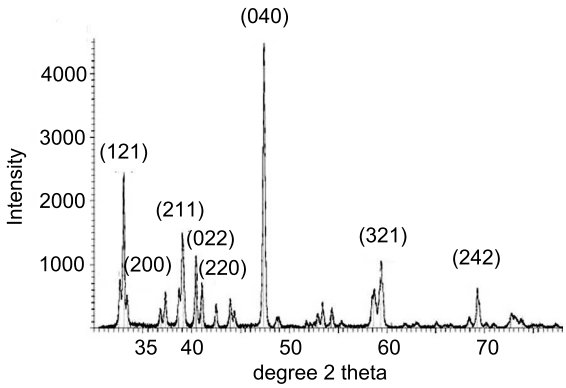

(f) Typical X-ray powder diffraction pattern

Figure 4.1: Crystalline neighborite ($NaMgF_3$) cubic particles obtained under conditions in Table 4.1

Table 4.1: Initial conditions used in the preparation of neighborite reference sample. All reactions were carried out at 80 °C

Initial conditions of stock solutions				
NaF		$MgCl_2$		Results [66]
C, mol/dm^3	V, cm^3	C, mol/dm^3	V, cm^3	
0.2	100	0.2	10	Typical well-defined neighborite cubic particles Fig.4.1

Table 4.2: Different initial conditions used in the preparation of neighborite samples. Reactants were always mixed at a 10:1 molar ratio, with NaF in excess. Although, particles were obtained over the range of the reactant concentrations, their size and morphology did not noticeably change

Initial conditions of stock solutions			
NaF		$MgCl_2$	
C, mol/dm^3	V, cm^3	C, mol/dm^3	V, cm^3
0.2—0.1	100	0.2—0.1	10

4.2 Preparation of sellaite (MgF_2) particles

Analogously to the neighborite system with some minor changes MgF_2 particles were prepared by precipitation in aqueous solutions of NaF and $MgCl_2$. Specifically, initial reactants were preheated to 80 °C, rapidly combined in equal volumes of various predetermined concentrations listed in Table 4.3, and then aged in a thermostatted water bath at the same temperature. Preliminary experiments were carried out to follow the growth of precipitated particles by removing samples over five hour period. These samples were examined by electron microscopy to track any changes in particle properties with time. It was established that the precipitates formed almost instantaneously and no changes were observed after two hours of aging. Therefore, as a rule solids generated after two hours were removed by filtration, washed on a General Electric (GE) polycarbonate membrane, and subsequently dried in a vacuum. Further evaluations showed that the methods of cooling and drying particles had no noticeable effect on their size and shape.

The following tests were carried out to establish effects of various anions and of the pH on the final precipitates. In the former case magnesium chloride was substituted by magnesium acetate, while the pH effect was tested by adding either a base (NaOH or LiOH) or an acid (HCl), while keeping all other conditions unchanged. The experimental parameters for all systems are summarized in Table 4.4.

Preparation of MgF_2 Platelets

Precipitation at pH 11 (adjusted either with NaOH or LiOH) yielded MgF_2 platelet-type particles by mixing NaF with either $MgCl_2$ or $MgAc_2$ (Table 4.4 A_1–A_4). In order to prevent precipitation of $Mg(OH)_2$, three aqueous solutions were prepared ($MgCl_2$ or $MgAc_2$, NaF, and NaOH or LiOH). The solutions of NaF and the base were

Table 4.3: Initial conditions for preparation sellaite particles with the reference sample B*. All reactions were carried out at 80 °C

Sample	Initial conditions				Results
	NaF		$MgCl_2$		
	C, mol dm^{-3}	V, cm^3	C, mol dm^{-3}	V, cm^3	
A	0.05	10	0.05	10	Fig.4.2a
B*	0.1	10	0.05	10	Fig.4.2b

Table 4.4: Initial experimental conditions (volumes, concentrations, and the pH) and resulting morphologies of MgF_2 particles. All reactions were carried out at 80 °C

#	Initial conditions of stock solutions						pH	Results
	NaF		$MgCl_2$		$MgAc_2$			
	C, mol/dm^3	V, cm^3	C, mol/dm^3	V, cm^3	C, mol/dm^3	V, cm^3		
A_1	0.02	10	0.2	10	—	—	11 (NaOH)	Platelet particles (Fig. 5.18)
A_2	0.02	10	—	—	0.2	10	11 (NaOH)	
A_3	0.02	10	0.2	10	—	—	11 (LiOH)	
A_4	0.02	10	—	—	0.2	10	11 (LiOH)	
B_1	0.02	10	0.2	10	—	—	6	Cubic particles (Fig. 5.19)
B_2	0.01	10	0.1	10	—	—	6	
C	0.02	10	0.2	10	—	—	2.7 (HCl)	Rectangular particles (Fig. 5.20)
D_1	0.2	10	0.2	10	—	—	6	Polycrystalline spherical particles [66, 90] (Fig. 5.21)
D_2	0.1	10	0.1	10	—	—	6	
E_1	0.02	10	—	—	0.2	10	6	Polycrystalline spherical particles (Fig. 5.22)
E_2	0.01	10	—	—	0.1	10	6	

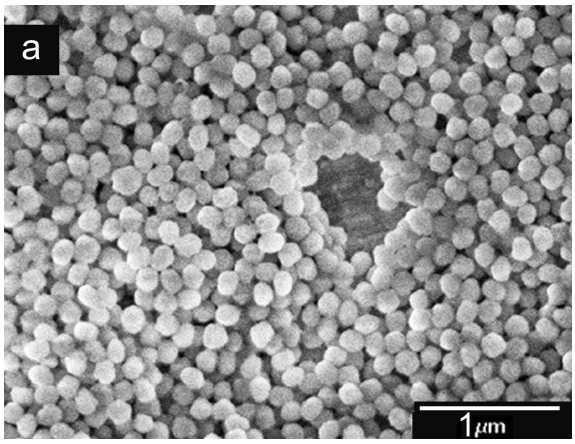

(a) MgF_2 particles of smaller diameters, sample A

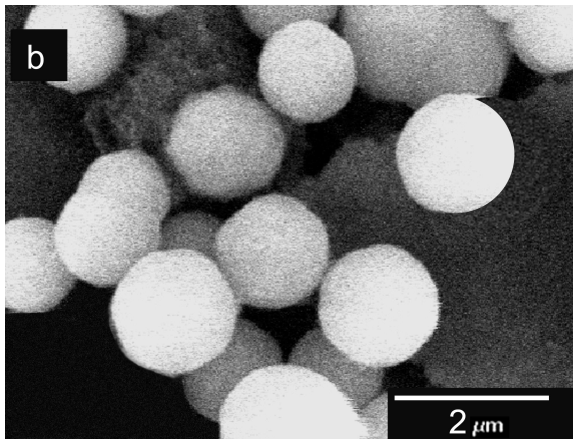

(b) MgF_2 particles of larger diameters, sample B*

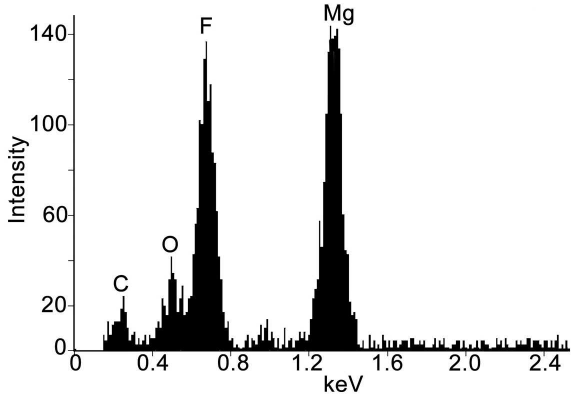

(c) EDX of the spherical particles indicates presence of both components: Mg and F

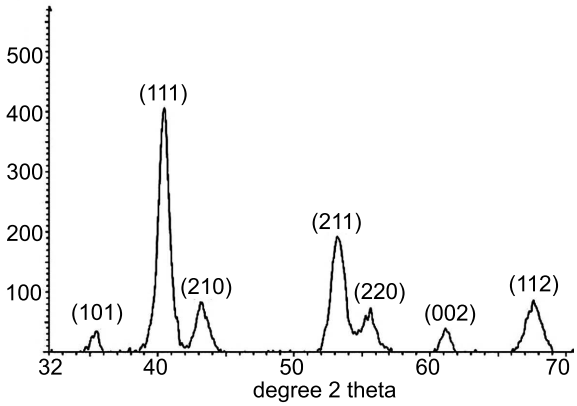

(d) Typical X-Ray powder diffraction pattern

Figure 4.2: Typical MgF_2 spherical particles of different diameters prepared under conditions given in Table 4.3

combined first, and then mixed with the magnesium salt solution. In all four cases precipitation occurred rapidly (in less than a minute), as observed by the Tyndall effect.

Preparation of MgF_2 Cubes

By mixing aqueous solutions of $MgCl_2$ and NaF at pH 6 without any additives (base or acid) under conditions in Table 4.4 B, produced single crystal cubes of MgF_2 (Fig. 5.19(a)).

Preparation of MgF_2 Prismatic Particles

Mixing NaF and $MgCl_2$ at pH 2.7 (adjusted with HCl, Table 4.4 C) yielded prismatic particles illustrated in Fig. 5.20(a). In this case it took somewhat longer time ($\sim$5 mins) for the particles to form (as indicated by the Tyndall effect) than what was observed in the cases of platelets and cubes.

Polycrystalline Spherical MgF_2 Particles

Two distinct types of spherical particles were obtained under conditions specified in Table 4.4 D and E. Earlier [66] uniform MgF_2 spherical particles made of nanosubunits were obtained under conditions in Table 4.4 D. Samples taken approximately every 10–15 minutes during a subsequent aging period of one hour showed that spheres grew slightly with time. The X-ray diffraction pattern of the solids is characteristic of MgF_2 (Fig. 5.21(b)). Furthermore, the XRD data confirmed the composite internal structure of those particles, consisting of subunits of 5–15 nm in diameter, as derived by the Scherrer method [100]. The chemical composition was corroborated by EDX analysis, which detected only Mg and F elements. In this study spherical sellaite particles were obtained, when $MgAc_2$ was used instead of $MgCl_2$ (Table 4.4 E).

4.3 Preparation of galena (PbS) particles

Original work on precipitation of lead sulfide cubic particles was performed by Wilhemly and Matijević [91]. While the cited study only describes some conditions to obtain such dispersions, the current work evaluates regimes of crystal growth under various experimental parameters.

Colloidal lead sulfide particles (Fig. 4.3) were prepared by precipitation under conditions specified in Table 4.5 A*. Sulfide ions were generated by the hydrolysis of thioacetamide in acidic media. The rate of precipitation was controlled by temperature, pH, and concentrations of TAA and of the lead ion [105]. The procedure for the formation of monodispersed colloidal metal sulfide sols involved a two-step process. First, "seeds" of the same composition were produced, which were then allowed to age either at elevated temperatures or in the presence of additional amounts of TAA. Specifically, the reactant stock solutions were rapidly mixed in predetermined volume ratios at room temperature. The mixture then continued to age for 20 hours. During entire time, the dispersion samples were periodically removed with a pipet for characterizations in terms of their particles size, internal structure, morphology, and chemical composition.

Black dispersion appeared after different times, depending on initial settings of the experiment. In most cases resulting solids were separated by filtration, washed repeatedly with water, and dried in vacuum. Various experiments were carried out to evaluate time dependent growth of PbS particles (Table 5.12), and to test the effects of temperature (Table 5.10) and the pH (Table 5.11).

Table 4.5: Initial conditions for preparation of galena particles at 20 °C

Sample	C_2H_5SN		$Pb(NO_3)_2$		HNO_3		H_2O
	C, mol dm^{-3}	V, cm^3	C, mol dm^{-3}	V, cm^3	C, mol dm^{-3}	V, cm^3	V, cm^3
A*	0.05	2	0.012	2	0.48	10	6

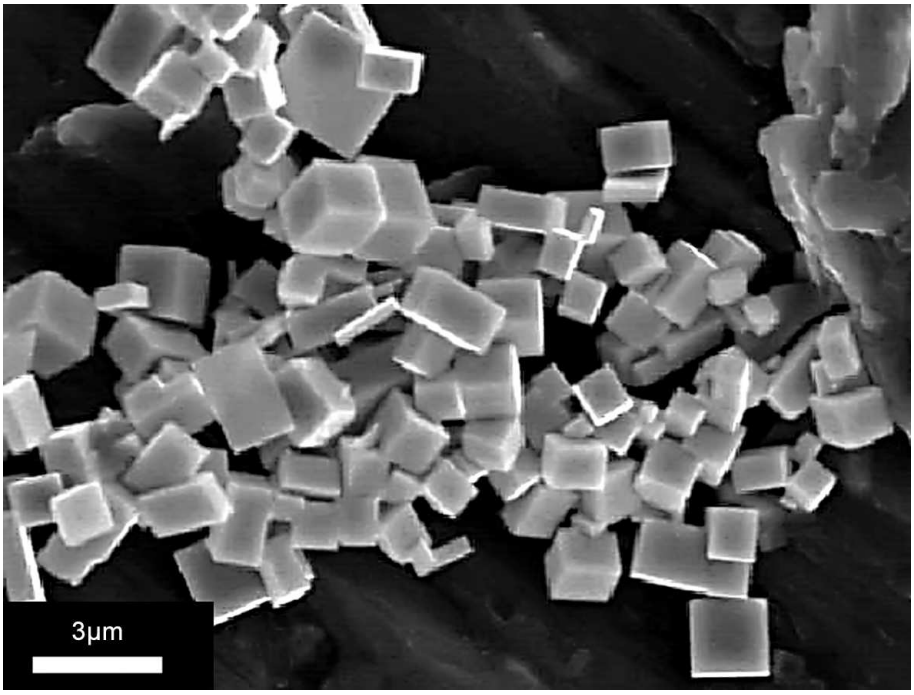

Figure 4.3: Typical PbS cubic particles prepared under conditions given in Table 4.5 A*

Chapter 5

Experimental Results and Discussions

5.1 Formation of neighborite ($NaMgF_3$) crystals

5.1.1 Effect of the anion and cation on the formation of cubic particles

Experiments carried out to test the effects of anions and cations on the morphology of neighborite particles are listed in the Tables 5.1 and 5.2.

Conditions in Table 4.1, which represent reference experiment, result in precipitation of cubic particles of 0.8–2 μm size (Fig. 4.1) as was determined with laser diffraction (Fig. 5.1). X-ray powder diffraction identified the particles as neighborite (Fig. 4.1(f)), that consist of subunits of 50–100 nm, estimated by the Scherrer method [100].

The anion effect – experiments *B* (Tables 5.1 and 5.2) – was tested on $MgAc_2$ in the same concentration range and volume ratios (10:1, with NaF in excess) as

Table 5.1: Different conditions used in the preparation of neighborite particles to test anion and cation effects

Sample	Final concentration mol dm^{-3}		H_2O cm^3	Temperature °C
	0.2	0.02		
Reference experiment				
A*	NaF	$MgCl_2$	110	80
Anion effect				
B	NaF	$MgAc_2$	110	80
Cation effect				
C	KF	$MgCl_2$	110	80
D	RbF	$MgCl_2$	110	80
E	CsF	$MgCl_2$	110	80

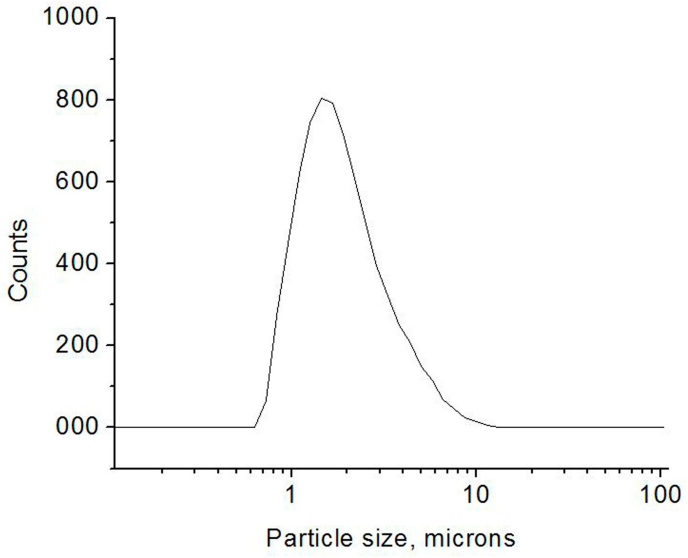

Figure 5.1: Size distribution of $NaMgF_3$ cubic particles (Table 4.1)

Table 5.2: Different conditions used in the preparation of neighborite particles to test anion and cation effects. Although, particles were obtained over the range of the reactant concentrations, their size and morphology did not noticeably change

Sample	Final concentration mol dm^{-3}		Volume ratio	H_2O cm^3	Temperature °C
	0.2–0.1	0.02–0.01			
Reference experiment					
A*	NaF	$MgCl_2$	10:1	110	80
Anion effect					
B	NaF	$MgAc_2$	10:1	110	80
Cation effect					
C_1	KF	$MgCl_2$	1:1	110	80
C_2	KF	$MgCl_2$	2:1	110	80
C_3	KF	$MgCl_2$	5:1	110	80
C_4	KF	$MgCl_2$	10:1	110	80
D_1	RbF	$MgCl_2$	1:1	110	80
D_2	RbF	$MgCl_2$	2:1	110	80
D_3	RbF	$MgCl_2$	3:1	110	80
D_4	RbF	$MgCl_2$	5:1	110	80
D_5	RbF	$MgCl_2$	7:1	110	80
E_1	CsF	$MgCl_2$	1:1	110	80
E_2	CsF	$MgCl_2$	2:1	110	80
E_3	CsF	$MgCl_2$	3:1	110	80
E_4	CsF	$MgCl_2$	5:1	110	80
E_5	CsF	$MgCl_2$	7:1	110	80

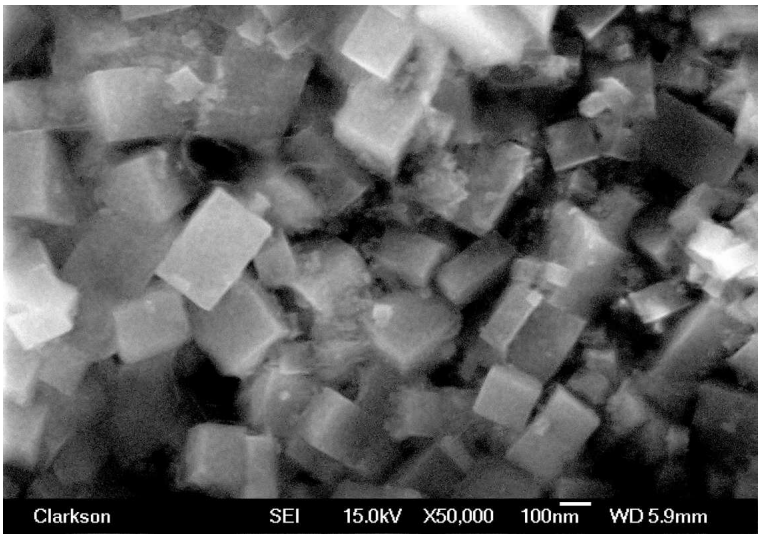

Figure 5.2: Typical SEM of $KMgF_3$ cubic particles obtained under conditions in Table 5.1 B

routine A*. Different analytical analyses performed on the precipitates demonstrated no noticeable effect on their shape, size, size distribution, crystallinity, or chemical composition. For this reason, neighborite particles prepared with either $MgCl_2$ or $MgAc_2$ were considered identical from now on.

The cation effect was tested on KF, RbF, and CsF salts (as listed in Tables 5.1, 5.2 C–E) in an attempt to produce $XMgF_3$ cubic particles (where X stands for K, Rb, or Cs). In principle, crystal structure of all $XMgF_3$ materials belongs to the tetragonal system, which means that under curtain conditions precipitation of "cubic" particles may occur. Indeed, it is demonstrated in this study that $XMgF_3$ in some instances formed cubic morphology.

Experiments C were prepared with KF instead of NaF at predetermined concentrations in accordance to Table 5.2 and mixed with $MgCl_2$ at different volume ratios (1:1, 2:1, 5:1, and 10:1, here KF was in excess). EDX and XRD analyses indicated the formation of $KMgF_3$ crystalline particles. Based on SEM images cubic morphologies of the precipitates started to be noticeable, when reactants volume ratios reached 5:1

and 10:1 (Fig. 5.2).

In the routines *D* $MgCl_2$ and RbF were mixed in the concentrations according to Table 5.2 and volume rations 1:1. 2:1, 3:1, 5:1, and 7:1 (RbF was in excess). EDX and XRD of the precipitates indicated the formation of $RbMgF_3$. Although, some experiments led to precipitation of "cubic" particles (Fig.5.3(a)), others mainly yielded dendrites on the stub surface (Fig.5.3(b)).

In the cases of CsF salt (conditions *E*) chemicals were mixed at predetermined concentrations and volume ratios similarly to RbF cases. In a number of experiments some routines resulted in the precipitation of micron size cubic particles of $CsMgF_3$ (Fig. 5.4(a)), while others produced dendritic structures upon drying on SEM stubs (Fig. 5.4(b)).

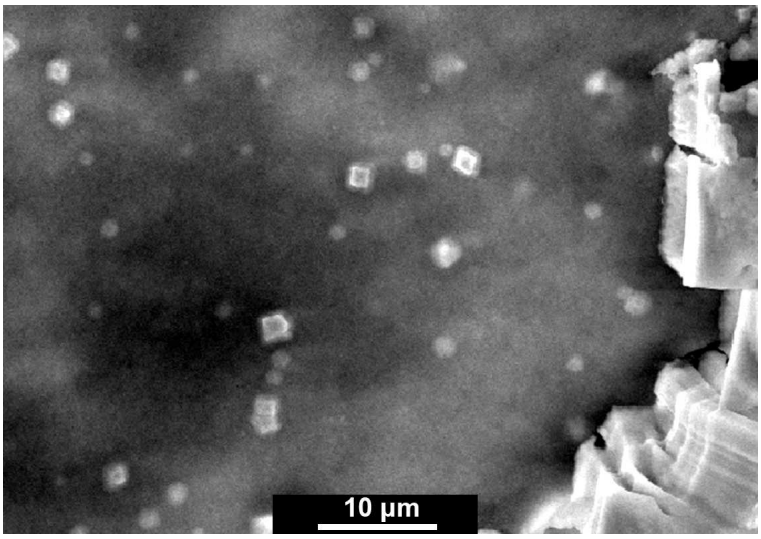

(a) Cubic particles obtained by mixing of Mg(II) and RbF at 1:3 volume ratio

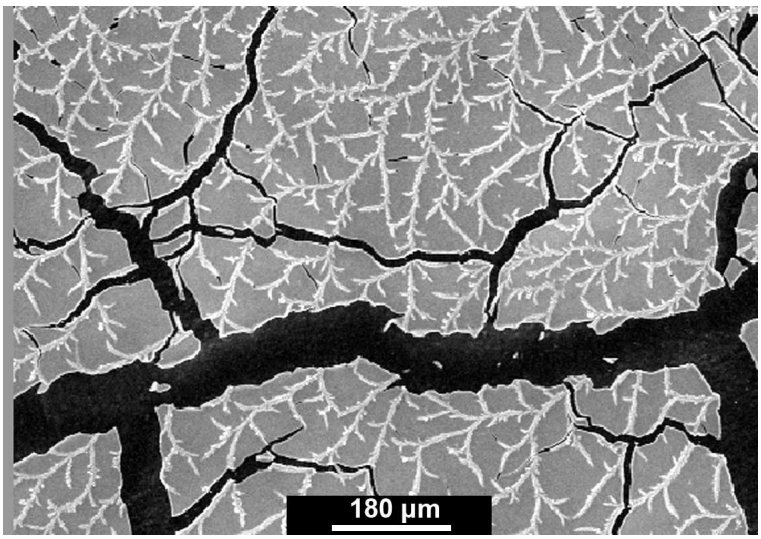

(b) Dendritic surface growth of the material observed on mixing of Mg(II) and RbF at all other volume ratios

Figure 5.3: SEM of $RbMgF_3$ cubic particles and surface dendrites

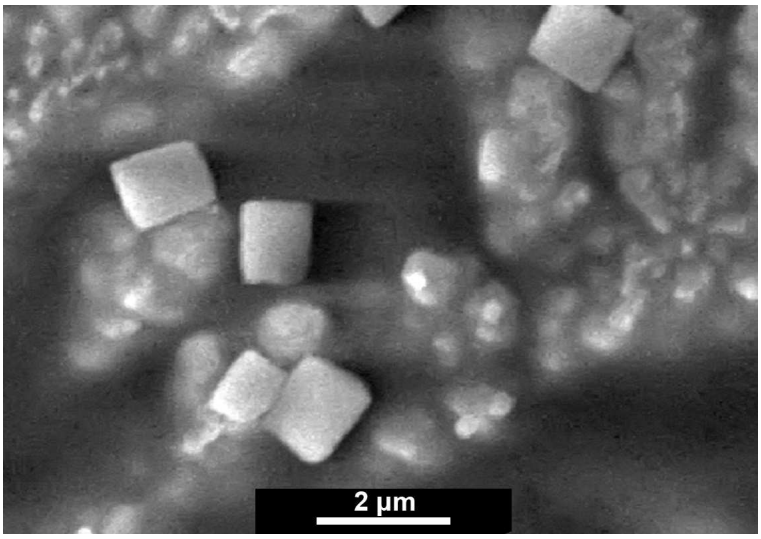

(a) Cubic particles obtained by mixing of Mg(II) and CsF at 1:5 volume ratio

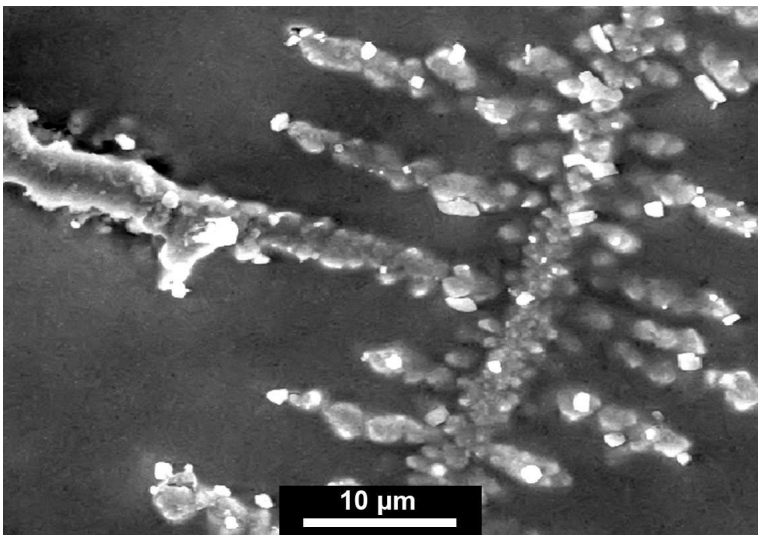

(b) Dendritic surface growth of the material observed on mixing of Mg(II) and CsF at all other volume ratios

Figure 5.4: SEM of $CsMgF_3$ cubic particles and surface dendrites

5.1.2 Effect of the reactants solubility on the formation of neighborite particles

To evaluate this effect, aqueous solutions of ethanol (Table 5.3, 5.4 F) and polyethylene glycol (PEG) (Table 5.3, 5.4 H) were used. Resulting precipitates were routinely examined for chemical composition and crystal structure by all available analytical means, which indicated the formation of crystalline $NaMgF_3$ dispersions in all following experiments.

Table 5.3: Different conditions used in the preparation of neighborite particles to test effect of the reactants solubility

Sample	Final concentration mol dm^{-3}		H_2O cm^3	Solvent cm^3	Temperature °C
	0.2	0.02			
Solubility effect					
F_1	NaF	$MgCl_2$	77	33 ethanol	80
F_2	NaF	$MgCl_2$	55	55 ethanol	80
H_1	NaF	$MgCl_2$	99	11 PEG	80
H_2	NaF	$MgCl_2$	77	33 PEG	80
H_3	NaF	$MgCl_2$	55	55 PEG	80

The solubility of $MgCl_2$ and NaF decreases by one order of magnitude in pure ethanol relatively to water [106]. Fig. 5.5 shows that the shape of prepared particles differs from cubes, when all reactant concentrations were the same as in the reference experiment (Table 4.1), except 30% or 50% (by volume) of water was substituted with ethanol (Table 5.3 F). As a matter of fact, all precipitates prepared in ethanol solution were of brick-like shape with characteristic sizes acquired from the electron micrographs $\sim 0.3 \times 0.6 \times 0.6\ \mu m$.

Table 5.4: Different conditions used in the preparation of neighborite particles to test effect of the reactants solubility. Although, particles were obtained over the range of the reactant concentrations, their size and morphology did not noticeably change

Sample	Final concentration mol dm^{-3}		Volume ratio	H_2O cm^3	Solvent cm^3	Temperature °C
	0.2–0.1	0.02–0.01				
Solubility effect						
F_1	NaF	$MgCl_2$	10:1	77	33 ethanol	80
F_2	NaF	$MgCl_2$	10:1	55	55 ethanol	80
H_1	NaF	$MgCl_2$	10:1	99	11 PEG	80
H_2	NaF	$MgCl_2$	10:1	77	33 PEG	80
H_3	NaF	$MgCl_2$	10:1	55	55 PEG	80

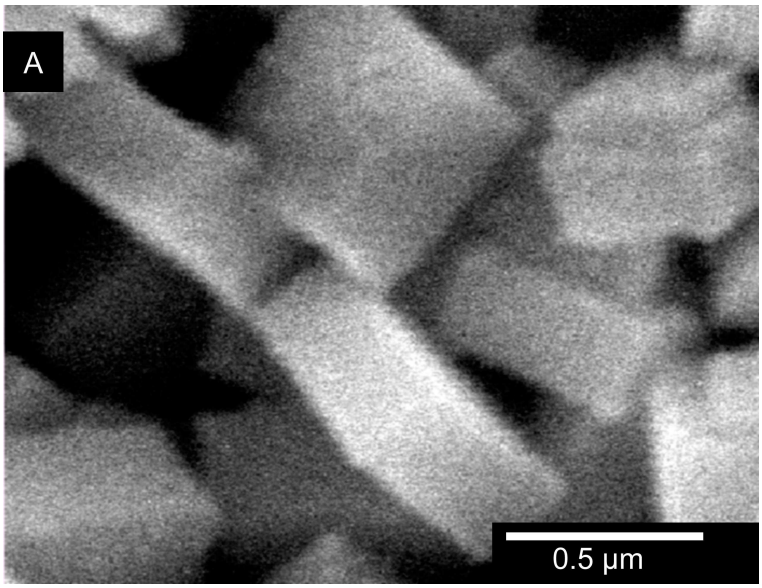

Figure 5.5: $NaMgF_3$ prepared in ethanol accordingly to Table 5.3 F_1

Neighborite particles prepared by precipitation from PEG (Table 5.3 H) as a rule were smaller in size. While concentrations and volume ratios of NaF and $MgCl_2$ were predetermined accordingly to the reference procedure (Table 4.1), aqueous solutions of PEG were prepared in several different concentrations –10, 30, and 50% (by volume). Similarly to the case with ethanol, resulting precipitates have brick-like shape with fairly smooth surfaces. For instance, at 50% of PEG precipitates have $\sim 200 \times 500 \times 500$ nm characteristic sizes (Fig. 5.6) and made of ∼65 nm crystallites in accordance to the Scherrer method.

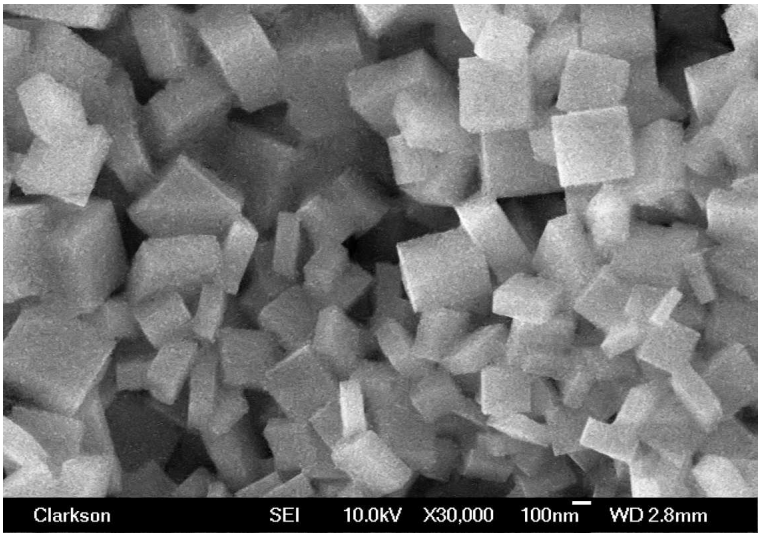

Figure 5.6: SEM of platelet particles prepared in 50% aqueous solution of PEG (Table 5.3 H_3)

5.1.3 Effect of the viscosity on the formation of neighborite particles

As was previously noted, cubic particles of neighborite were formed with characteristic sizes of ∼0.5 μm in ethanol (which viscosity is 122 g/(cm sec) [106]). A set of experiments was designed to test correlation between neighborite particles size, their surface morphology, and the viscosity of media (Table 5.5, 5.6 K).

Table 5.5: Experimental conditions used in the preparation of neighborite particles to test solution viscosity

Sample	Final concentration mol dm^{-3}		H_2O cm^3	Solvent cm^3	Temperature °C
	0.2	0.02			
Viscosity effect					
K_1	NaF	$MgCl_2$	99	11 pentane	80
K_2	NaF	$MgCl_2$	88	22 pentane	80
K_3	NaF	$MgCl_2$	77	33 pentane	80
K_4	NaF	$MgCl_2$	55	55 pentane	80
K_5	NaF	$MgCl_2$	22	88 pentane	80

While concentrations and volume ratios of NaF and $MgCl_2$ were predetermined according to the reference procedure (Table 4.1), aqueous solutions of pentane were prepared in several different concentrations –10, 20, 30, 50, and 80% (by volume). Viscosity of pentane is 24 g/(cm sec), and the solubility of NaF and $MgCl_2$ in it is close to the solubility in ethanol. Experiments with pentane were conducted in sealed glassware at 60 °C due to its lower boiling point. Results from SEM images (Fig.5.7(a)) and particle sizer (Fig. 5.7(b)) showed that size distribution of neighborite crystals was close to the sizes of the precipitants obtained in ethanol. which

Table 5.6: Experimental conditions used in the preparation of neighborite particles to test solution viscosity. Although, particles were obtained over the range of the reactant concentrations, their size and morphology did not noticeably change

Sample	Final concentration mol dm^{-3}		Volume ratio	H_2O cm^3	Solvent cm^3	Temperature °C
	0.2–0.1	0.02–0.01				
Viscosity effect						
K_1	NaF	$MgCl_2$	10:1	99	11 pentane	80
K_2	NaF	$MgCl_2$	10:1	88	22 pentane	80
K_3	NaF	$MgCl_2$	10:1	77	33 pentane	80
K_4	NaF	$MgCl_2$	10:1	55	55 pentane	80
K_5	NaF	$MgCl_2$	10:1	22	88 pentane	80

indicates no influence of viscosity on final size of $NaMgF_3$ particles.

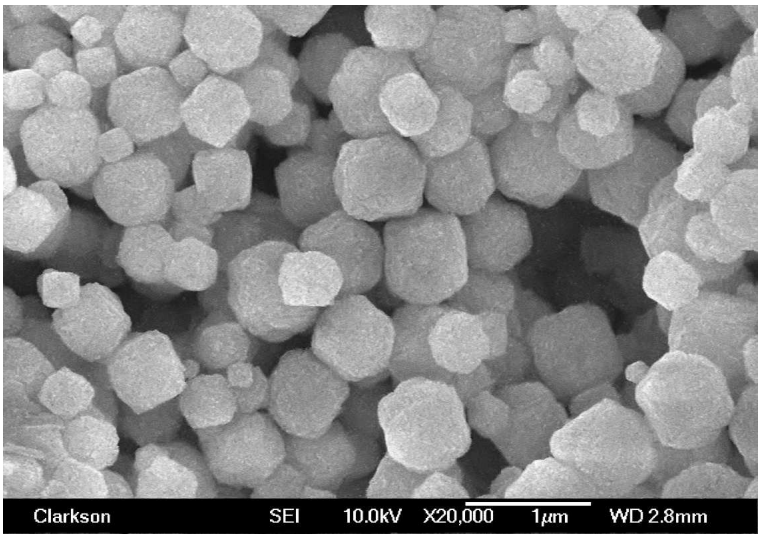

(a) SEM of neighborite particles prepared in 50% aqueous solution of pentane

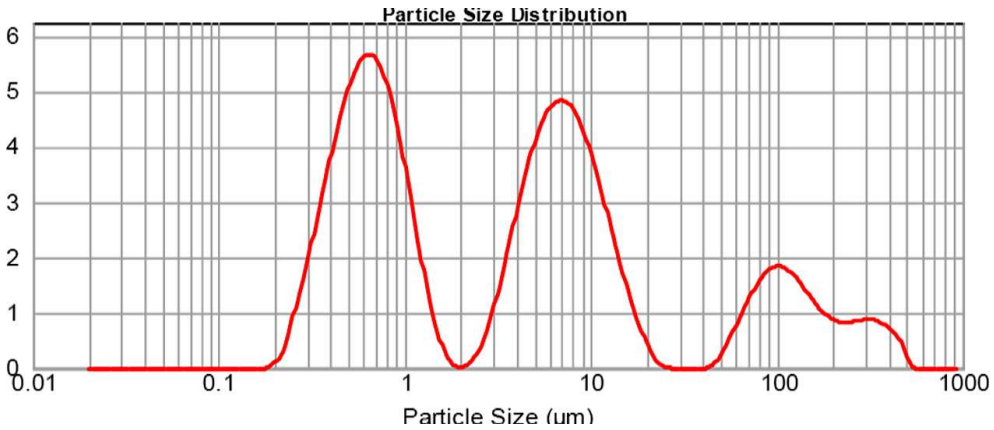

(b) Size distribution of neighborite particles precipitated in pentane

Figure 5.7: Viscosity effect tested on neighborite particles prepared in pentane (Table 5.5 K)

5.1.4 Temperature effect on the formation of neighborite particles

To test the effects of temperature, experiments were conducted under identical chemical conditions at 25, 40, and 80 °C (Table 5.7 L).

Table 5.7: Experimental conditions used in the preparation of neighborite particles to test temperature effect

Sample	Final concentration		H_2O	Temperature
	mol dm^{-3}		cm^3	°C
	0.2	0.02		
Temperature effect				
L_1	NaF	$MgCl_2$	110	25
L_2	NaF	$MgCl_2$	110	40
L_3	NaF	$MgCl_2$	110	80

Initially particles were prepared under conditions (Table 5.7 L_3) at 80 °C. During the early stages of the reaction the solids already indicate cubic habit, although their surface appears rough without well defined edges (Fig 5.8 (e)). After 15 minutes of aging most of the dispersed solids formed as well-defined smooth cubes with sharp edges (Fig. 5.8 (f)). After three hours all particles had cubic shape.

Other experiments were carried out at lower temperatures, i.e. at 25 °C and 40 °C (Table 5.7 L_1), L_2, respectively). The representative FESEM micrographs are given in Fig. 5.8. While the precipitation proceeded as fast as at 80 °C the morphology of the particles was affected by temperature. At 40 °C the cubic shape was less pronounced with rounded corners, and nearly spherical at 25 °C. The X-ray patterns of all those samples had the same characteristics that shown in Fig. 4.1(f). In fact, even calculated

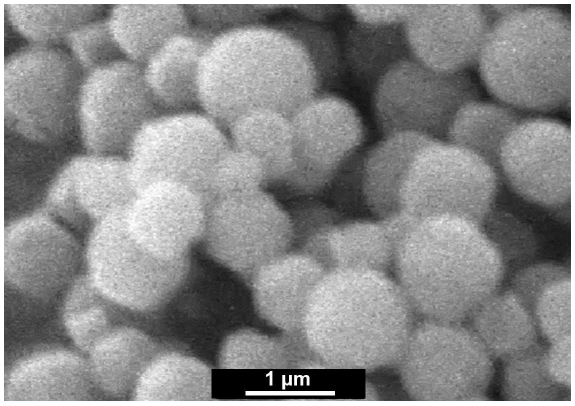

(a) Particles obtained at 25 °C essentially immediately after mixing

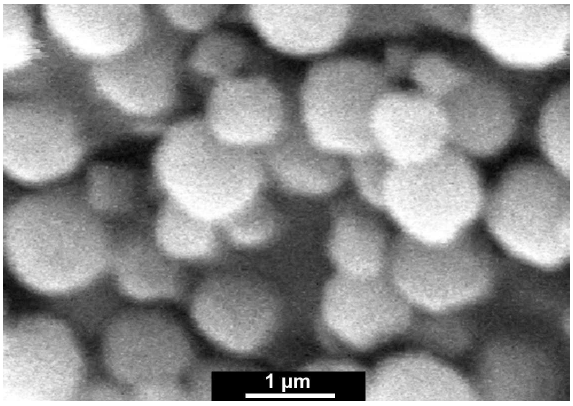

(b) Particles formed during 15 minutes of aging at 25 °C

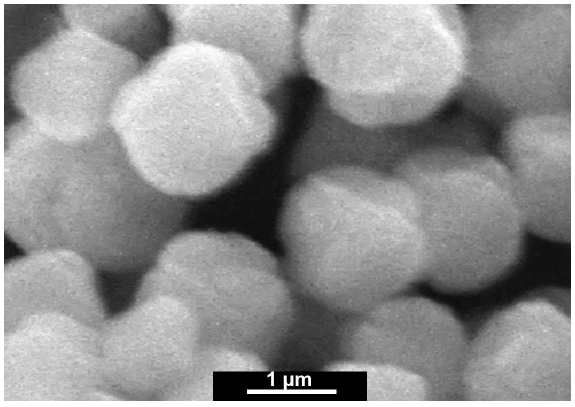

(c) Particles obtained at 40 °C essentially immediately after mixing

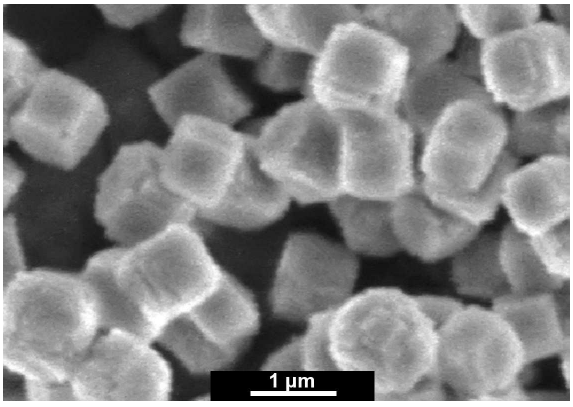

(d) Particles formed during 15 minutes of aging at 40 °C

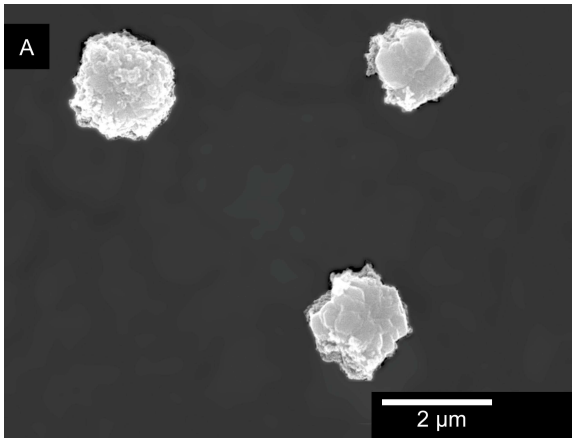

(e) Particles obtained at 80 °C essentially immediately after mixing

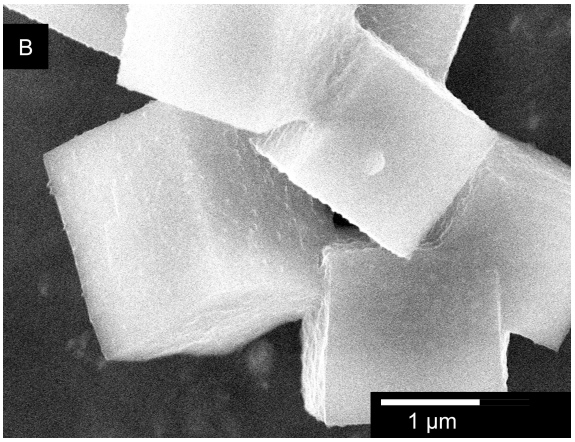

(f) Particles formed during 15 minutes of aging at 80 °C

Figure 5.8: Temperature effect on the formation of $NaMgF_3$ particles (Table 5.7)

average crystallite sizes for samples A, L_1–L_2 resulted in nearly identical values (50–58 nm), which indicates that there is no correlation between particles morphology and their crystallite sizes.

These findings indicate that the environmental temperature has a strong effect on the formation of neighborite particles. At room temperature it was not possible to obtain cubic particles even after two months (see next section). However at 40 °C, cubes started to form after some reasonable time (∼15–20 minutes). Also the higher was the temperature the more prominent was the cubic shape of the solids (with smoother surfaces and sharper edges).

5.1.5 Formation of neighborite particles on extended time scales

Shape track on a month scale

As was summarized above – temperature of the media plays a significant role on the final shape of neighborite particles. At higher temperatures cubic particles are formed, while at lower – only spherical solids were observed. Therefore, it is natural to inquire whether the particles that were formed at lower temperatures are given enough time to reach their equilibrium shape. To answer this question the precipitates were prepared at room temperature under conditions specified in Table 5.8. After the first day of aging the sample was split into two beakers. One was instantly heated and kept for 5 hours at 80 °C, where the other continued to age at room temperature for two more months and only then it was heated to 80 °C for 5 additional hours.

Table 5.8: Experimental conditions used to test precipitation of neighborite particles over extended period

Sample	Final concentration		H_2O	Temperature
	mol dm^{-3}		cm^3	°C
	0.2	0.02		
Time scale (over two months)				
M	NaF	$MgCl_2$	110	25

Almost every other day a drop of the sample was taken for SEM and EDX observations. Two samples were prepared for XRD to evaluate their crystallite structure: on the first day of the experiment, and after two months. It was confirmed that only neighborite crystals were formed, which crystallinity did not noticeably change with time (crystallites size remained near 45±10 nm.)

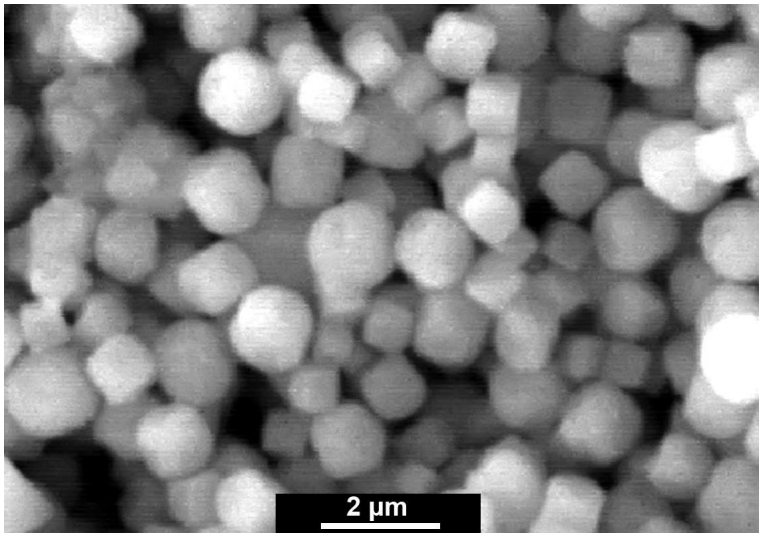

(a) Particles aged for three hours at room temperature

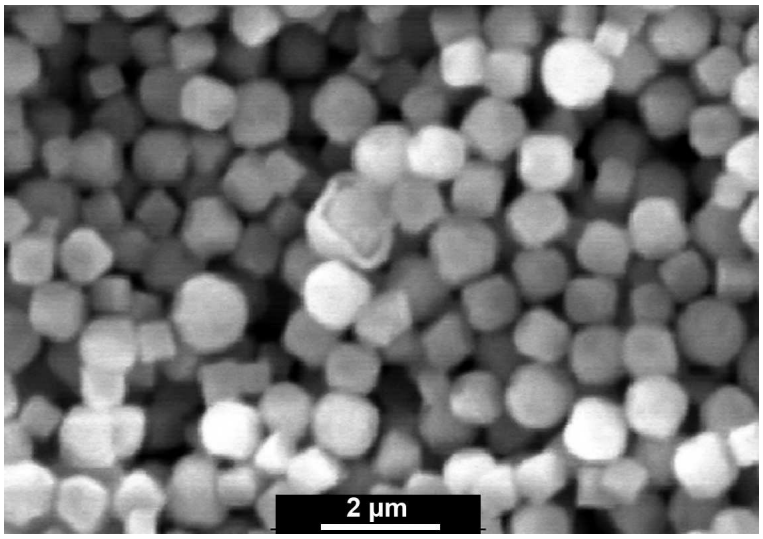

(b) Particles aged at room temperature for 2 months

Figure 5.9: Shape evolution of $NaMgF_3$ particles at room temperature on the two months period

Based on this study, we believe that the final shape of neighborite particles establishes during first several hours of aging (Fig. 5.9). This shape is dependent on media temperature during particles formation and some additional aging period thereafter. In other words, the shape of the particles does not noticeably change on a long time scale. Also, from the experiments follow that there is a period of several days (at 25 °C), during which spherical $NaMgF_3$ still may be recrystallized into cubic if temperature increases to 80 °C. When neighborite spherical precipitates were formed at room temperature and aged for 24 h, increasing the temperature to 80 °C for 5 extra hours resulted in the transformation of most of the solids into cubes. In contrast – increasing the temperature after one month of aging did not have a noticeable effect on the final morphology of the particles.

Shape evolution on a minute scale

While no shape evolution was detected at a long run, it is natural to inspect growth of the particles at shorter time scales. Numerous experiments conducted at 80 °C indicated that after 5 minutes of aging neighborite cubic particles were essentially formed. In those routines 5 minutes was a minimal time interval necessary to prepare a SEM/TEM sample.

Table 5.9: Experimental conditions used to test precipitation of neighborite particles over short period

Sample	Final concentration		H_2O	Temperature
	mol dm^{-3}		cm^3	°C
	0.2	0.02		
Time scale (over one minute)				
N	NaF	$MgCl_2$	110	80

To shorten this time limit a "*freeze-dry*" technique (see Sec. 3.1.8) was successfully

utilized. Major reactants were prepared in a standard way (Table 5.9) and rapidly mixed. After mixing, a drop of the solution (0.5–1 ml) was injected into liquid nitrogen and the formed icicle was placed on a SEM stub. Six stubs were prepared in this manner: at 10, 20, 30, 40, 60, and 90 seconds after mixing. Samples were gradually warmed up to the ice melting point and water was sucked off with a capillary. EDX of all samples detected reasonable ratios of Na, Mg, and F components, which indicates presence of neighborite.

It is of interest to observe and analyze the shape evolution of those particles during their first minute of growth (Figs. 5.10–5.13). At the very first seconds of the reaction nuclei rapidly grow needles (Fig. 5.10), which amount only increases during the first 30–50 sec (Fig. 5.11). By the end of the minute amount of those needles is such dense that they start to break, dissolve, and recrystallize from the center of the initial nucleus (Fig. 5.12). Results of such surface rearrangements lead to the formation of clusters in the crystal (Fig. 5.13), which later transform into smooth surfaces.

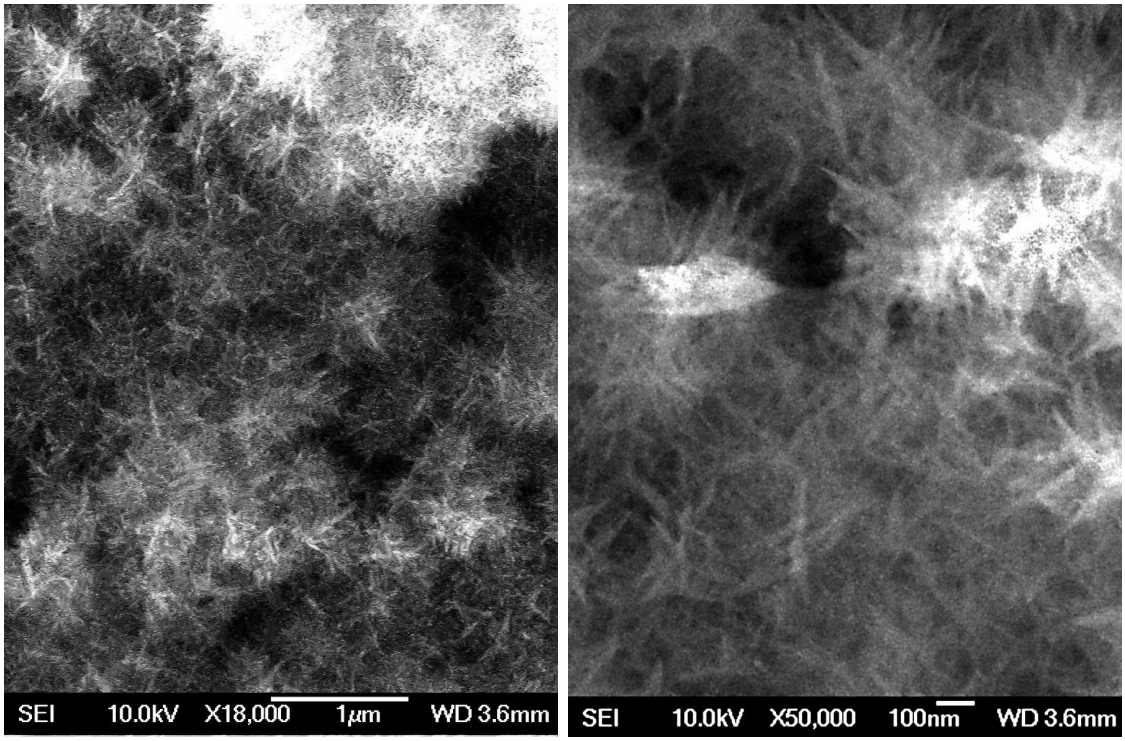

Figure 5.10: Neighborite particles formed under conditions in Table 5.9 after 30 seconds reaction

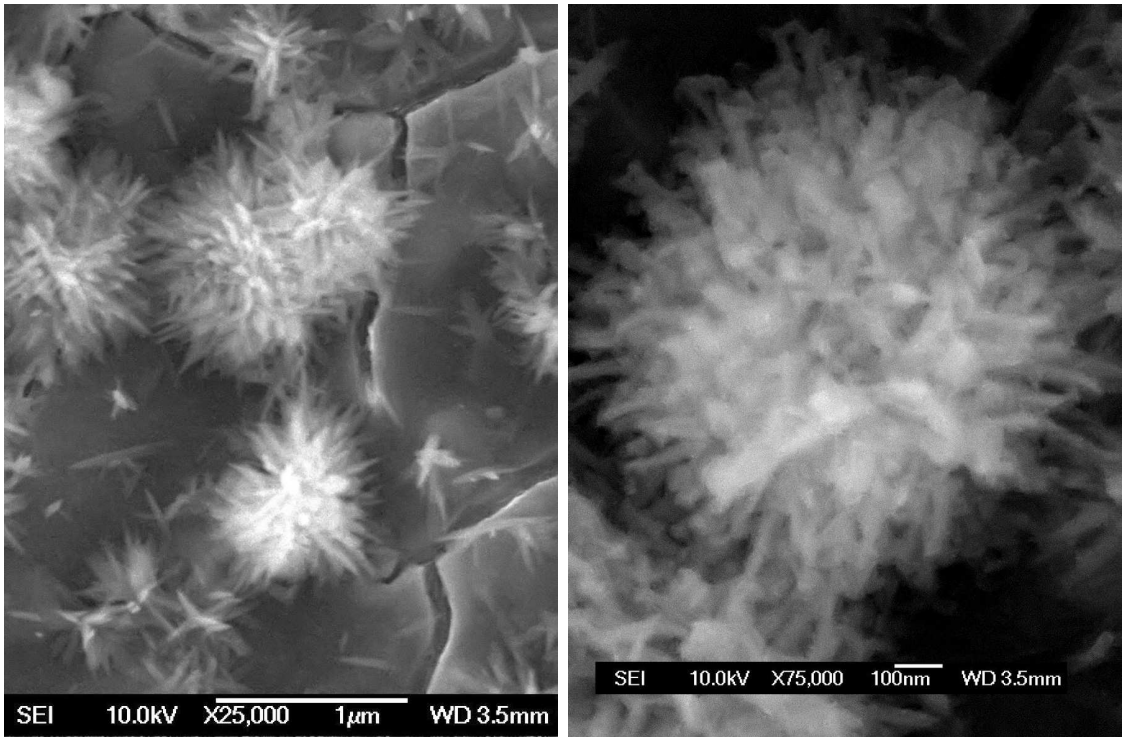

Figure 5.11: Neighborite particles formed under conditions in Table 5.9 after 40 seconds reaction

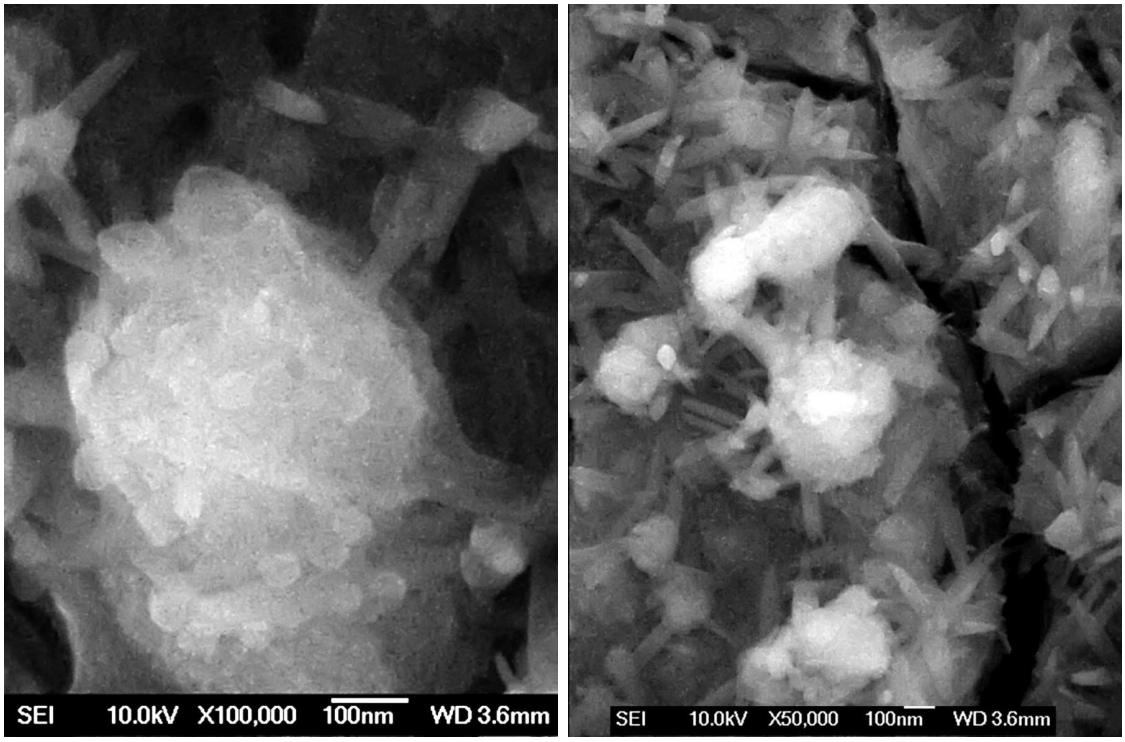

Figure 5.12: Neighborite particles formed under conditions in Table 5.9 after 60 seconds reaction

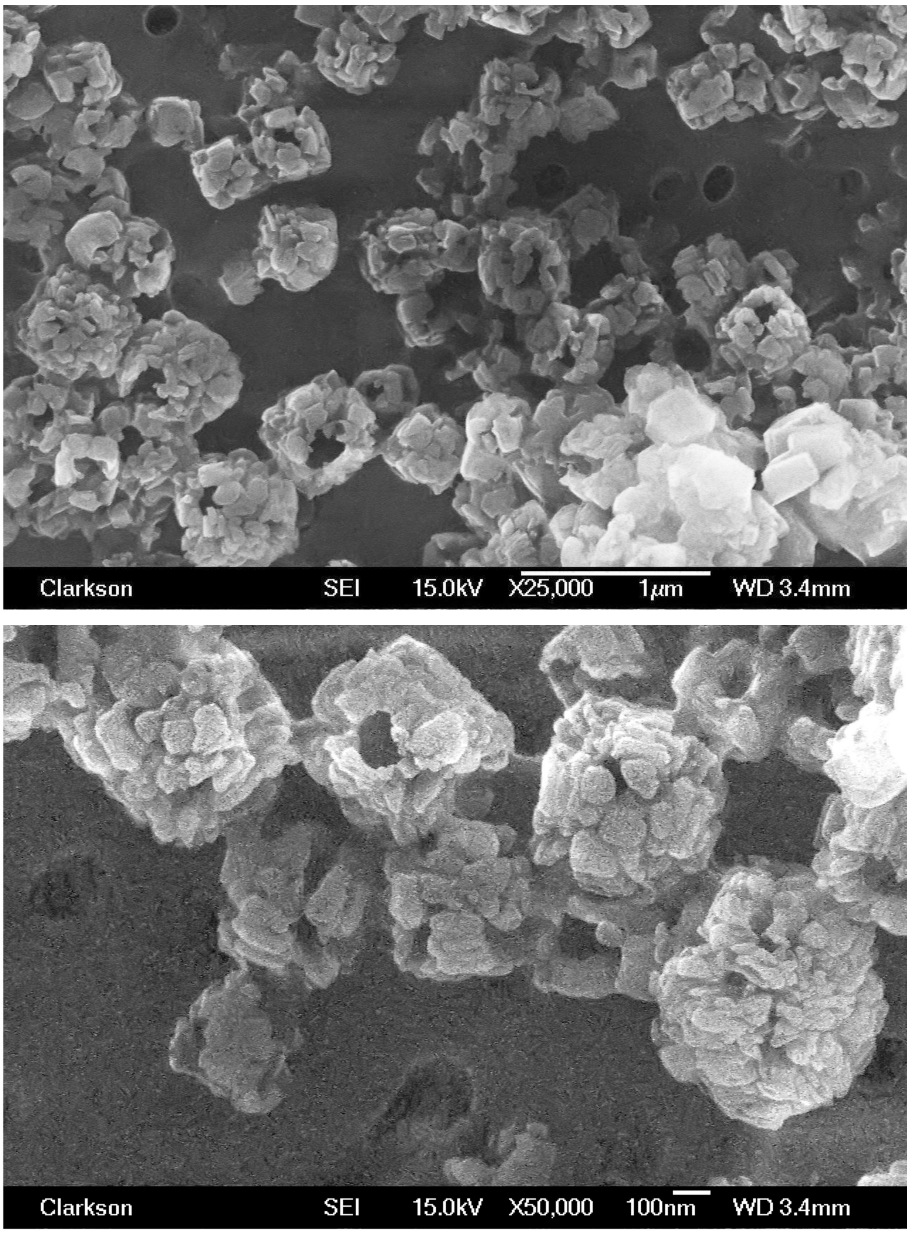

Figure 5.13: Neighborite particles formed under conditions in Table 5.9 after 90 seconds reaction

5.1.6 Structural characterization.

While X-ray diffraction of cubic neighborite particles clearly indicated their composite nature, electron microscopic and etching studies were carried out to substantiate and identify the subunit constituents.

It was noted that exposing cubes in BFTEM mode with a narrow beam (in comparison to the particles surface area) of 200 keV caused slow evaporation from their surface. Fig. 5.14(a) displays a comparison of two cubes: on the left side the effect of a moderate electron beam is seen, while on the right side no radiation was applied. The light area in Fig. 5.14(b) displays the part of the particle surface exposed to the electron beam for approximately one minute. Individual subunits became visible by applying a wider beam and longer exposure to the entire surface of the cube (Fig. 5.14(c)). The size of these subunits of 50–100 nm estimated on the enlarged image (Fig. 5.14(d)) is consistent with the value obtained with X-ray diffraction.

Earlier study [90] has shown that the nature of the products obtained by mixing solutions of NaF and $MgCl_2$ depended in a sensitive way on the concentrations of the reactants as illustrated in Fig. 5.15. This finding did not offer an explanation regarding the mechanism by which cubic particles of neighborite were formed. Current study indicates that their formation proceeds through a two-stage process. When nearly equivalent concentrations of NaF and $MgCl_2$ are used, spheres of MgF_2 are formed (see Section 4.2), which retained of the same shape on aging. However, in sufficient excess of NaF, the first solid consists of MgF_2, that on continued reaction converts into $NaMgF_3$. During that process the excess sodium fluoride is incorporated into crystalline subunits with their simultaneous phase transformation. This mechanism is supported by the enthalpy of formation data at 298 K, which are -1124 kJ/mol for MgF_2 [107], and -1716 kJ/mol for $NaMgF_3$ [108].

To further test the feasibility of a two stage process, additional experiments were

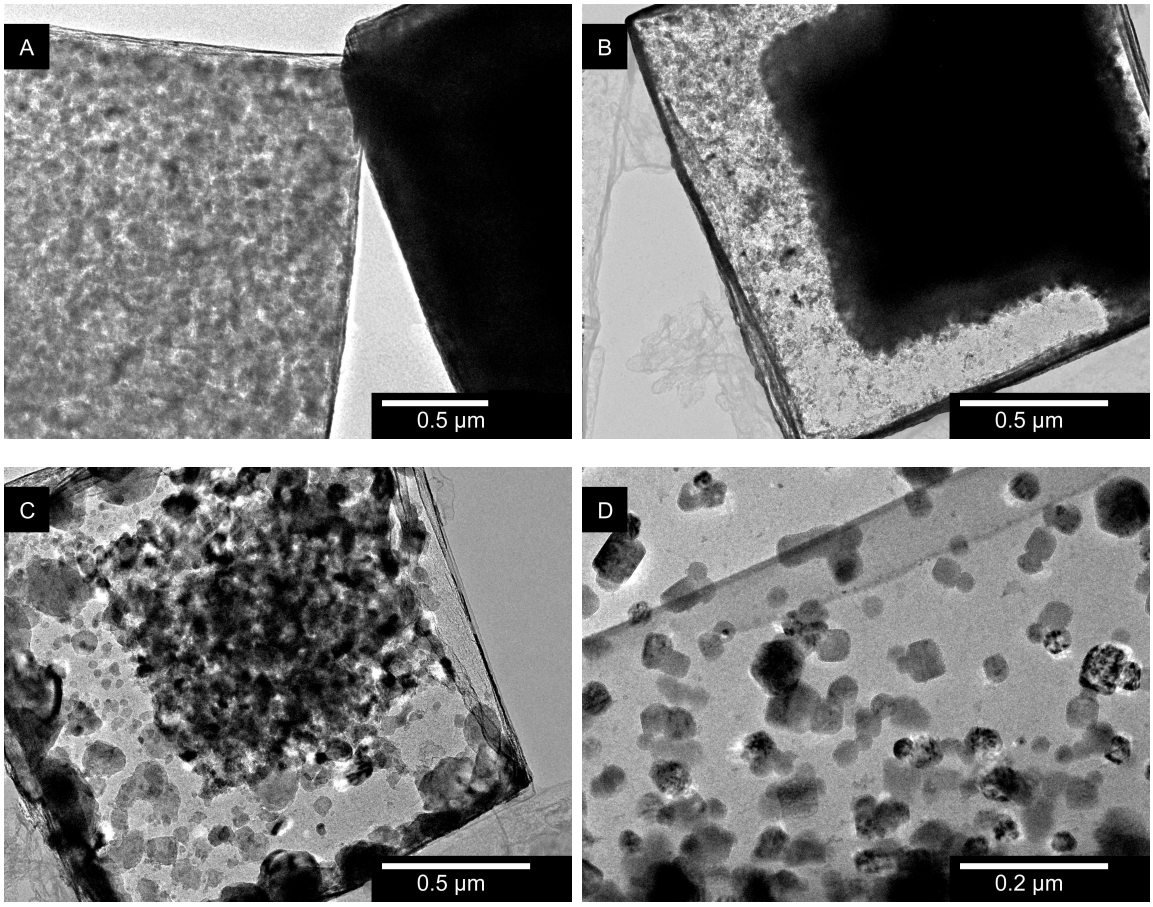

Figure 5.14: TEM observations of $NaMgF_3$ cubic particles. (a) - particle time evolution under electron beam exposure (on the left side a moderate electron beam influenced the particle, and on the right side no radiation had been applied). (b) - a part of the particle surface was exposed to electron beam. (c) - exposed an internal structure of a cubic particle. (d) - displayed subunits of 50–100 nm in size

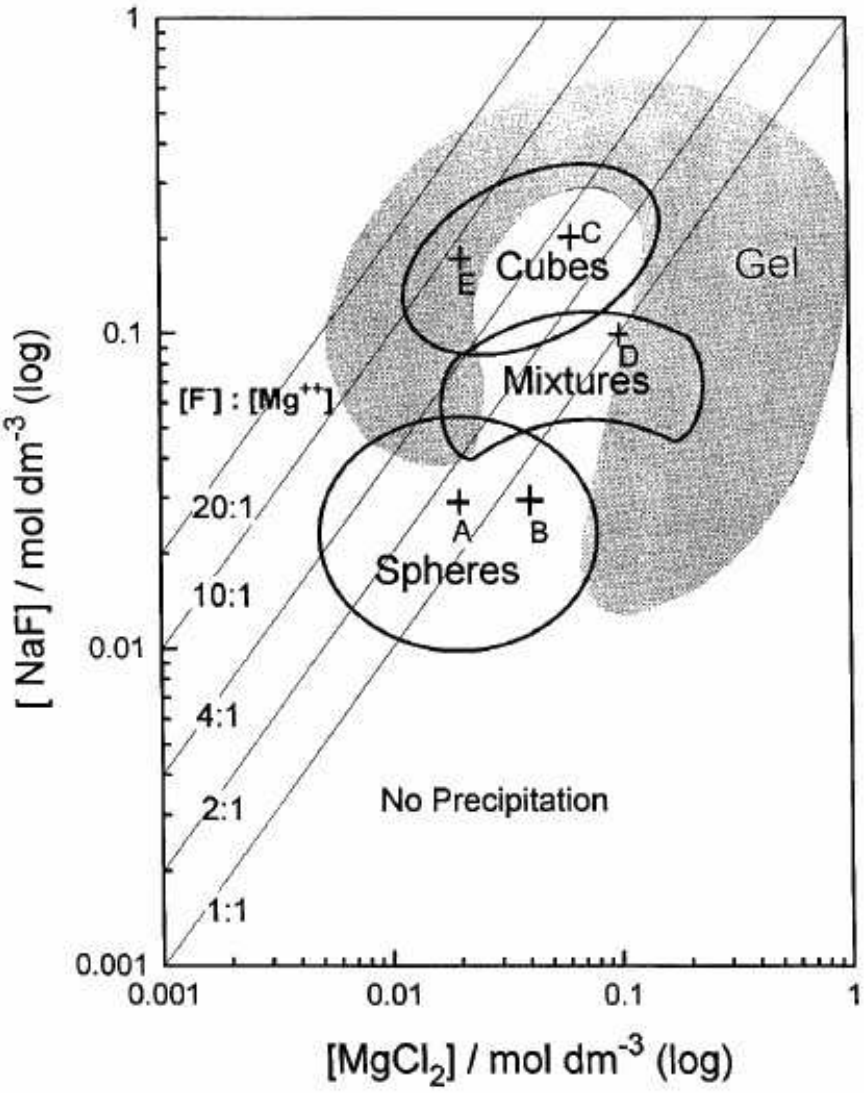

Figure 5.15: Composition domains of precipitates formed by mixing solutions of different concentrations of NaF and $MgCl_2$, aged at 80 °C for 3 hours [90]

carried out as follows. At first, spheres of MgF_2 were prepared by the standard process (sample D_1 Table 4.4). To the dispersion of produced spherical particles (Fig 5.16(a)) additional amount of NaF was added and the entire system was then kept at 80°C for different periods of time. After 2 hours cubic particles of rough surface were observed (Fig 5.16(b)), which on further aging ended up as cubes of smooth surfaces (Fig 5.16(c)). The latter solids had all the same characteristics as the dispersions prepared directly by mixing reactant solutions in excess of sodium fluoride. When dispersions of spherical particles of MgF_2 were first aged for a longer period of time (three hours) and then reacted with additional NaF, transformation into cubes also took place, but the process required much longer time. The resulting cubes were less regular in shape and of broader size distribution. Transformation of MgF_2 into neighborite also took longer time with lower concentration of added sodium fluoride.

The entire transformation process into cubic particles must be affected by the composition of initial spheres of MgF_2 formed by aggregation of nanosize precursors (Fig 5.16(a)). It would seem that on addition of NaF each of these nanosize subunits crystallizes into neighborite (Fig 5.16(b)), which at the elevated temperature are restructured into cubes. During this entire process the original subunits increase in size; while in original spheres they are in the order of 10 nm, in the final cubes their average size is between 50–100 nm.

Based on the findings of this study the following mechanism of $NaMgF_3$ particles growth is proposed and schematically illustrated in Fig. 5.17. Immediately after mixing of the reactants, nucleation of MgF_2 takes place. When nuclei reach their critical size, they convert into $NaMgF_3$ dendrites and grow rapidly, depleting reactant ions from the solution. Once concentration of those ions significantly drops (which takes under one minute) intensive surface rearrangement compactefies crystals shape. Thin needles either dissolve or brake, and released monomers tend to build new

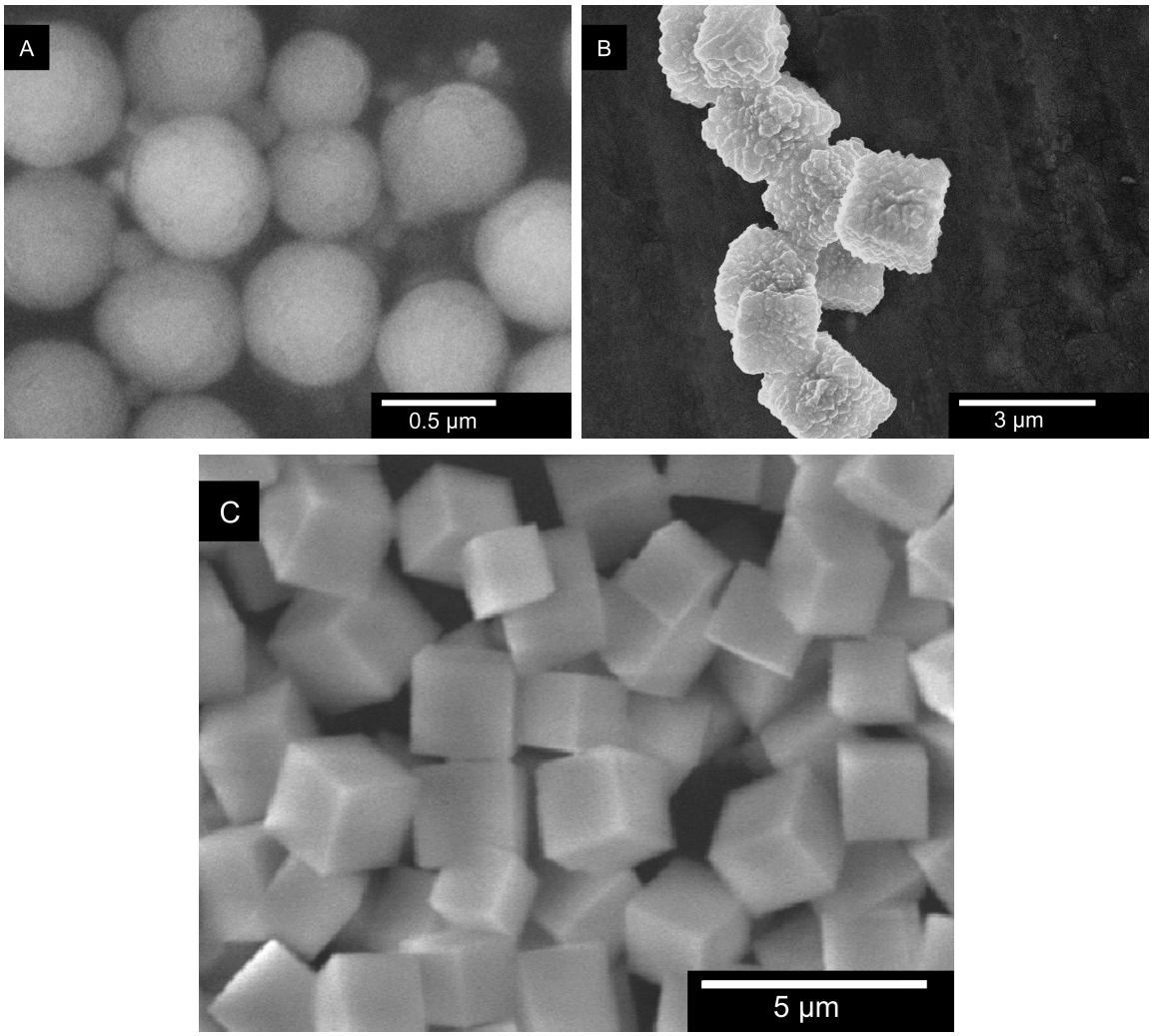

Figure 5.16: SEM images shows transformation of MgF_2 spherical particles into $NaMgF_3$ cubic crystals. (a) - MgF_2 spherical particles formed, when nearly equivalent concentrations of NaF and $MgCl_2$ are used. (b) - as an additional amount of NaF was added, $NaMgF_3$ rough cubic particles were formed on early stage of recrystallization. (c) - $NaMgF_3$ well defined cubic particles formed on aging after surface recrystallization

clusters with lower surface energies from the center of the particle. Which after several hours at 80 °C transforms into cube with smooth faces.

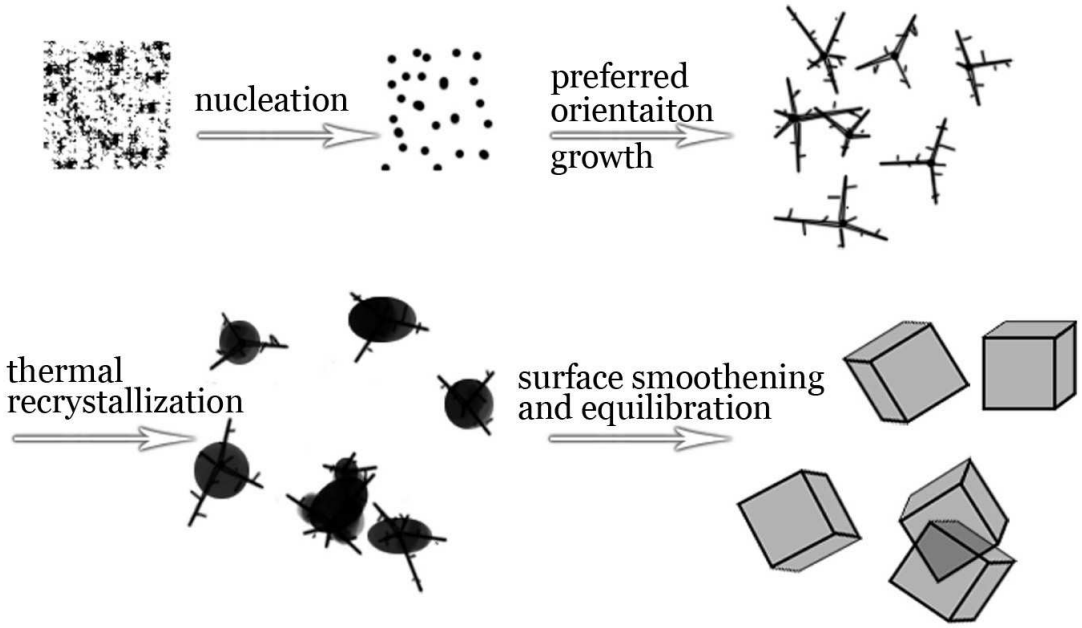

Figure 5.17: Schematic illustration of the mechanism of neighborite particles growth

5.2 Formation of sellaite (MgF_2) crystals

5.2.1 Controlled growth of magnesium fluoride particles

In Sec. 4.2 (Table 4.4) it was shown that using the same reactants one may precipitate particles of the same chemical composition by different mechanisms, resulting in a variety of morphologies. Specifically, by changing the pH and the ionic strength, MgF_2 was prepared as uniform crystals of different habitus or as polycrystalline spheres. These particles form by different mechanisms classified at the bottom side of the triangle shown in Fig. 1.1.

Crystalline particles

Crystalline particles of platelet, cubic, or prismatic shapes, obtained by changing the pH, were formed by diffusional growth (left corner of the scheme in Fig. 1.1). MgF_2 cubes, ranging in size from 50 to 100 nm and having the X-ray diffraction pattern of the mineral sellaite, precipitated under essentially neutral conditions (Table 4.4, B). The skewed shape of their size distribution (Fig. 5.19(c)) is indicative of the diffusional growth mechanism, as modeled by Privman [64]. Under certain conditions, as explained below in this section, these particles may aggregate to form polycrystalline spheres.

The ξ-potential of cubic particles, purified by extensive washing and redispersed in pure water was 64 ± 10 mV and their isoelectric point (IEP) was estimated between pH 8 and 9.5. Thus, cubic particles grew at the pH below the IEP, resulting in the positive charge due to the specific adsorption of Mg^{2+}.

Prismatic $\sim 600 \times 400$ nm single crystals of MgF_2 were formed at acidic conditions (sample C Table 4.4), below the IEP analogously to the previous case. Due to a higher solubility of MgF_2 under such conditions, the supersaturation lower than in neutral

and basic solutions, was responsible for slower crystal growth, resulting in larger elongated particles. Resolved electron diffraction confirmed sellaite crystal structure, and the EDX mapping indicated only Mg and F constituents (Fig. 5.20(b)).

In contrast to the previous two cases, thin MgF_2 hexagonal platelets were formed above the IEP in basic solutions (LiOH or NaOH, pH 11). Using values for the solubility products of MgF_2 ($K_{sp} = 5.16 \times 10^{-11}$) [106] and of $Mg(OH)_2$ ($K_{sp} = 5.61 \times 10^{-12}$) [106], and taking into account concentrations of the reactants (Table 4.4, A), sellaite should preferentially precipitate. Indeed, electron diffraction and powder X-ray diffraction (Fig. 5.18(b)) did not detect any possible hydroxy compounds, such as $Mg(OH)_2$, Mg(OH)F, Mg(OH)Cl. EDX, however, detected some oxygen in all samples A_1–A_4 (Table 4.4), which indicates some adsorption of the OH^- group on the surface of the platelets, as is also indicated by the lower value of the electrokinetic potential ($\xi = 30 \pm 3$ mV) as compared to cubes. Hexagonal shape of the plates and their preferential growth in two dimensions lead to the conclusion that these hydroxyl ions are bound on the (111) face of the nuclei, preventing growth in the direction perpendicular to that face.

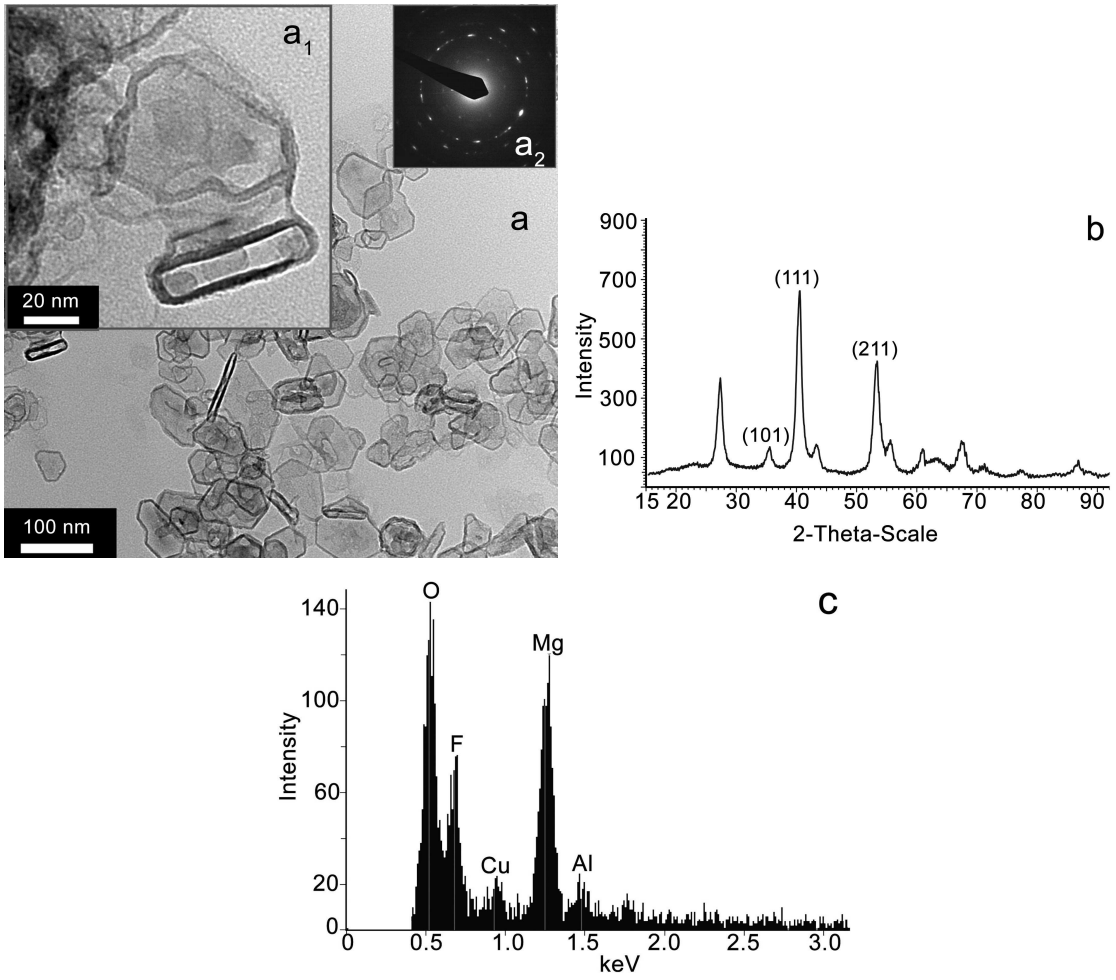

Figure 5.18: Platelet type MgF_2 particles obtained under conditions in Table 4.4 A. (a) Platelet crystals, (a_1) two magnified platelets in different orientations, (a_2) their electron diffraction; (b) X-ray diffractogram, and (c) EDX pattern

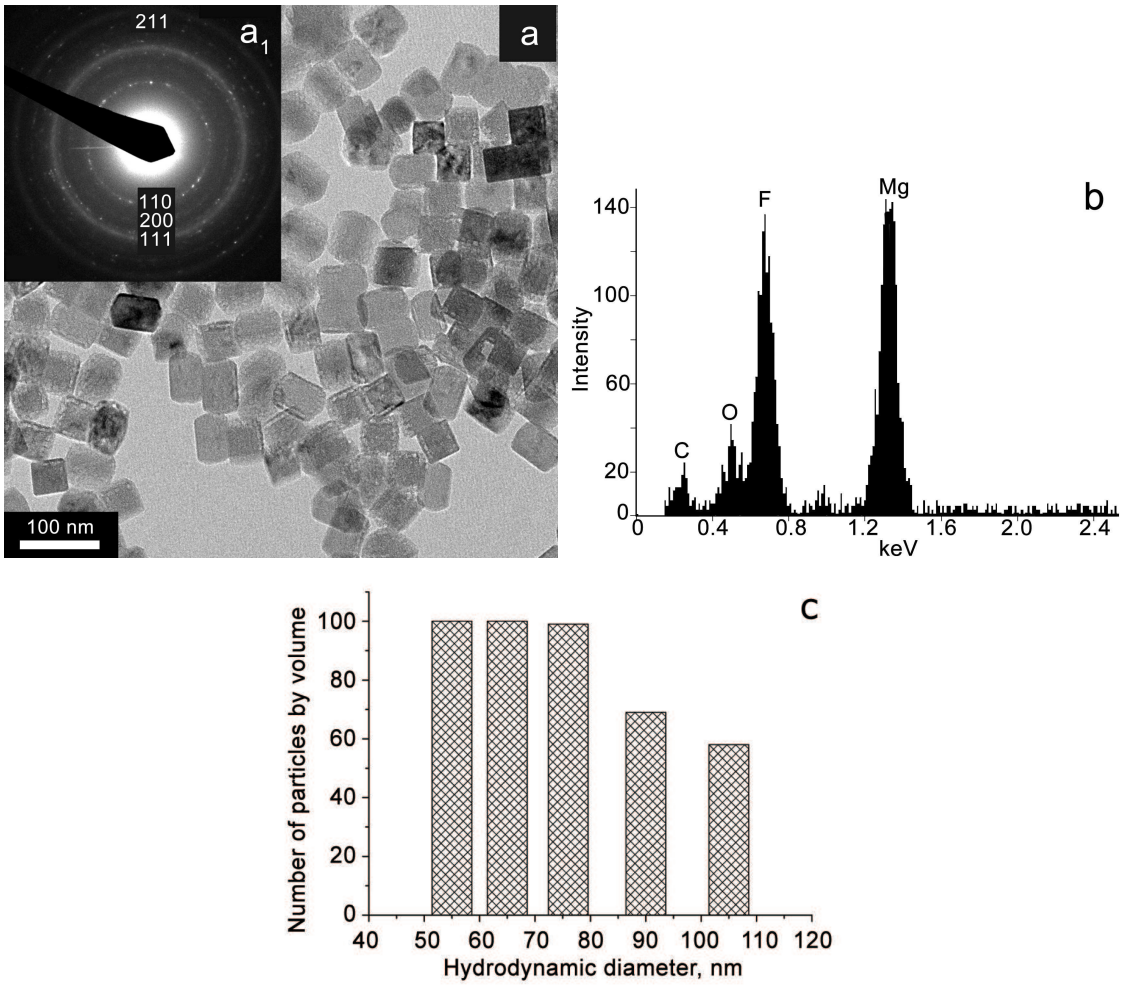

Figure 5.19: Cubic MgF_2 particles obtained under conditions in Table 4.4 B. (a) TEM image and (a_1) electron diffraction of cubic crystals; (b) EDX spectrum; (c) corresponding size distribution

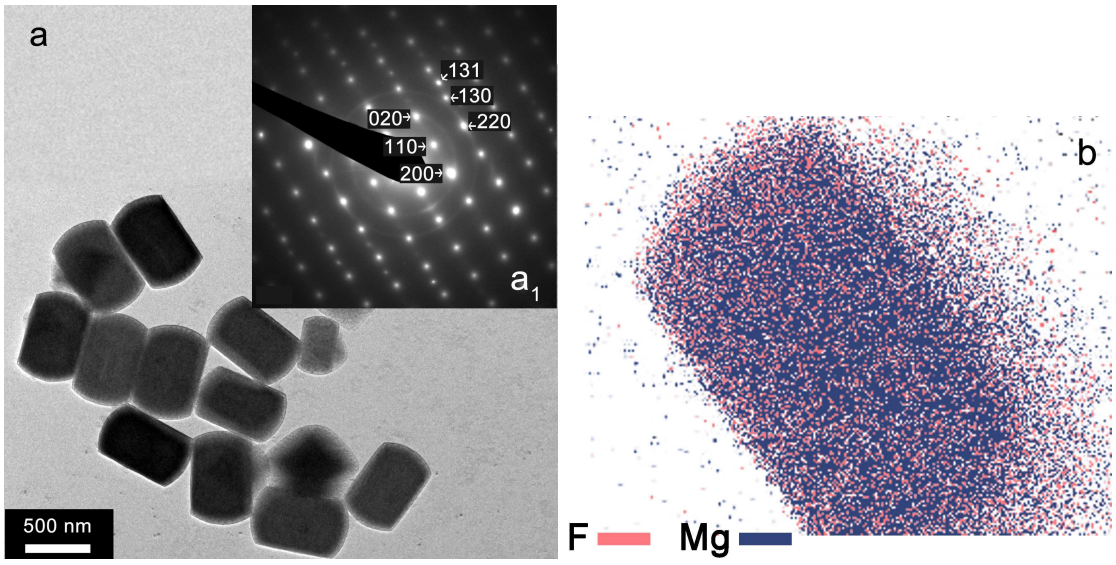

Figure 5.20: Prismatic MgF_2 particles obtained under conditions in Table 4.4 C. (a) TEM image, (a_1) electron diffraction of a single particle; (b) element mapping in scanning TEM mode indicates only magnesium and fluorine

Polycrystalline particles

Two different samples of polycrystalline MgF_2 spheres were obtained, as classified in the right corner of the scheme (Fig. 1.1). The formation of aggregated particles, displayed in Fig. 5.21(a), is caused by sufficiently high ionic strength. Under conditions in Table 4.4, D the resulting spheres consisted of nanosize precursors of 5–15 nm in size, assessed from the broadening of the X-ray peaks by the Scherrer method [100]. Such crystallites uniformity was expected considering their almost identical lattice parameter stresses (Sec. 5.4 Table 5.14). Similar cases have been observed before with metallic particles (Ag and Au [18]) and inorganic salt particles (CdS [11]). A model, describing conditions leading to uniform spheres by such aggregation, has been successfully tested on the cited systems.

Somewhat different conditions are encountered in polycrystalline spheres displayed in Fig. 5.22(a), which consist of cubic subunits (similar to Table 4.4 B). Symmetrical size distribution profile of the spherical particles (Fig. 5.22(d), Table 4.4 E) and loose packing of the cubic subunits (which can be seen in bright and in dark field TEM images as transparent areas inside individual aggregates Fig. 5.22(a–c)) suggest slow aggregation of crystallites into larger spherical particles. The number of such subunits in each aggregate was estimated to be roughly between 13–30. The unique aspect of this system is that the aggregation of the subunits is only observed when magnesium acetate (rather than $MgCl_2$) was used as a reactant in the precipitation process. Consequently, one needs to speculate on the role of acetate rather than chloride anions in this particular case. Since the reactant concentrations and all other conditions were the same as those in sample B (Table 4.4), the adsorbability, size, and the shape of acetate ion must have an effect on the aggregation process. While the ξ-potential for particles prepared with acetate ion was, as a rule, lower by 10 mV than the value obtained with Cl^-, this difference is not sufficient to account

for lesser stability of the precursors. A possible explanation may be based on the the adsorption of acetate ions, which would certainly involve carboxyl group attachment to magnesium sites on the particles surfaces and consequently, tail-to-tail interaction of the approaching subunits.

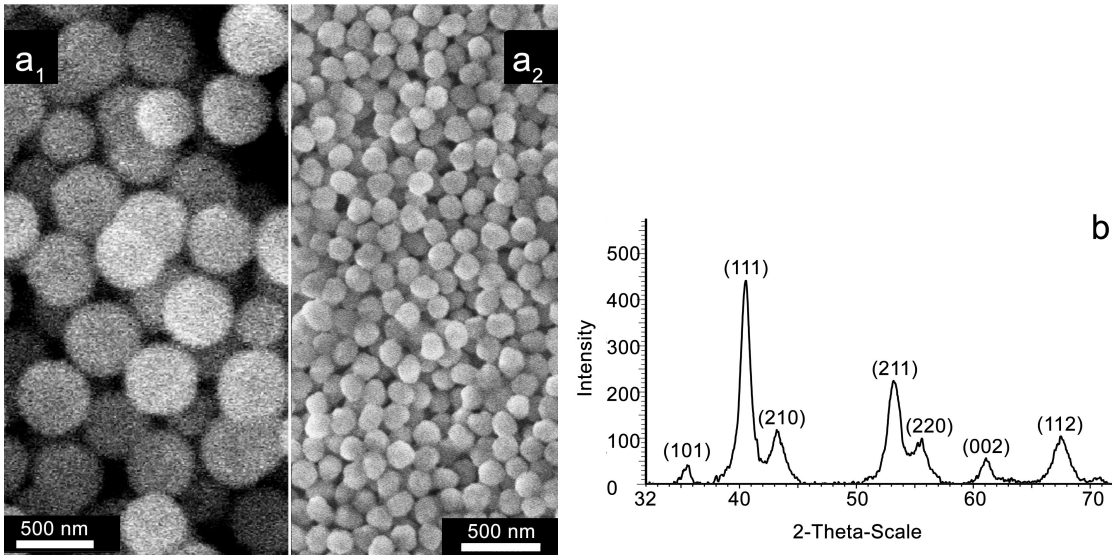

Figure 5.21: (a) Spherical polycrystalline particles obtained under conditions in Table 4.4 D of two different sizes [66, 90]; (b) their X-ray diffraction

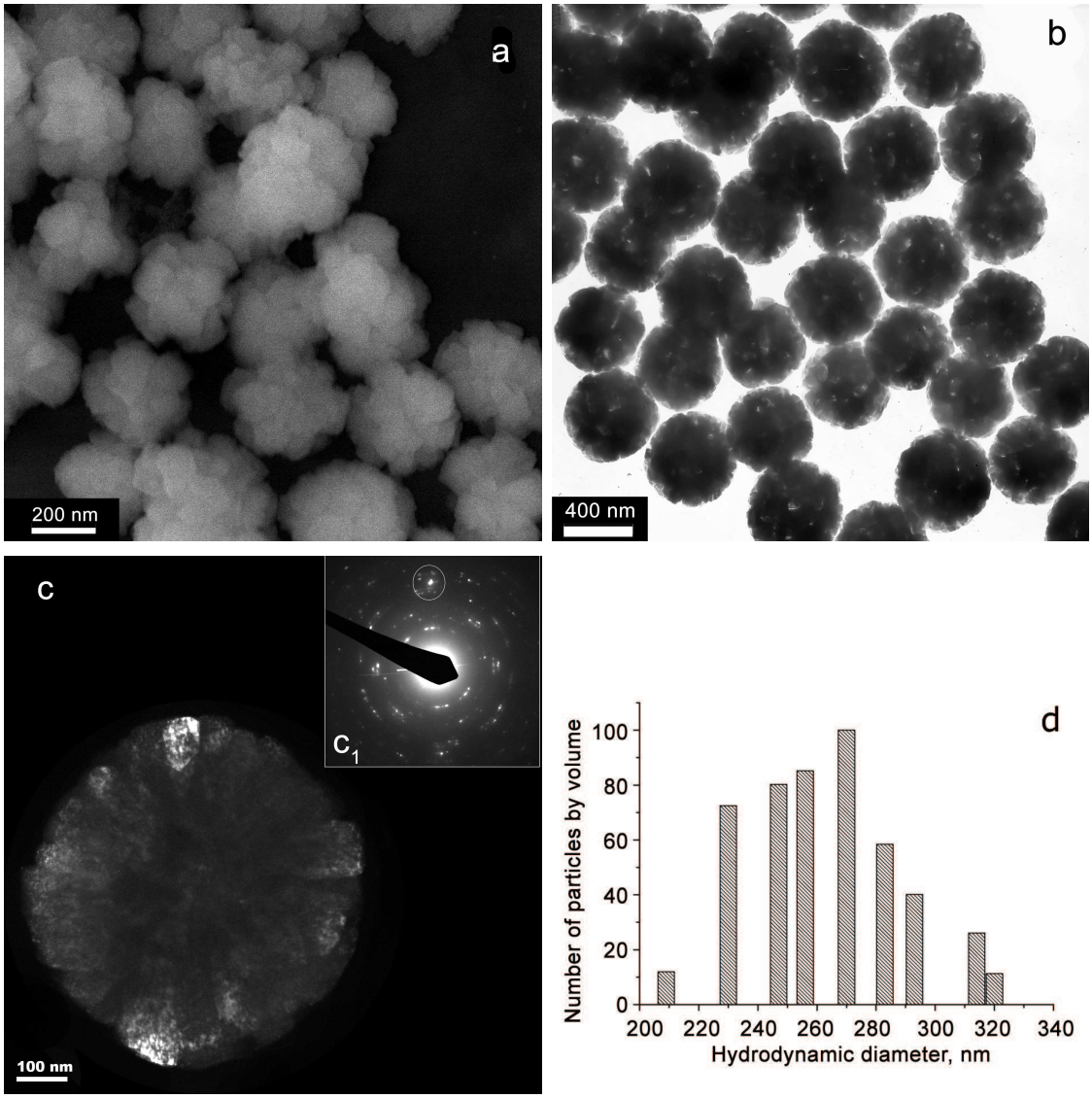

Figure 5.22: (a) SEM and (b) TEM images of spherical particles obtained under conditions in Table 4.4 E. (c) Dark field image of a single particle, with (c_1) corresponding electron diffraction; (d) size distribution of these particles obtained by light scattering

5.2.2 Time evolution growth of magnesium fluoride particles

Time evolution of sellaite particles growth is of interest, because it can be directly compared to the results of self-assembled nucleation growth theory described by Privman [64]. Numerous approaches were sought to achieve appropriate time scale of early stages of MgF_2 formation. Employed experimental procedures did not allow samples to be prepared in less than 1 minute and, consequently, followed the evolution of already formed aggregates. Therefore, utilizing *freeze-dry* method (see Sec. 3.1.8) and setup in Fig. 3.12 yielded results for reaction times as short as 5 seconds.

Aqueous solution of NaF and $MgCl_2$ at equal molar concentrations were prepared according to the Table 4.4 D_1 and thoroughly mixed in tubing of predetermined length. Time of mixing in such tube was tested with two colored solutions. Those solutions lose their color when fully mixed. By such discoloration it was measured that two reactants entirely mix in $\sim$0.5 sec at lowest pumping rates.

The length of the mixing tube as well as the rate of pumping controlled total reaction time. A cup of liquid nitrogen at the end of the mixing tube instantaneously froze the reaction, collecting samples of the specific lifetime. Results acquired from electron micrographs (Fig. 5.23) and laser particle sizer are summarized in the Scheme 5.24.

It was experimentally estimated that induction period for nucleation took approximately 3–4 seconds, after which burst nucleation took place for 6–7 more seconds. From electron micrographs, the measured size of those nuclei, was between 3 and 8 nm. Assuming that the critical nuclei are of spherical shape and of $\sim$20 $\mathring{A}$ in diameter, it was possible to estimate a number of monomers needed to build such nucleus.

Particularly, primitive cell volume of MgF_2 is 65.22 $\mathring{A}^3(AppendixD)$ and has tetragonal crystal structure. Density packing of atoms in tetragonal structure is 0.586 [109]. Accounting that, a number of monomers needed to form a nucleus of a

critical size is:
$\frac{\pi 20^3}{6} \times \frac{1}{65.22} \times 0.586 \approx 37.$

Next, in Fig. 5.23(b) 11 seconds old particles of two different sizes are shown. Smaller solids (3–8 nm) are the newly formed nuclei by burst nucleation, whereas larger (15–30 nm) are diffusionally grown crystals. Presumably, particles of ∼30 nm are the oldest solids.

By the second 15 (Fig. 5.23(c)) there were no new nuclei formed. Instead, the aggregation of so formed nuclei is initiated. resulting in particles of 25–35 nm in diameter (Fig. 5.23(c)). During the next several seconds these secondary particles continue to grow by incorporation of additional nuclei (Fig. 5.23(d), (e), (f)). This aggregation process continues for several minutes, yielding dispersion of MgF_2 polycrystalline spheres of modal diameter ∼800 nm. The complete process of MgF_2 growth is schematically given in Fig. 5.24

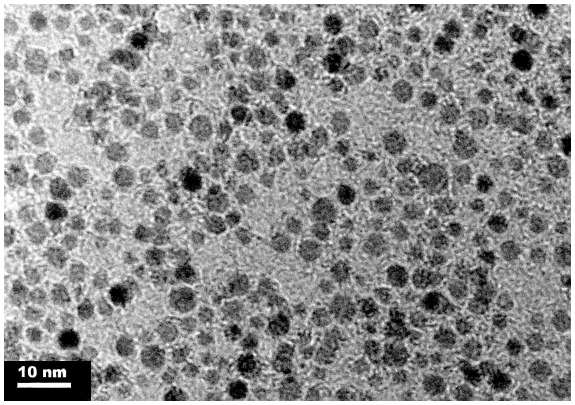

(a) 4.9 sec

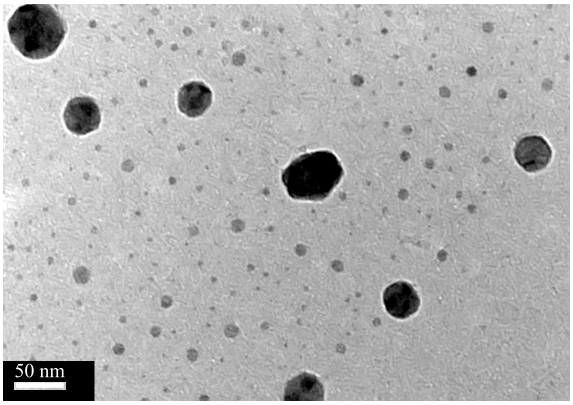

(b) 11 sec

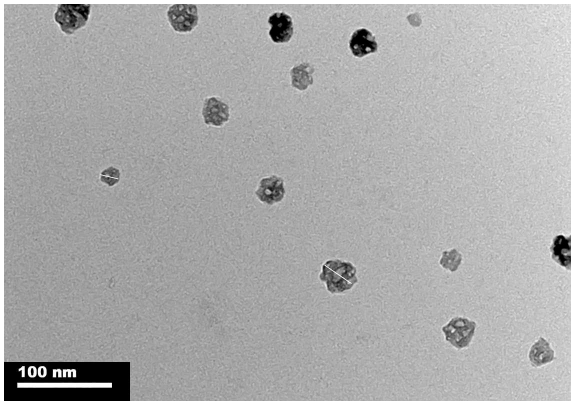

(c) 15 sec

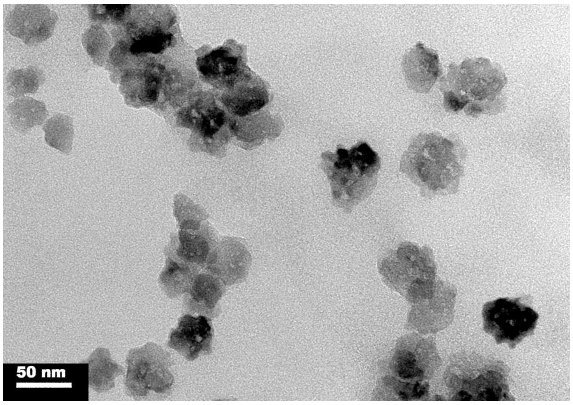

(d) 18 sec

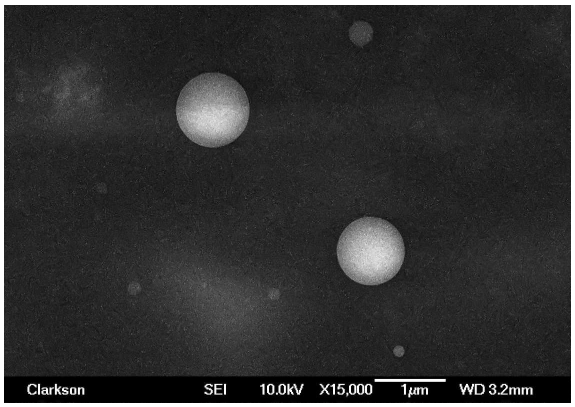

(e) 20 sec

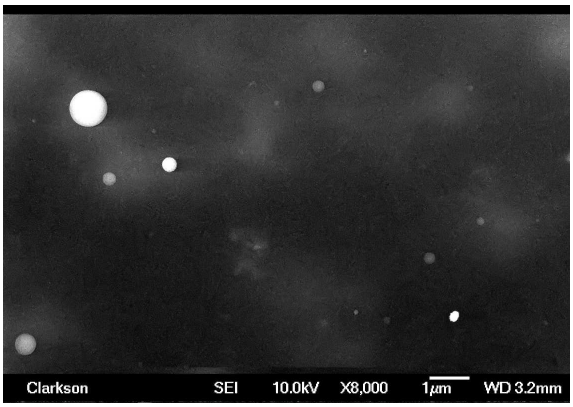

(f) 20 sec

Figure 5.23: Time evolution growth of MgF_2 particles

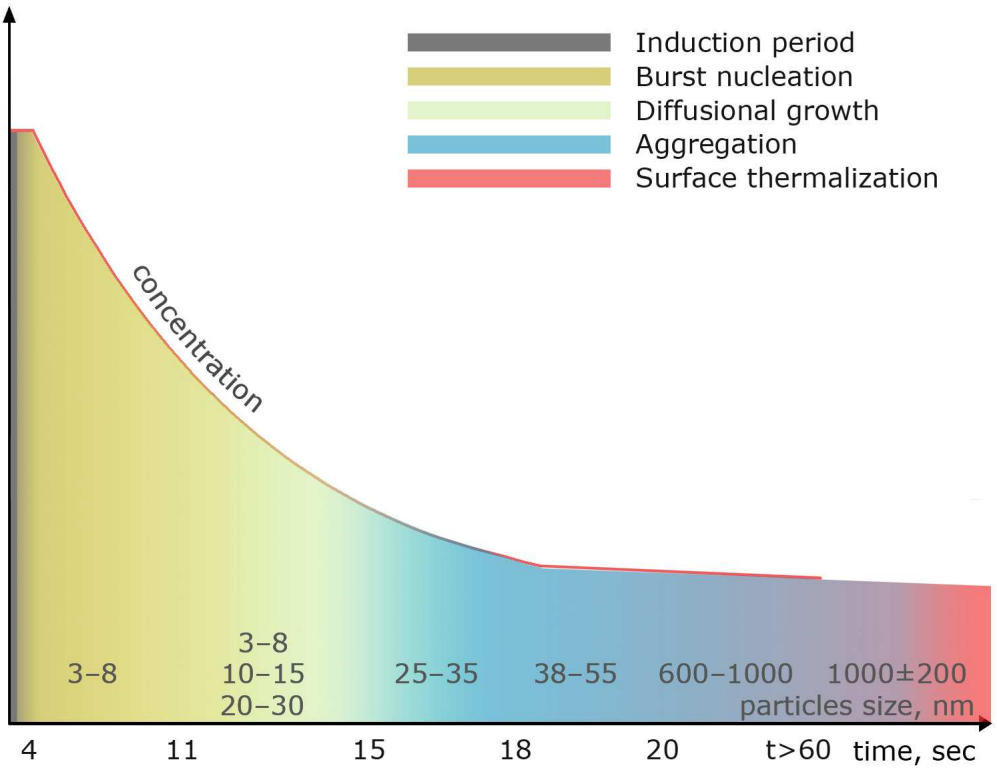

Figure 5.24: Schematic time evolution growth of MgF_2 particles

5.3 Formation of galena (PbS) crystals

5.3.1 Hydrolysis of thioacetamide (TAA)

As described in Sec. 4.3, TAA (C_2SNH_5) was selected as the source of sulfide ions. While in numerous studies it was assumed that TAA rapidly decomposes, Swift et. al. [105] showed that such assumption was not valid. In fact, the decomposition of TAA is a complex process, which is sensitive to temperature and the pH. There were three pH ranges defined [105] that affected differently the hydrolysis of TAA.

At $pH < 3$ precipitation of lead sulfide is driven primarily by the hydrolysis of thioacetamide as:

$$-\frac{d[PbS]}{dt} = k[TAA][H^+]$$

where k is the parameter dependent on temperature [105].

T, °C	$k, L\ mol^{-1}\ min^{-1}$
90	0.21
80	0.098
70	0.089
60	0.019

At $3.5 < pH < 5$ the rate of PbS precipitation is affected by the proton concentration according to:

$$-\frac{d[Pb(II)]}{dt} = k\frac{[Pb(II)][TAA]}{[H^+]^{1/2}}$$

For example, at 90 °C –d[Pb(II)]/dt = 0.113 ($L^{1/2}$ $mol^{-1/2}$ min^{-1}). At $pH > 5$ the rate of lead sulfide precipitation is almost 1000 times faster than the rate of H_2S formation by hydrolysis of TAA.

Swift et. al. [105] showed that temperature plays a major role in the kinetics of TAA hydrolysis. In this study reactants were mixed in accordance to Table 4.5

but experiments were carried out at 23, 50, 60, and 90 °C to test the effects of the temperature on the formation of PbS particles (Table 5.10).

Table 5.10: Temperature effect on the time of the formation of PbS particles

Sample	T, °C	Time, h
B_1	20	20
B_2	50	6
B_3	60	5
B_4	90	1

Crystals of similar morphologies were obtained over the entire temperature range, but after different times. At elevated temperatures the formation of the particles was significantly faster due to shorter decomposition time of TAA comparatively to the room temperature. For example, it took 20 h for PbS to be formed at 23 °C and only one hour at 90 °C.

5.3.2 Solubility of lead nitrate in aqueous solution of nitric acid

It was shown by Ostanova et. al. [110] that the solubility of $Pb(NO_3)_2$ decreases in aqueous solutions with higher concentrations of nitric acid. Therefore, at essentially any pH precipitation of lead sulfide particles will be limited either by solubility of $Pb(NO_3)_2$ or by decomposition of TAA. For example, at lower pHs the rate of TAA decomposition increases proportionally to $[H^+]$, whereas the solubility of $Pb(NO_3)_2$ significantly decreases. As a result, the formation of PbS particles is primarily driven by availability of the lead ion. In contrast, at neutral and basic pH conditions the rate of PbS formation is predominantly controlled by the hydrolysis of TAA. Only in slightly acidic conditions both solubility of lead nitrate and hydrolysis of TAA

contribute equal amount of constituent ions needed for PbS precipitation.

5.3.3 Effect of the pH on the formation of PbS particles

To test the pH effect, reactants were mixed according to the reference experiment (Table 4.5) in the presence of either HNO_3 or NaOH as specified in Table 5.11. It was found that precipitation of PbS in acidic media took place without the formation of any intermediate complexes. In contrast, in basic conditions $Pb(OH)_2$ may precipitate first, which then transforms into PbS in the presence of TAA.

Table 5.11: Effect of the pH on the final size of lead sulfide particles precipitated at T=50°C

Sample	pH	Size, nm	Shape
D_1	1	2000±500	Cubic
D_2	2	1000±250	Cubic
D_3	3	350±50	Cubic
D_4	4	350±50×50±10	Brick
D_5	11	20±10	Prismatic

In all cases in acidic media (D_1–D_4) either cubic or brick-like particles were obtained, but of different sizes. For example, at pH = 1 crystals of 2±0.5 μm of almost cubic morphology precipitated (Fig. 5.25(D_1)); at pH = 2 slightly smaller particles of 1±0.25 μm in size were detected (Fig. 5.25(D_2)). Modal length of the solids prepared at pH 3 was 300 nm (Fig. 5.25(D_3)), and at pH = 4 mostly platelets of 300–400 nm in length and ∼50 nm thick were formed (Fig. 5.25(D_4)).

In sample D_5 TAA and lead nitrate were mixed in the presence of NaOH at pH 11 resulting in instant precipitation of PbS nanoparticles of 10–30 nm in size (Fig.5.26(a)). When the pH was adjusted to 1 with nitric acid, aggregation of the

nanocrystals was observed resulting in spherical particles of several microns across (Fig. 5.26(b)).

Manipulating the pH during PbS nucleation and growth allowed to control their size and, to some extent, shape only by selecting different regimes of TAA decomposition (Sec.5.3.1). Based on the results of this study the following general trend was established in the formation of PbS particles. The lower was the initial pH the slower was the formation of PbS crystals but the larger were final particles with smother surfaces. On the other hand, the higher was the pH the faster was the reaction resulting in dispersions with nanocrystals of down to 5 nm in size.

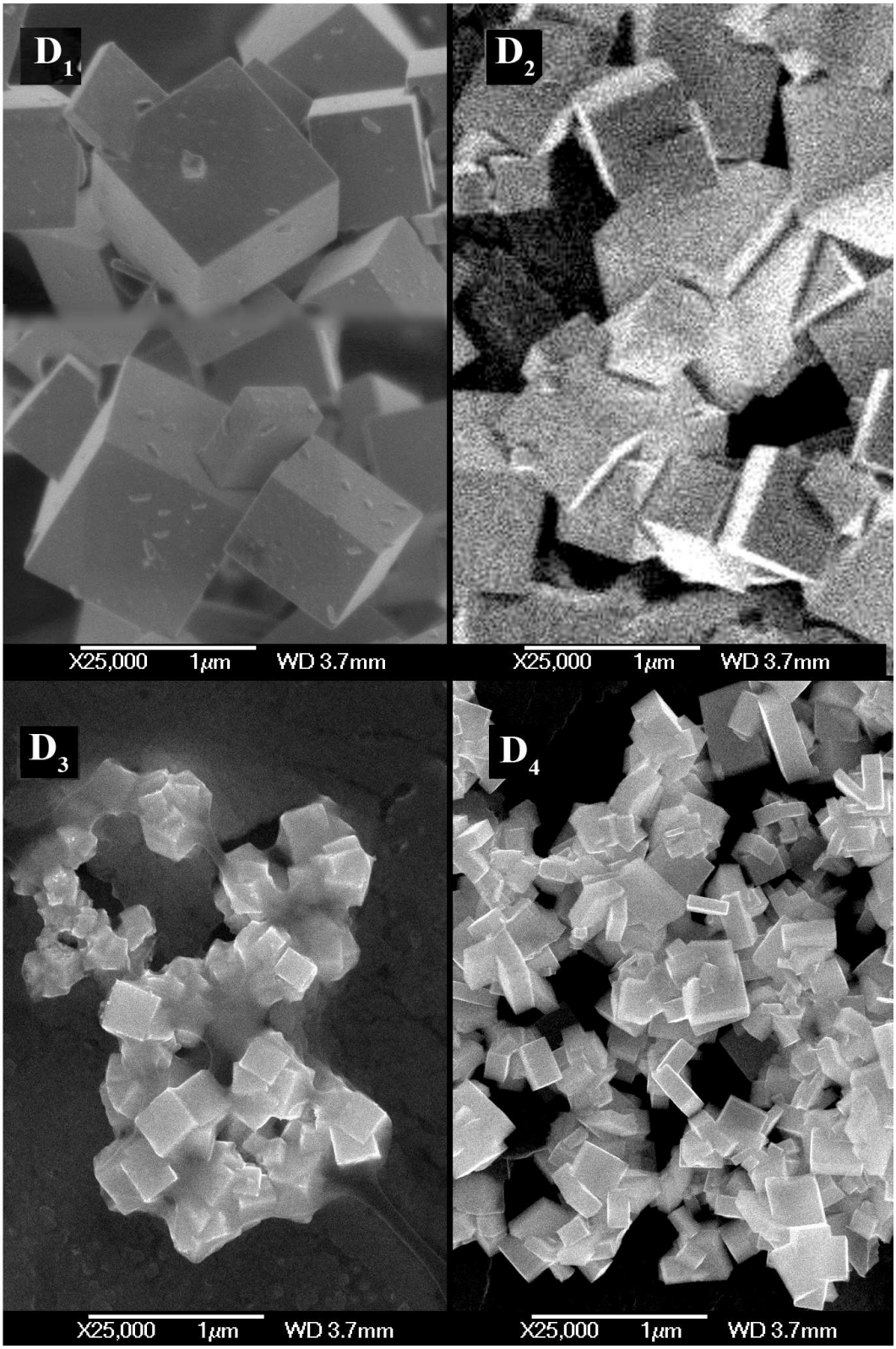

Figure 5.25: PbS particles of different sizes and aspect ratios prepared at the pH values 1–4 (Table 5.11)

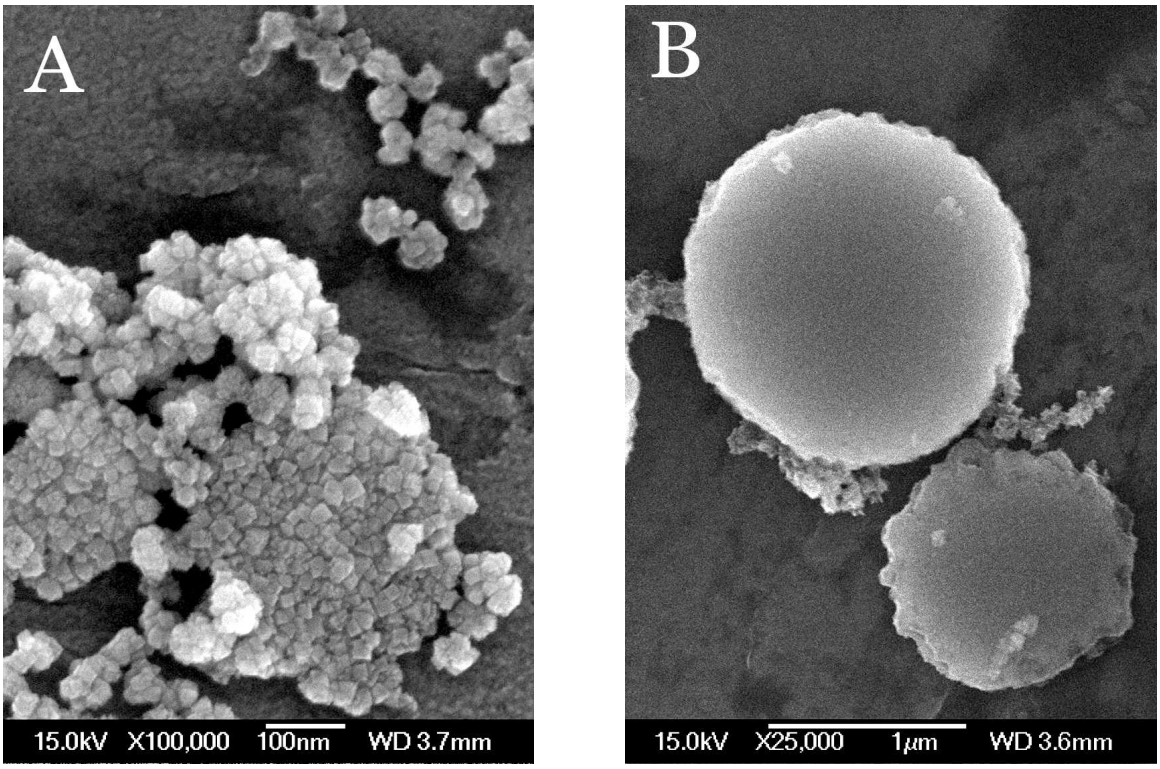

Figure 5.26: (a) Lead sulfide nanoparticles obtained by precipitation at pH 11, and then (b) coagulated when the pH was adjusted to 1 (Table 5.11 D_5)

5.3.4 Time dependent growth of lead sulfide particles

Stages of growth of lead sulfide particles were investigated from size distribution data, obtained after different times during the reaction. When reactants were mixed in accordance to Table 5.12, very few nuclei were formed during first ten minutes. Their concentration in the solution was below the sensitivity threshold of the available laser particle sizer. However, from the electron micrographs (Fig. 5.27 (left)) it was possible to estimate the size of the formed nuclei, which was approximately 10–20 nm.

Table 5.12: Conditions used to investigate PbS particles growth at T=50 °C

C_2H_5SN		$Pb(NO_3)_2$		HNO_3		H_2O
C, mol dm^{-3}	V, cm^3	C, mol dm^{-3}	V, cm^3	C, mol dm^{-3}	V, cm^3	V, cm^3
0.05	2	0.012	2	0.48	10	6

With time, the concentration of solids in the reactor increased, allowing for stable readings of size distribution in the particle sizer. In Fig. 5.28(top) the data were collected from both electron micrographs and particle sizer. It can be clearly seen from the figure how modal size of the PbS crystals increases with time and their size distribution broadens. If the size of the particles is being plotted against time (Fig. 5.28 (bottom)), three distinct stages of PbS growth can be revealed.

In the first five minutes concentrations of Pb and S ions were at their highest values. During this – induction – period PbS nuclei of critical size were formed. Then, in the next 25 minutes the size of the formed particles increased linearly by the factor of three, depleting available sulfide and lead ions. This linear behavior indicates rapid diffusional crystal growth, which is also supported by broadening of the size distribution profile [71] (Fig. 5.28 Top).

During the next five hours, size of the particles also increased linearly, but only

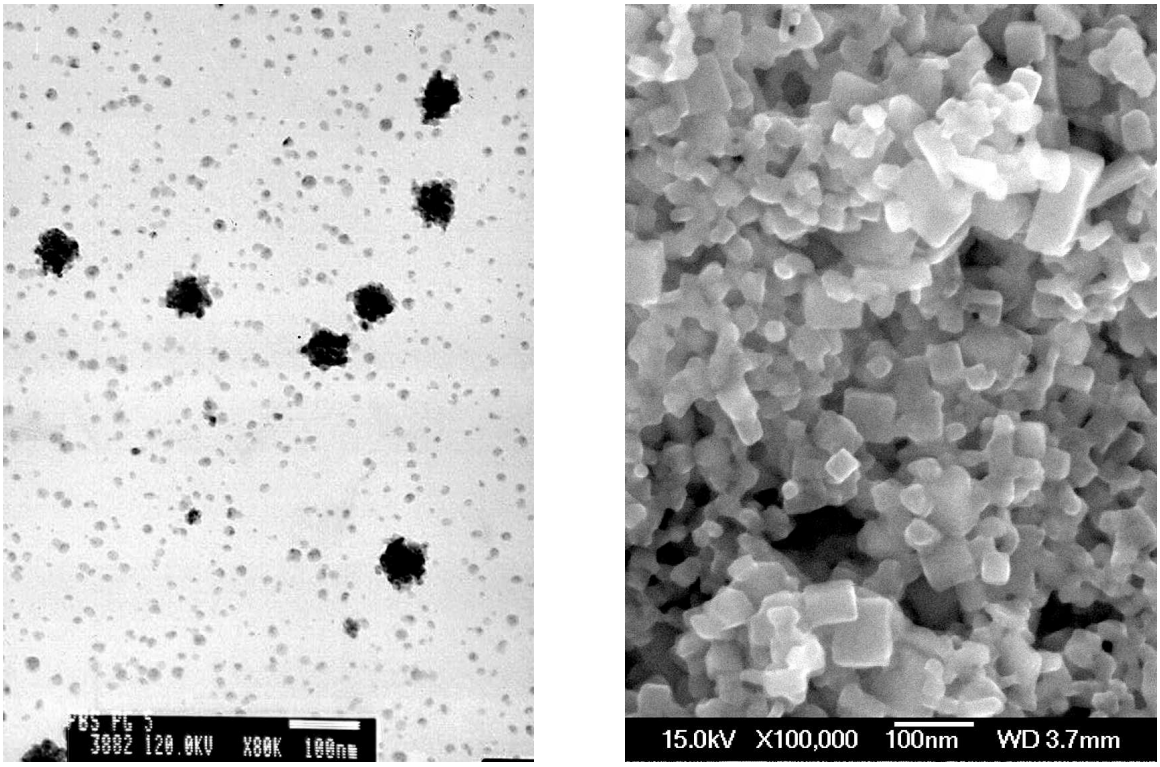

Figure 5.27: Lead sulfide particles formed during first five minutes (left), and after five hours (right) prepared under conditions in Table 5.12

by the factor of two. Such trend was controlled by the hydrolysis of TAA, which was a slow process (see Sec. 5.3.1). At this stage no additional nucleation was observed, but rather continuous crystal growth resulting in particles of 90±20 nm in size (Fig. 5.27 (right)).

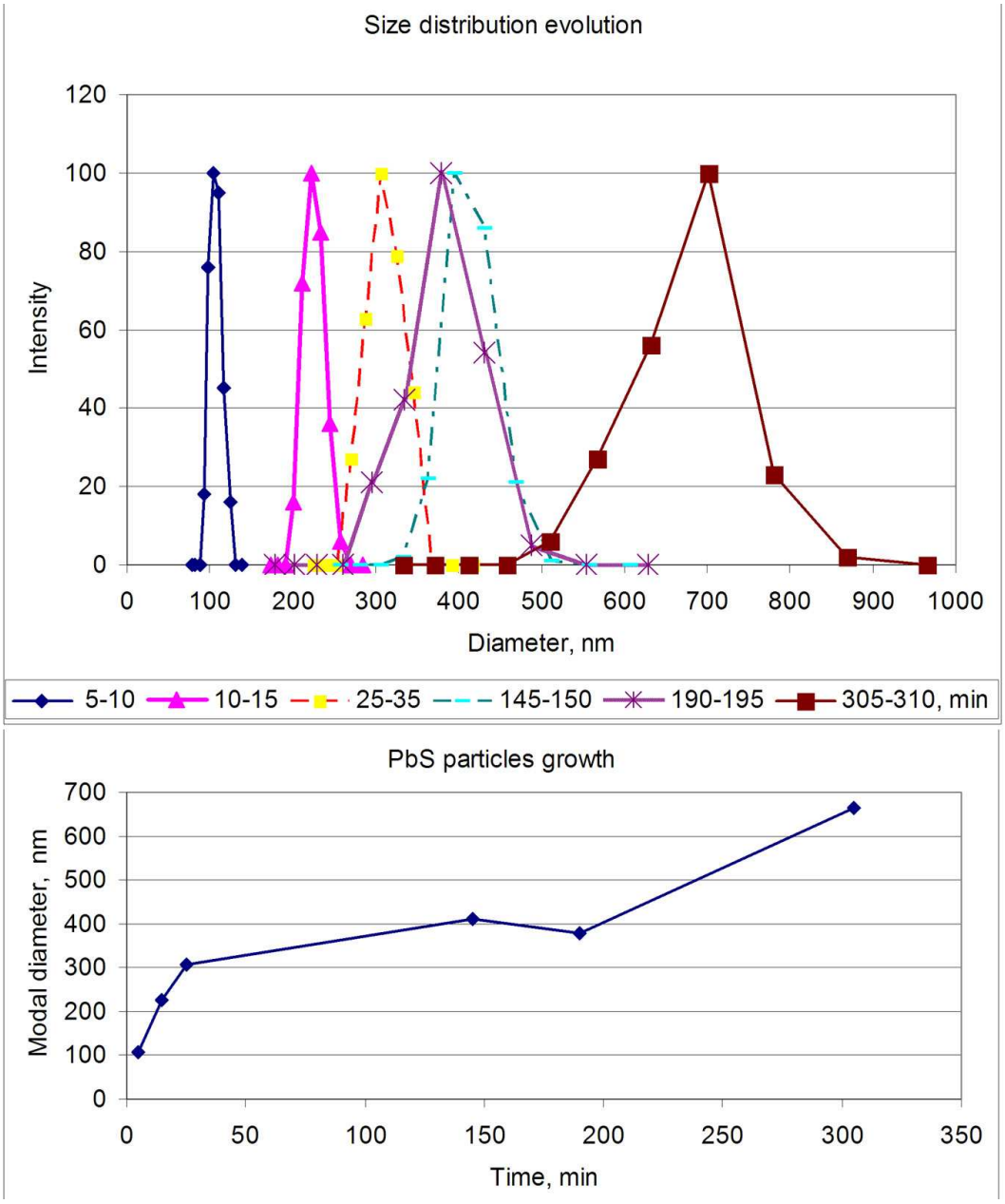

Figure 5.28: Time evolution of lead sulfide particles prepared at 60 °C under reference conditions (Table 4.5). (Top) – propagation of the size distribution profile with time (area under each profile is *not* normalized to the amount of matter). (Bottom) – average particles size vs. time

5.4 Surface tension and shape of the colloidal particles

Surface tension of nanoparticles is one of the important experimental parameters needed in an effort to elucidate the mechanisms of the formation of fine particles [64, 71, 72]. Cited theoretical studies, authors suggested to use surface tension as a fit parameter due to the absence of valid experimental values in the literature. In the following section fairly simple and fast technique for obtaining surface tension values of the microcrystals is reviewed and applied. Particularly, the surface tension is explicitly calculated for magnesium fluoride particles of two different shapes: spherical and platelet. And the correlation between microscopic shape and surface tension is constructed.

Orowan (1949, unpublished) was the first who demonstrated the existence in crystalline solids of force analogous to surface tension in liquids, which is also known as the stress in a liquid surface. Shuttleworth and Nicolson [111,112] attempted to widen this concept so that it can be applied to crystal faces.

In those studies, the surface stress is defined analogously to stress in elasticity. Utilizing this concept and the relation of the surface tension of a crystal to the surface free energy: $\sigma = F + A(dF/dA)$ [111], where F is Helmholtz free energy and A is the area of a surface; Shuttleworth [111] showed that the surface tension may be expressed with good accuracy for particles of different shapes by:

$$\sigma = -\frac{3\Delta a}{4\beta} \tag{5.1}$$

where β is compressibility and Δa is the absolute change in the lattice parameter.

Simultaneously, Nicolson [112] theoretically substantiated the contribution of various kinds of forces to surface tension in the cubic planes. The original work contains initial equation applicable for any crystal structure. For example, in NaCl type cubic crystals surface tension contribution may be summarized as follows:

Force	Contribution
Coulomb	$\sigma_e = 0.4386e^2/a^3$
Van der Waals	$\sigma_W = -(2/a)^8(0.2565(\mu_+^+ + \mu_-^-) + 0.2880\mu_+^-)$
Repulsion	$\sigma_{rep} = -(2/a)^{11}(0.1038(\lambda_+^+ + \lambda_-^-) + 0.0530\lambda_+^-)$
Ion dipole	$\sigma_{id} = -2.920e(p_+ + p_-)/a^4$
Like dipoles	$\sigma_{ld} = -38.32(p_+^2 + p_-^2)/a^5$
Unlike dipoles	$\sigma_{ud} = 140.1p_+p_-/a^5$

Here e is the electron charge, a is the interatomic spacing, μ and λ are the equation parameters, which can be obtained from [112], p^+ and p_- are the dipole moments acquired from positive and negative ions respectively.

Later Stoneham [113] refined Eq. 5.1 for microcrystals of various geometries, and, more importantly, proposed technique for the surface tension calculation from lattice parameter changes. Although, new equations more accurate, in this study Eq. 5.1 was used mainly due to the fact that not all particles in the inspected dispersions were necessarily of the same geometrical morphology.

The surface tensions of MgF_2 microcrystalline platelets (Fig. 5.18(a)) and spherical particles (Fig. 5.21(a)) were assessed from X-ray diffraction data. According to Eq. 5.1, it was necessary to have exact values of lattice parameters and compressibility. Values for the latter were taken from Haines study [114]. For precise peaks characteristics, diffractograms were refined in *Topas* software package and then processed with the use of Nelson-Riley function (see section 3.1.5) for exact values of lattice parameters a and c.

Deviation of the lattice parameters from those reported for the bulk crystals [115](see

Appendix D) amounted to $\Delta a_{spheres} = 1.558 \times 10^{-1}$ Å and $\Delta c_{spheres} = 1.284 \times 10^{-1}$ Å, and $\Delta a_{platelets} = 8 \times 10^{-4}$ Å and $\Delta c_{platelets} = 4.39 \times 10^{-2}$ Å. The above data and intermediate calculations summarized in Tables 5.13 and 5.14, yielded the surface tensions.

Table 5.13: Evaluation of lattice parameters of spherical and platelet MgF_2 nanocrystals

d	2θ	h k l	Intercept—precise values of lattice parameters			
			$cos^2\theta$		$\frac{cos^2\theta}{sin\theta} + \frac{cos^2\theta}{\theta}$	
			a, Å	c, Å	a, Å	c, Å
2.52911	35.534	101	Spherical particles			
2.22779	40.489	111	4.7433	2.9653	4.5875	3.0937
2.03317	43.216	210				
1.72042	53.251	211	Platelet particles			
1.65085	55.664	220				
1.51676	61.04	002	4.6625	3.001	4.6288	3.0889
1.38427	67.62	122				

In Table 5.13 the list of analyzed peaks was acquired from XRD patterns of both samples. Resolved by two approximation methods (Figs. 5.29 and 5.30), precise lattice parameters were then used to calculate the surface tension of spherical and platelet particles.

It is interesting to note the correlation between the two different MgF_2 crystal shapes and σ values (Table 5.14). In the case of spherical particles, the surface tensions of a and c lattice parameters are almost equal and high in absolute value, which indicates that particles are made of very small subunits of isotropic shapes. Indeed, quantitative data, obtained from XRD by the Scherrer method (see Sec. 5.2),

Table 5.14: The surface tension of MgF_2 particles of different shapes calculated with the values of parameters obtained from Nelson-Riley approximation and Eq. 5.1

	LP*	MgF_2 spheres	MgF_2 platelets
Sample		Table 4.4, D	Table 4.4, A
Micrograph		Fig. 5.21(a)	Fig. 5.18(a)
XRD		Fig. 5.21(b)	Fig. 5.18(b)
Lattice parameters for bulk crystal [115], Å	a	4.6280	
	c	3.0450	
Lattice parameters, obtained from experiment by Nelson-Riley approximation, Å	a	4.5875	4.6288
	c	3.0937	3.0889
Compressibility [114], GPa^{-1}	a	0.003	
	c	0.0024	
Absolute values of surface tension, N/m	a	3.89	0.02
	c	4.01	1.37

*Lattice parameter

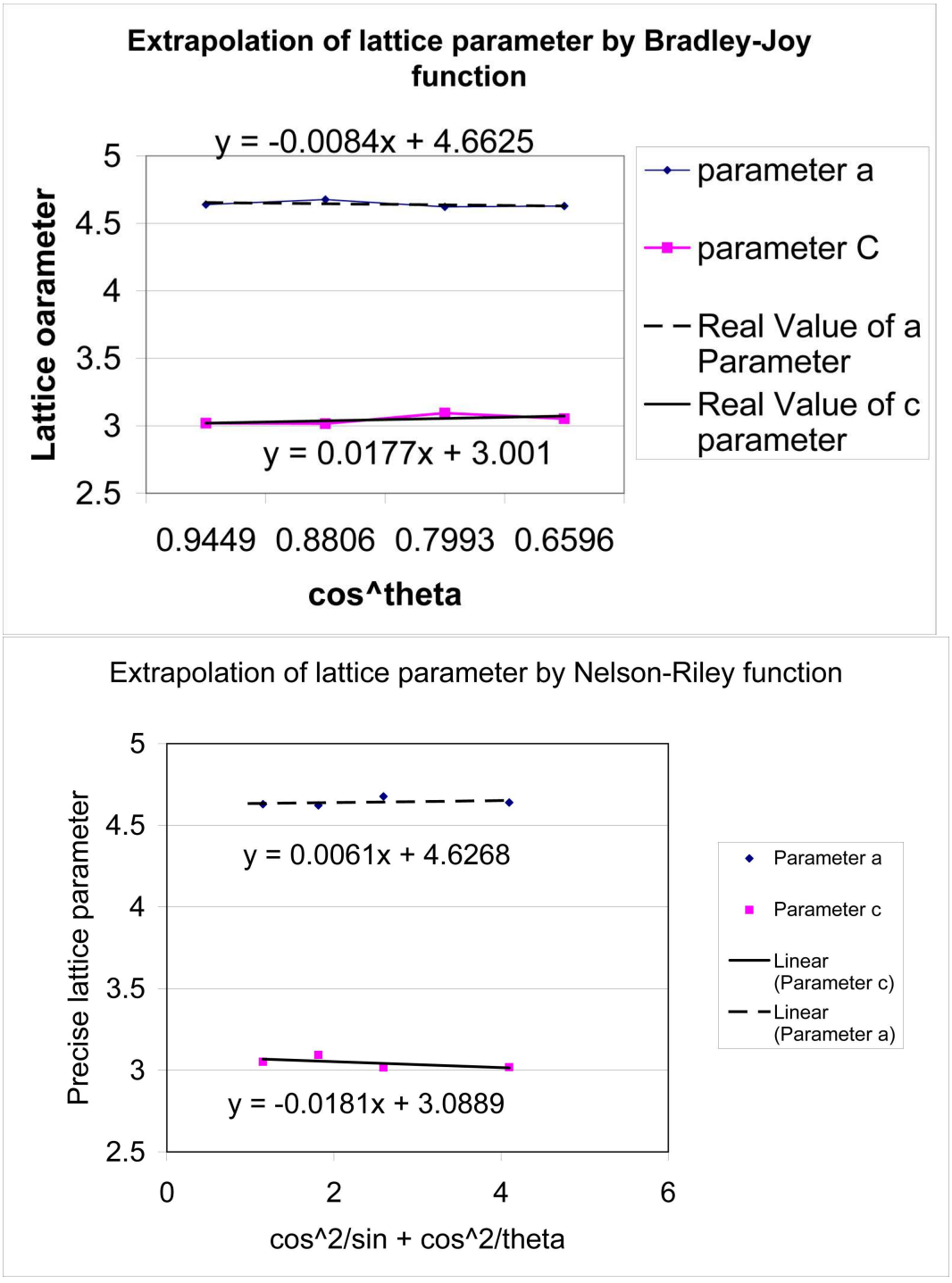

Figure 5.29: Bradley-Joy and Nelson-Riley approximations for MgF_2 platelet crystals

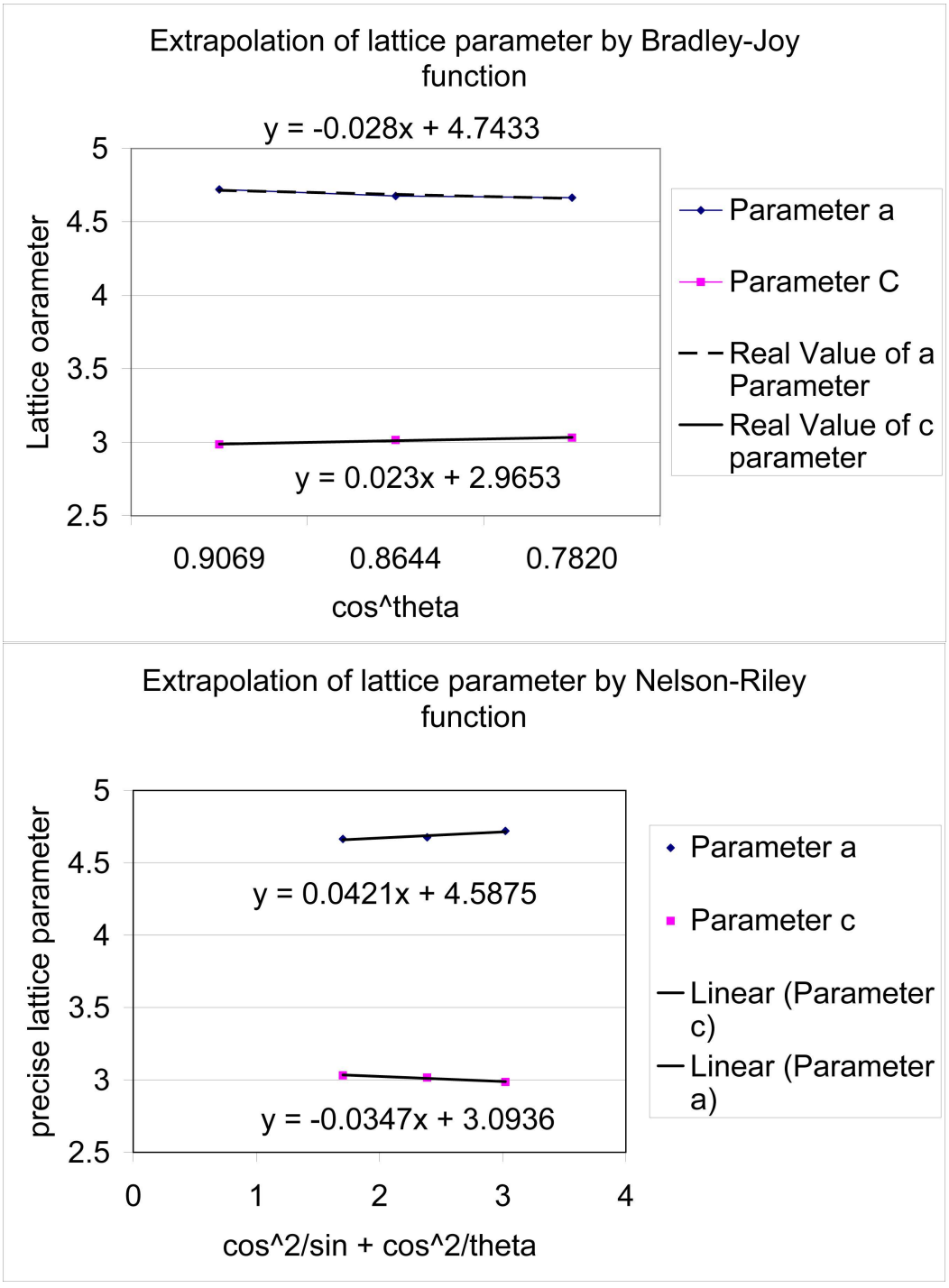

Figure 5.30: Bradley-Joy and Nelson-Riley approximations for MgF_2 spherical crystals

shows that spheres are made of nanosize subunits of 8–15 nm in size [66].

In case of platelets, the interpretation of the surface tension data is more complex. From the micrographs it follows that the particles have hexagonal structure with (111) surface, which means that there was very limited growth in Z-direction (perpendicular to (111) plane), and almost unrestrained growth in the XY-plane. Such selective growth may be explained by the preferential adsorption of the OH^- groups on (111) planes, when MgF_2 particles were formed in basic solutions. Electron diffraction and powder X-ray diffraction (5.18b) did not detect hydroxy compounds, such as $Mg(OH)_2$, Mg(OH)F, Mg(OH)Cl. EDX, however, detected some oxygen present in all samples (Fig. 5.18(c)), which is an indicative of the OH^- group.

Due to the platelets geometry two significantly different numbers of surface tension were obtained. As listed in the Table 5.14 value of a is close to zero, representing low stress in the XY-plane. In contrast, value of c is a big number, indicating high interatomic forces along Z-direction. From the physical point of view, it means that immediately after nucleation OH^- anions bound to the (111) planes on the nuclei surface and prevented particles from further growth in this direction, which caused their thickness of $\sim$20 nm.

Clearly, the surface tension value continuously alters during particles growth. The general trend of such change is expected to decrease when particles grow, which, ideally, should be accounted in the dynamic numerical models. The method described here, allows to calculate the surface tension, and may help in the future numerical simulations that attempt to characterize growth of the particles of different morphologies. For example, in [72] Robb *et. al.* discuss results of computational modeling of the formation of uniform spherical silver particles. For their calculations the authors used surface tension as a fitting parameter, assuming values between 0.4–0.55 N/m. However, the surface tension value, calculated as described here, results in 0.02–0.05 N/m

for the same silver particles, which is at least one order of magnitude lower. It is understandable that Robb's study was extended to a certain approximation; however, it is advisable in the future to utilize experimental data since it can be obtained fairly easily.

Chapter 6

Conclusions

This study illustrated the complexity of the problems related to the preparation, in a predictable way, of uniform particles of a given chemical composition and shape by the precipitation process. Using a system of a relatively simple chemical composition and avoiding complexation of interacting ions, it was possible to produce uniform particles of different shapes and internal structures by changing only a few parameters (pH, temperature, reactant concentration, and ionic strength). Specifically, cubic, prismatic, platelet, and spherical colloidal particles of PbS, MgF_2, and $NaMgF_3$ were formed either by diffusional growth or aggregation of the subunits as classified at the bottom of the Scheme 1.1.

The problem with the predictability of final shapes of particles, prepared by precipitation in solutions, becomes even more difficult once the reacting species form various complexes prior to precipitation. It would seem that in the present state of our understanding of precipitation processes, the formation of homogeneous spheres is expected when reacting cations hydrolyze and form polymeric solutes which then condense. In contrast, the formation mechanisms of monocrystalline and polycrystalline particles require information on all species in reacting solutions and their interactions,

which differ from case to case. Obviously, under such conditions the predictability of the properties of the resulting well-defined solids becomes a rather difficult, if not impossible, task. Rather than being able to predict the formation of a specific dispersions, it is possible to elucidate the formation mechanisms when all pertinent data become available.

Chapter 7

Novel Method for Characterization of Spherical Colloidal Particles

7.1 Distribution of density in spherical colloidal particles by TEM

Introduction

The variation in the distribution of density in colloidal spherical particles was evaluated by transmission electron microscopy (TEM) [116], without utilizing a high resolution mode, and quantified by image processing. The method eliminates the dependency of the image contrast on sample crystallinity. The advantage of such an approach is manifested by the short time sample preparation, fast instrument tune-up, rapid image acquisition and analysis, all of which shortens the processing time. Colloid silver spheres and gold nanoparticles were examined and compared to amorphous silica and acrylate-methacrylate polymer spheres. The latter can be considered as ideal homogeneous model samples. Image files having **.dm3* extension, obtained

from TEM, were processed with *ImageJ* software, and later analyzed with script written in *Microsoft Visual C++*. It is shown that the radial distribution of density of highly crystalline gold nanoparticles resembles the used models, while in larger polycrystalline silver spheres it differs significantly from the "ideal" case. Deviations from linearity for gold and silver were interpreted in terms of finite polydispersity and internal inhomogeneities. The described method made it possible to estimate rapidly the number of subunits needed to achieve properties of an equivalent sphere, without considering the crystalline nature of such particles.

It is well known that many properties of finely dispersed matter (optical, magnetic, adsorptive, etc.) depend not only on chemical composition, but also on the size, shape, and internal structure of individual particles. It is important in many applications for solids to consist of entities as uniform as possible. While many methods are available for the preparation of well-defined nanometer to micrometer size particles of different morphologies [6–8], their size distribution may vary somewhat, as well as the internal structure or some other properties. For example, the internal density of spheres may change from the center to the periphery, which could affect their optical, electrical, and thermomechanical characteristics. Therefore, it is desirable to have methods to quantify such properties within individual particles, without resorting to complicated techniques, such as high resolution TEM.

Below an analytical procedure is described that allows to evaluate density variation due to internal inhomogeneity and particle size by a TEM technique. Multiple radial distributions of density of each individual metallic sphere (silver and gold) were constructed and compared to those, obtained for internally homogeneous spheres of silica and the polymer. The method is based on the relationship [94]:

$$log(I_0/I(r)) = \mu\rho x \tag{7.1}$$

where I_0 and $I(r)$ are the incident and transmitted beam intensity, respectively, μ is a quantity that involves experimental parameters, such as objective aperture and exposure conditions, ρ is the material density, and x is the thickness of the sample. The plot of $log(I_0/I(r))$ as a function of x for an ideal sphere should give a straight line. Indeed, the studied model systems produced such a linear relationship, while deviations from linearity for gold and silver particles could be interpreted in terms of finite polydispersity and internal inhomogeneities. Thus, the method yields not only the bulk density data, but also qualitative indications on some physical properties of the dispersed matter.

Materials

Silica particles were chosen due to their near perfect sphericity and optimum contrast gradient when using bright field TEM (BFTEM). A dispersion of such particles, which were prepared by hydrolysis of tetraethyl-orthosilicate (TEOS) as originally described by St*ö*ber [117] is illustrated in Fig. 7.1a [90]. Two such particles of ∼200 nm were evaluated in the analysis (Fig. 7.1b). The application of the model to larger spherical particles of lower specific gravity was verified with acrylate-methacrylate polymers of $\sim 3\mu m$ in diameter (Fig. 7.2) supplied by CONPART (Oslo, Norway). The uniform gold nanoparticles (Fig. 7.3) were obtained by chemical precipitation in homogeneous solution to be described elsewhere. Polycrystalline spherical silver particles (Fig. 7.4), consisting of nanosize subunits were prepared by reduction of a silver-polyamine complex with iso-ascorbic acid as reported in [118]. Essential properties of the materials are summarized in Table 7.1.

Table 7.1: Physical properties of particles

Material	Specific gravity, $kgm^{-3}10^3$	Size, nm
Gold	19.3 [106]	∼20
Silver	10.5 [119]	50–100
Silica	2.2 [119]	∼200
Acrylate-methacrylate	1.08 [119]	∼3000

Characterization methods

For the TEM measurements samples were prepared accordingly to the section 3.2. Digital images, obtained from TEM with the Digital Micrograph software (GATAN INC.), were saved in *.dm3 format, which allowed them to store the relevant information needed in this study, such as exposure conditions, the incident and transmitted electron beam intensities, as well as the size of the pixels in units of length (e.g. nanometers) .

Data processing and interpretation

Digital images, acquired in bright field TEM mode, were evaluated using the *ImageJ* (image processing software [120, 121]) as follows: a straight line was drawn from the approximate center of a particle towards the periphery (Fig. 7.5, single line). To avoid artifacts caused by angular variations of the intensities, a moderate thickness line was selected. To eliminate fringes and other diffraction effects that may arise due to high magnification and crystallinity of the samples, each particle was virtually sliced into 36 segments, which were then averaged. Thus, a radial profile script, using Microsoft Visual C++ programming language, was implemented in the image processing software in order to perform the following tasks:

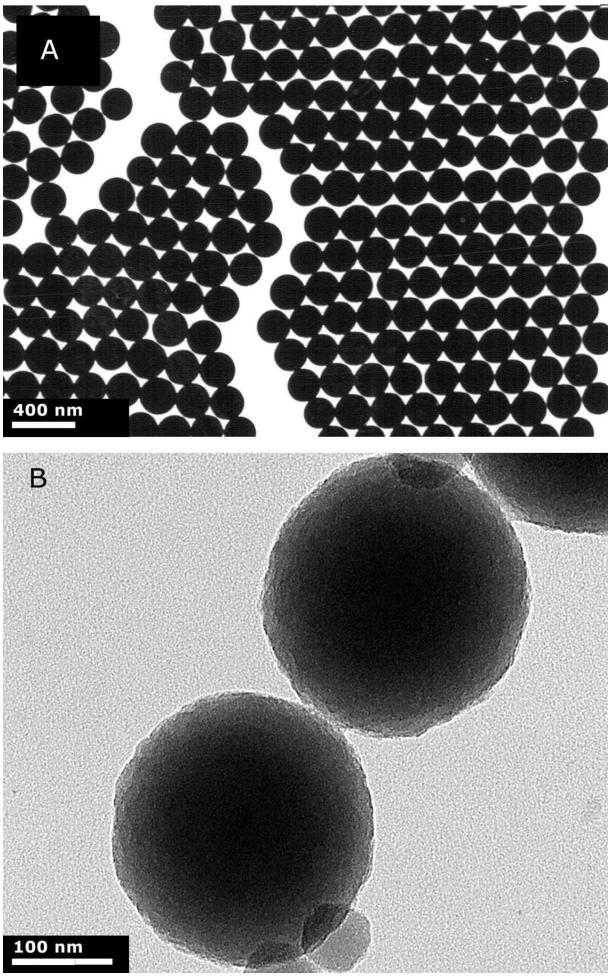

Figure 7.1: (a) Example of a dispersion of silica particles prepared by hydrolysis of TEOS [90, 117]; (b) TEM of two silica particles used in this study

- identifying the background intensity that corresponds to I_0 in Eq.7.1;
- dividing a particle into 36 equal angular segments (Fig. 7.5 multiple lines);
- finding the particle's boundaries inside the built circumference, defining the average radius of the particle, normalizing it to unity, and finding new geometrical center;
- constructing the intensity profile $I(r)$ along each line (Fig. 7.6);
- calculating and storing of these values in data file ($*.dat$).

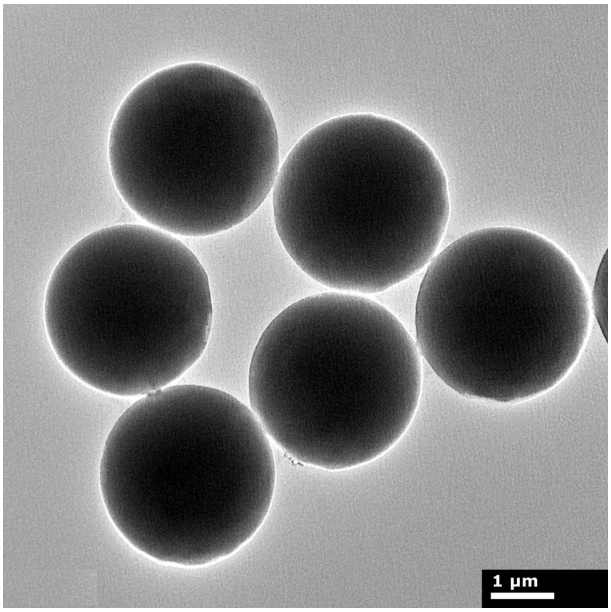

Figure 7.2: TEM of acrylate-methacrylate polymer particles were used to test the model

Information gathered with this script was arranged as follows: the lengths of the angular segments were stored in 36 columns, while the number of pixels along each radius was stored in rows (approximately 380–500 rows, depending on the image magnification). The so obtained two-dimensional array was further statistically analyzed with a Microsoft Visual C++ script by averaging all 36 columns for each row and fitting data to a linear function, as examplified for silica particles in Fig. 7.7.

Results

Since this study is mainly focused on the interpretation of digital images obtained by electron microscopy, taking advantage of the instrument output, the format was essential. Commonly, in imaging analytical techniques each pixel in an image is assigned to a measured intensity and the data are saved in various formats (e.g. *jpg, tiff, bmp,* etc.). In most cases converted data lose some essential information because each pixel represents color values rather than absolute values of original intensity.

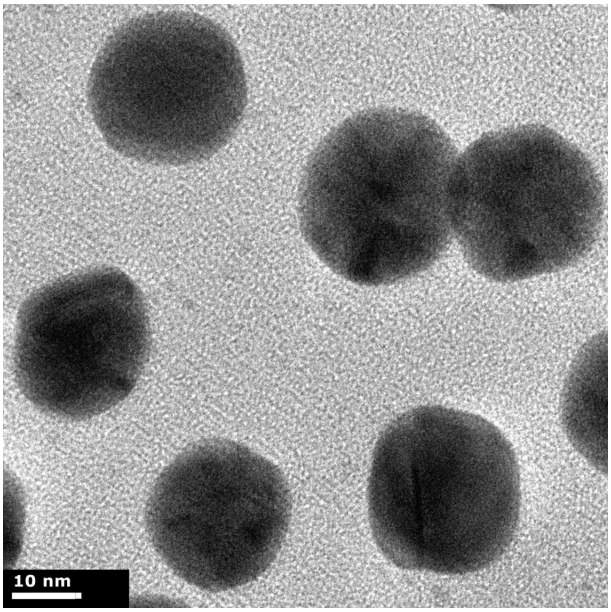

Figure 7.3: TEM of gold particles prepared by chemical precipitation in homogeneous solution

For example, in a grayscale picture zero and 255 correspond to black and white pixels, respectively. Such conversion to grayscale maintains the general visual details and provides small file size, but lacks the ability to store specific details that might be needed for more advanced processing. For the purpose of this study the **.dm3* format was used (Fig. 7.6), because it stores pertinent information and eliminates the deficiency of a grayscale.

TEM images (Figs. 7.3, 7.4) show that the investigated metal particles are not perfect spheres, but for processing purposes they were treated as such, with equivalent radii as described in the radial profile script. The essential approximation, made in the script, considers 36 different radii (profiles) of a given particle from the manually selected center to its edge with 10 degree increments (Fig. 7.5, multiple lines). Further, based on the calculated average radius, the script defines a confined circle and redefines the geometrical center of the particle. All further processing and interpretations are performed over the particle circumference generated in the last step. Using

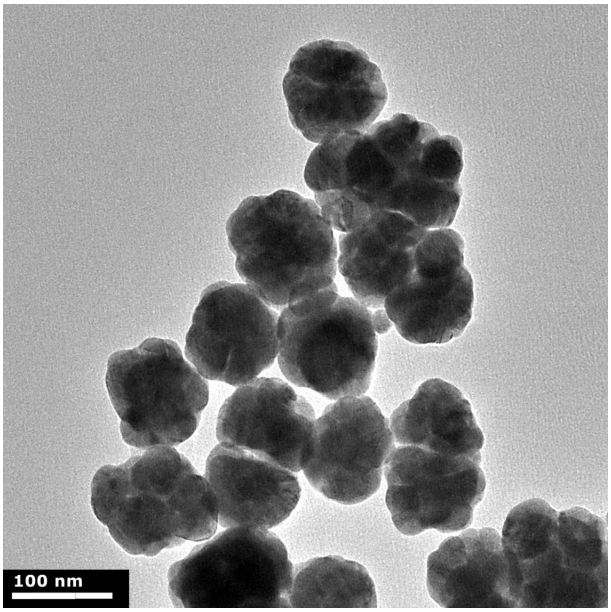

Figure 7.4: TEM of silver particles prepared by reduction of silver-polyamine complex with iso-ascorbic acid according to [118]

the described procedure, it was possible to obtain an appropriate contrast gradient of the systems summarized in Table I using apertureless BFTEM mode.

The reference spherical silica and polymer particles showed gradual increase in transparency from the center to the periphery, while the transparency remained constant upon rotation with respect to the center of symmetry. It is essential to recognize that even these "ideal" particles may have some minor surface roughness.

The profiles of bulk density of two individual silica particles (Fig. 7.7) follow the straight line as predicted by Eq. 7.1 for the sphere. Analogous results were obtained for the spherical acrylate-methacrylate particles as displayed in Fig. 7.8.

Gold investigated under BFTEM mode shows similar trends (Fig. 7.9) as the model systems. While the individual density profile of each sphere deviates slightly from linearity, the calculations show that the linearity improves, if one builds a stack of five individual entities (Fig. 7.10). This finding yields the same kind of density profile as for "ideal" silica particles.

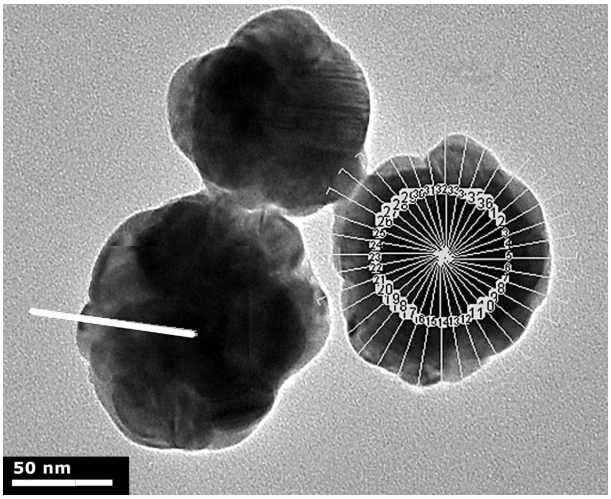

Figure 7.5: Spheroidal silver particles, analyzed in ImageJ, with initial radial profile line of interest (single line on the left particle) and 36 angular segments (multiple lines on the right particle)

In contrast, the same analysis, applied to the silver, shows considerably greater deviation (Fig. 7.11) in linearity than the other investigated cases. Furthermore, stacking of several silver particles lessens the profile deviation, but still does not produce reasonable linearity (Fig. 7.12).

Discussion

The results of the described analytical method are applicable to particles of any shape, but the program developed in this study can be applied only to spheroids. In principle, obtained data are affected by the size and uniformity of the particles, their density, and internal structure. The results of the analysis are expressed in plots as log of intensity ratios vs. normalized particle's thickness, which in an ideal case should be linear as required by Eq. 7.1. In real systems the shapes of these plots can be used to qualitatively assess certain particle properties in a given dispersion.

Monodisperse spheres (silica and acrylate-methacrylate) of somewhat different sizes yielded quite linear plots of the same slope with relatively small vertical shifts,

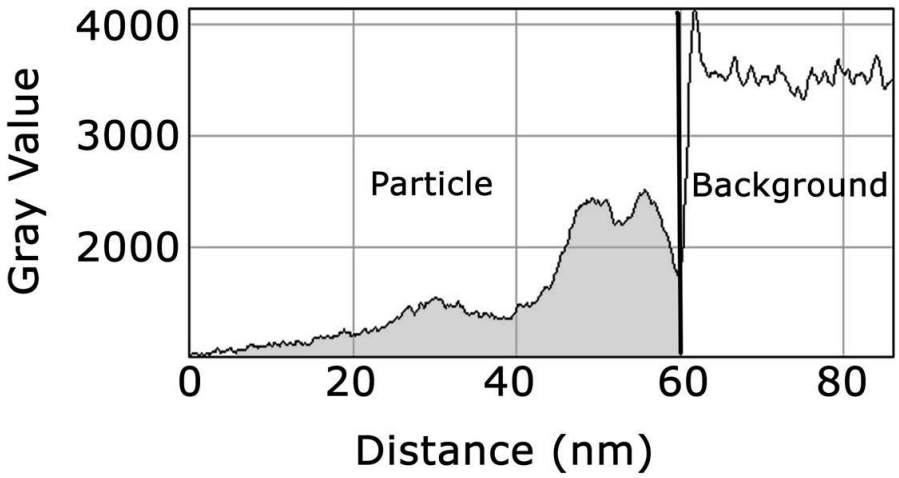

Figure 7.6: Typical intensity profile from **.dm3* file along straight line taken from the center of a particle to beyond its boundaries

indicating their size uniformity (Figs. 7.7, 7.8). The magnitude of such shifts is indicative of their degree of polydispersity. Departure from the linearity depends on internal inhomogeneity of the particles, caused either by crystal planes at high resolution, or their composite nature, for example, when they are made up of smaller subunits. In the case of gold (Fig. 7.9) there is some deviation from linearity and more pronounced vertical shifts. While these particles are single crystals, the observed trends are partially due to some distortion of sphericity and to internal crystal planes. Averaging data for five particles (Fig. 7.10) eliminates the structural and morphological effects.

In contrast, much larger silver particles show significant departure from the ideal case. It has been established that the experimental procedure [118] yields particles that consist of aggregates of smaller subunits. Such internal structure should be responsible for the observed analytical results. Averaging data for five particles (Fig. 7.12 plot B), similarly to gold, eliminates both internal effects and shape deviations from the ideal model. However, it is insufficient to use only three particles in order to obtain density profile for the entire silver dispersion (Fig. 7.12 plot A).

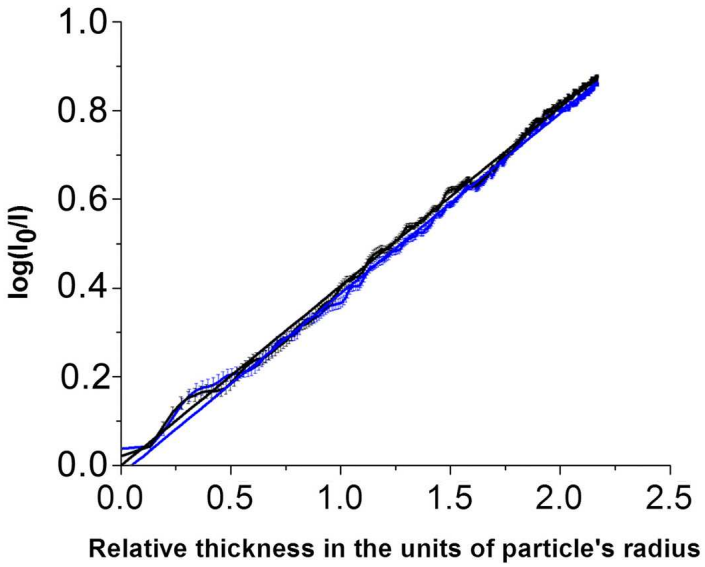

Figure 7.7: The plot of data for silica particles density profile according to Eq. 7.1, with small oscillations near its average. Two curves represent two particles from Fig. 7.1b

A final comment refers to reproducible deviation from the linearity in density profile plot of silica particles between abscissa values of 0.25 and 0.5 (Fig. 7.7). The latter corresponds to distances of 0.96 R and 0.98 R from a particle's center, where R is the averaged and normalized to unity radius of a spheroidal particle. Such deviation can be caused by Fresnel diffraction at the edge of a sphere with high curvature. Fok [122] described the theoretical possibility of this phenomenon for spherical objects that have a radius much larger than the wavelength of the incident radiation. Analogues effect was not observed with the investigated metallic particles, because it was obscured by stronger deviation from linearity of their density profiles.

In principle, the density profile in a given particle can also be obtained by X-ray elemental mapping in the STEM mode. However, as shown in Fig. 7.13, this technique was unable to provide accurate results, due to poor resolution and high scattering blurriness in the images.

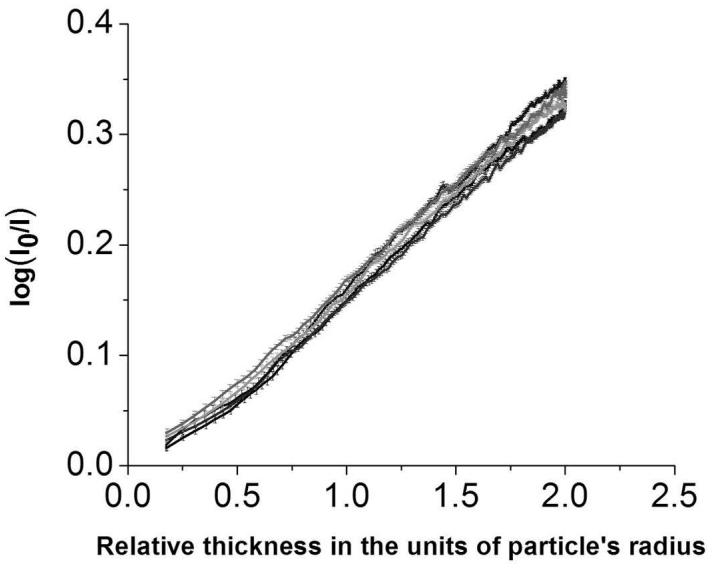

Figure 7.8: The density profile plot data for five acrylate-methacrylate particles from Fig. 7.2

Conclusions

This section describes a model that can yield bulk density changes of individual spherical either amorphous or crystalline particles of different sizes and internal compositions from regular TEM images. The image processing does not discriminate particles based on their crystallinity. Thus, two amorphous spherical particles (organic acrylate-methacrylate and inorganic silica) yielded linear profile of bulk density from their center to periphery. In contrast, spherical particles of two metals (silver and gold) showed significant deviations of their density profiles due to shape and internal structure factors. However, assuming layers of several particles the density profile approaches the predicted linearity. This particular consequence may be important for applications, where film thickness properties are critical. By applying the described method one may assess the particle packing in the deposition of thin layers in microelectronics and sensors. Results with silver are of additional interest, because it has been well established that a large number (if not most) of uniform colloidal

particles, prepared be precipitation, consist of smaller subunits [123]. Indeed, a model was developed that defines conditions under which monodispersed spheres can form by such aggregation mechanism [12, 54, 56].

In addition, current model may be utilized for evaluating the thickness of coating of spherical particles. Indeed, densities of a particle and its coating are different and, thus, should give a vertical shift between their linear trends. Obviously, the number of *coating* atoms will be larger at the edge of the TEM projection of the spherical particle comparatively its center. Hence, two profiles should start with significant displacement and then one – that is correspondent to the coating – should smoothly merge into the particle's profile.

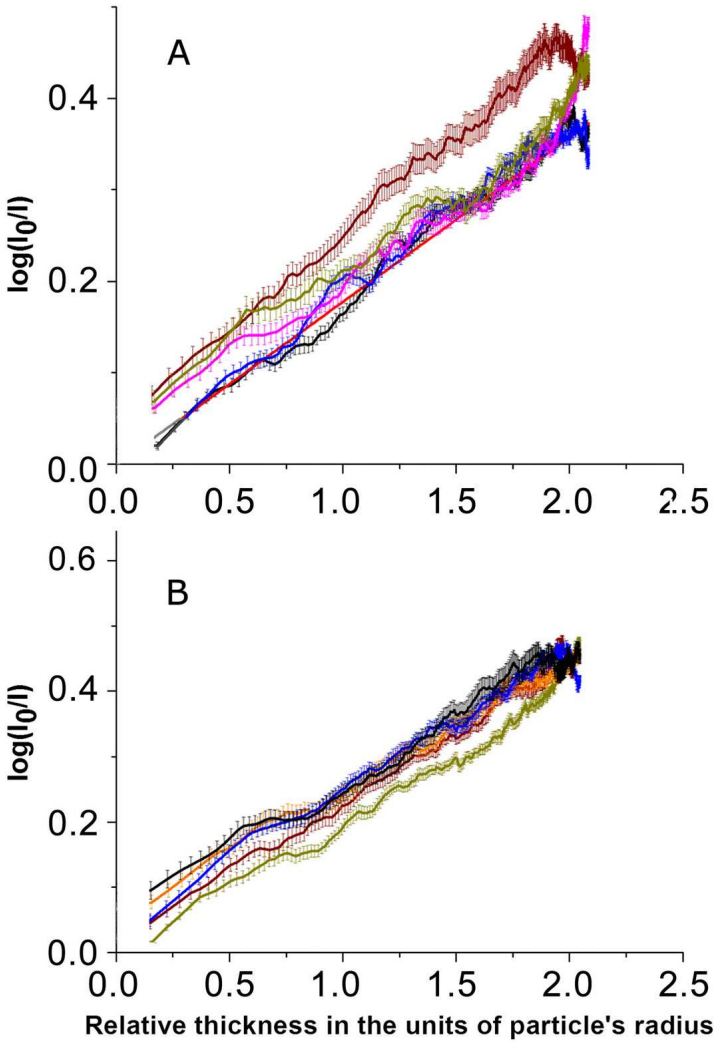

Figure 7.9: (a) A batch of five gold particles and (b) data from another batch of five particles

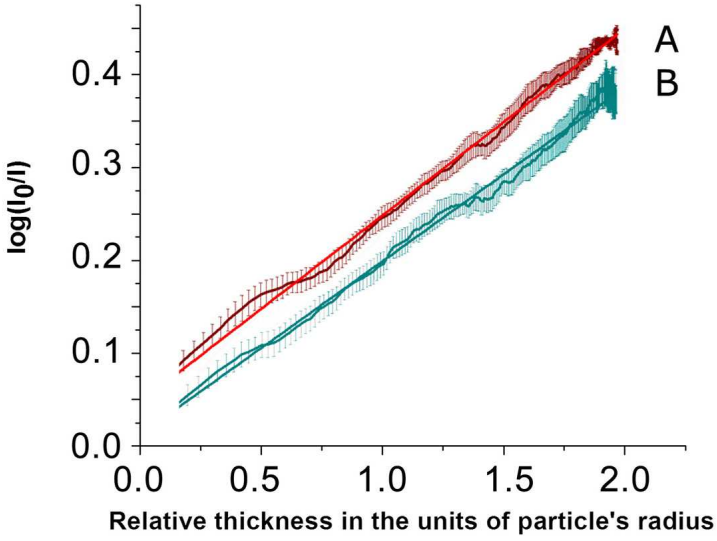

Figure 7.10: Averaging of five gold particles from Fig. 7.9a and Fig. 7.9b

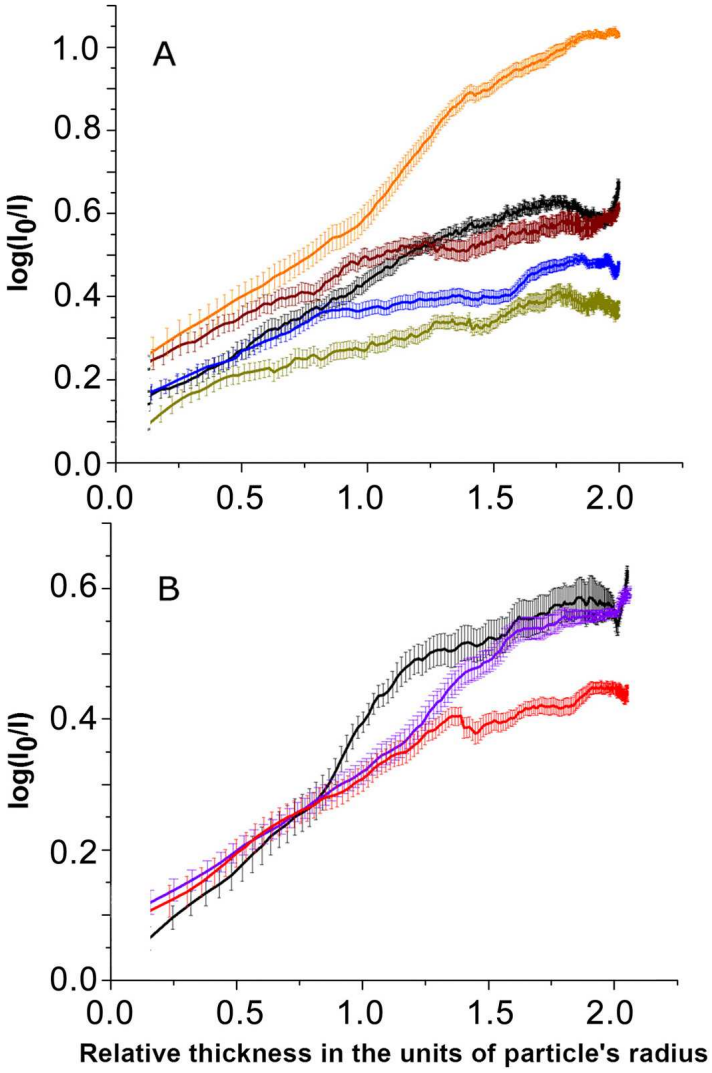

Figure 7.11: (a) A batch of five silver particles and (b) data from another batch of three particles

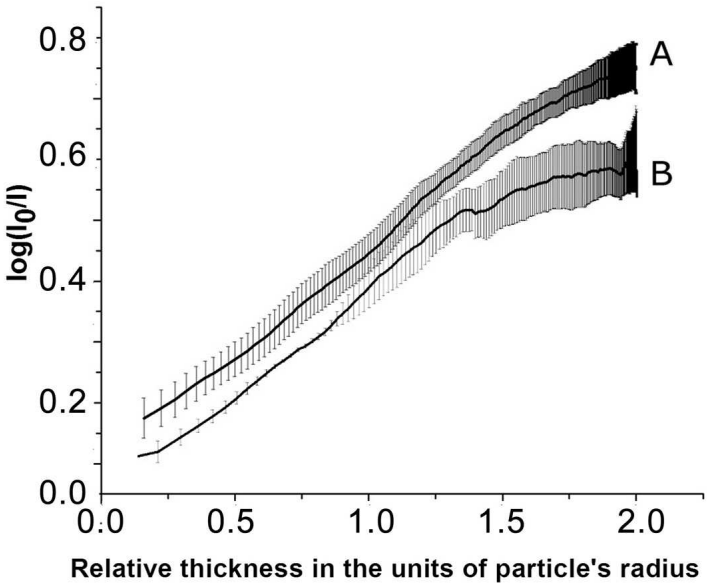

Figure 7.12: Averaging of five particles from Fig. 7.11a and three particles from Fig. 7.11b

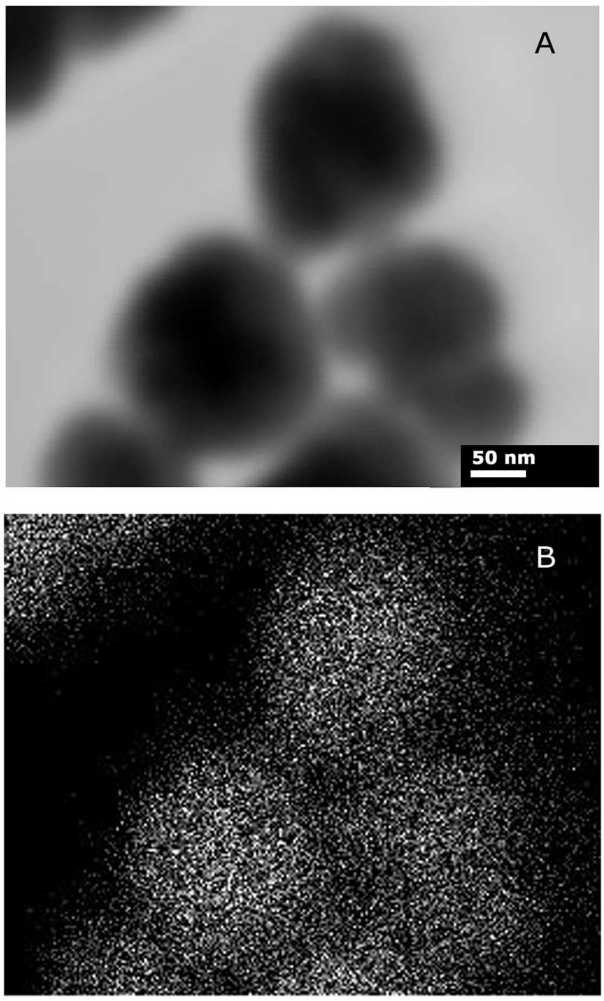

Figure 7.13: (a) STEM mode of nanosize silver particles of the same sample as in Fig. 7.4 and (b) is their mapping equivalent

Appendix A

3D Numerical Simulation Code

```
// surface model v8.cpp : the program simulates three dimentional growth of a particle

#include "stdafx.h"
#include <iostream>
#include <stdio.h>
#include <stdlib.h>
#include <math.h>
#include <iomanip>
#include <time.h>
#include <dos.h>
#include <fstream>
#include <conio.h>
#include <string>
using namespace std;

#define Time 40000000       // this is the number of the deposited particles
#define GTime 5             // this is the number of iterations for averaging the global height
#define Period 1000

#define Pi 3.14159265
#define mean1   45
#define mean2   135
#define mean3   225
#define mean4   315
#define mean_up 54.7356  // corresponds to 0.9553 this and below are angles between random line and 0Z axis
#define mean_dn 125.2644
#define epsilon 0.0001
#define wangle  0.7853  // some angle in Rad that defines gaussian in range -+ wangle

const int LEN = 28;         // this is the length of the INITIAL particle
const int WID = 28;         // this is the  width of the INITIAL particle
const int HGH = 28;         // this is the height of the INITIAL particle
const int M = 700;              // this is the  width of the space
const int L = 700;              // this is the length of the space
const int N = 700;              // this is the height of the space

    int iarr_space[L][M][N];
    /* an array of the space -- stores all data about the events */
//  short arr[300];
```

```
    inline short zero_data(int iarr_space[L][M][N]);
    /* makes the iarr_space array ZERO */

    short deposition(int iarr_space[L][M][N], float angle1, float angle2);
    // this function corresponds to particles deposition

    short rearrangement(int iarr_space[L][M][N]);
    // analogically -- this is rearrangement of already deposited particels

int   x1, x2, y_1, y_2, z1, z2;   /* some global variables */
double fx1, fx2, fy1, fy2, f_0 , sig, ratio;

int main()      /*AAAAAAAAAAAAAAAAAA  MAIN  AAAAAAAAAAAAAAAAAA*/
{
/*================================*/
    char start[10], end[10]; /* it's just for getting time from processor*/
    srand((unsigned)time(NULL));
/*================================*/

/*================================*/
    short   s_temp, s_choice_dr/* deposit or re-arrange*/, s_choice_sp/* part of the space*/, region;
    short   x_coord, y_coord;
    int     i; /* counters  */
    int     i_temp; /* variables */
    float   f_temp_rand, _ro , _phi, _psi, _gam, norm, u1, u2, v1, v2, f_y ;
/*================================*/

    /*================================*/
        ofstream surf("surface_data.dat", ios::trunc/*ate*/);/* here we creat files to fill them later*/
        ofstream surf_x("x_data.dat", ios::trunc/*ate*/);/* here we creat files to fill them later*/
        ofstream surf_y("y_data.dat", ios::trunc/*ate*/);/* here we creat files to fill them later*/
        ofstream surf_z("z_data.dat", ios::trunc/*ate*/);/* here we creat files to fill them later*/
        ofstream temp_d("temp.dat", ios::trunc/*ate*/);/* here we creat files to fill them later*/

        surf<<_strtime(start)<< endl << _strtime(start) << endl;
        cout<<_strtime(start)<< endl;
        cout<< "size "<<(int) sizeof(iarr_space)<<endl; /* memory size check */
/*================================*/
    x1 = L / 2 - LEN / 2;   x2 = L / 2 + LEN / 2 ;
    y_1 = M / 2 - WID / 2;  y_2 = M / 2 + WID / 2;
    z1 = N / 2 - HGH / 2;   z2 = N / 2 + HGH / 2 ;
    zero_data(iarr_space);
    cout << "\a";
    cout << "Input standart diviation 'sigma' = ";
    cin >> sig ; surf << "Input standart diviation 'sigma' = " << sig << endl;
    cout << "Input ratio between deposition and rearrangement r = "; cin >> ratio ;
    surf << "Input ratio between deposition and rearrangement r = " << ratio << endl;

    ofstream temp_data("temp.dat", ios::ate);/* here we creat files to fill them later*/

/* total number of particles which already deposited */
for (i = 0; i < Time; i++){
    if ((i % 1000) == 0){ cout << i << "   "<<_strtime(start)<<endl; }
/* This is the loop which describes evolution for only one particle*/

    /* shows how many loops is already done */
    /* in the following lines we decide : deposit or rearrange particles */

    s_temp = rand(); f_temp_rand = (float)s_temp / 32768 ;
    s_choice_dr = (f_temp_rand < ratio)  ? 0 : 1;
        /* with the probabily 1/ratio it will be the deposition */
    switch(s_choice_dr){
        case 0:                     /* D E P O S I T I O N */
                do{
                    do{
```

```
                s_temp = rand(); u1 = (double)s_temp / 32767 ;
                /* METHOD OF THE POLAR SYSTEM COORDINATES WHICH DEFINES PHI_angle */
                s_temp = rand(); u2 = (double)s_temp / 32767 ;
                v1 = (2 * u1 - 1); v2 = (2 * u2 - 1); f_y = pow(v2,2) + pow(v1,2);
                }
                while(f_y >= 1);
                _phi =(float)sig * v1 * sqrt(-2 * log(f_y) / f_y);
                         /* normaly distributed angle with diviation 'sig' & mean value 'f_mean' */
                         // infact!! this is normal distribution!!
                }   while ((_phi > 0.7854) || ( _phi < -0.7854 )); /* corresponds to +-45 degree in RAD
                                                                     this value and below psi can be arbitrary
                                                                     because model by itself is not physical */

                do{
                    do{
                s_temp = rand(); u1 = (double)s_temp / 32767 ;
                   /* METHOD OF THE POLAR SYSTEM COORDINATES WHICH DEFINES PSI_angle */
                s_temp = rand(); u2 = (double)s_temp / 32767 ;
                    /* this routin is described in Knuth Art of Programming v2 1981*/
                v1 = (2 * u1 - 1); v2 = (2 * u2 - 1); f_y = pow(v2,2) + pow(v1,2);
                }
                while(f_y >= 1);
                _psi =(float)sig * v1 * sqrt(-2 * log(f_y) / f_y);
                        /* normaly didtributed angle with diviation 'sig' & mean value 'f_mean' */
                }   while ((_psi > 0.7854) || (_psi < -0.7854));
                        /* corresponds to +-45 degree in RAD*/

            s_temp = rand(); f_temp_rand = (int)s_temp * 4 /32768;
                 // phi value runs through 4 upper corners of a cube when psi is mean_UP
            _phi = _phi + (f_temp_rand * Pi/ 2 + Pi / 4) ;
                // and throuhg 4 lower corners when psi is mean_DOWN

            s_temp = rand();
            if(( s_temp % 2 ) == 0 ) {
                _psi = _psi + (float)mean_up * Pi / 180;}
            else {
                _psi = _psi + (float)mean_dn * Pi / 180;}

                deposition(iarr_space, _phi, _psi); // deposited particles

        break;
        case 1:                     /* R E - A R R A N G E M E N T */

                    rearrangement(iarr_space);

        break;
    } /* end of     switch(s_choice_dr){ */

}     /* end of     for (num_particles = 0; num_particles < Time; num_particles ++) */

          for (int ii = 0 ; ii < L; ii++){
             for (int jj = 0 ; jj < M; jj++){
                 for(int kk = 0 ; kk < N ; kk++){
                     if ((iarr_space[ii][jj][kk] == 1))
                     {surf_x << ii<< endl; surf_y << jj << endl; surf_z << kk << endl;}
                 }
             }
        }

        surf<<_strtime(end)<< endl;
        cout << "\a";
    return 0;
}

/* AAAAAAAAAAAAAAAAAAA  FUNCTIONS AAAAAAAAAAAAAAAAAA */
```

```
/*AAAAAAAAAAAAAAAAAAAAAAAAAAAAAAAAAAAAAAAAAAAAAa*/
// Space is Initialized here
inline short zero_data(int iarr_space[L][M][N]){
    short ii, jj, kk;
        ofstream surf("surface_data.dat",ios::ate);
        ofstream surf_x("x_data.dat", ios::ate);
        ofstream surf_y("y_data.dat", ios::ate);
        ofstream surf_z("z_data.dat", ios::ate);

        for(ii=0; ii<L; ii++){
            for (jj=0; jj<M; jj++){
                for (kk = 0; kk < N; kk++){
                iarr_space[ii][jj][kk] = 0;
                }
            }
        }
        for(ii = x1; ii <= x2; ii++){   /* we set the shape of the surface */
            for (jj = y_1; jj <= y_2; jj++){
                for(kk = z1; kk <= z2; kk++){
                    iarr_space[ii][jj][kk] = 1;
                }
            }
        }
        for(ii = (x1 + 1); ii < x2; ii++){
 /* this partition of the code hepls me in future create the carcas for the inital shape visualization */
            for (jj = (y_1 + 1); jj < y_2; jj++){
                for(kk = (z1 + 1); kk < z2; kk++){
                    iarr_space[ii][jj][kk] = 2;
                }
            }
        }
return iarr_space[L][M][N];
}
/*AAAAAAAAAAAAAAAAAAAAAAAAAAAAAAAAAAAAAAAAAAAAAa*/
/* D E P O S I T I O N */
/*AAAAAAAAAAAAAAAAAAAAAAAAAAAAAAAAAAAAAAAAAAAAAa*/
/* PLEASE BE AWARE OF THE FACT THAT HERE XX & YY ARE RELATIVE
COORDINATES WHILE IARR_SPACE DEALS WITH ABSOLUT VALUES */
short deposition(int iarr_space[L][M][N], float angle1,float angle2){
    short xx, yy, zz, ro;
    float f_ro, f_phi, d_psi, d_phi, d_gam, f_psi;

        ofstream surf_x("x_data.dat", ios::ate);
        ofstream surf_y("y_data.dat", ios::ate);
        ofstream surf_z("z_data.dat", ios::ate);
//      ofstream temp_data("temp.dat", ios::app);/* here we creat files to fill them later*/

    f_phi = angle1 ;
    f_psi = angle2 ;
    /*****************************/

        f_ro = LEN / 2 ; ro = (int)f_ro;
            xx = (int)ro * sin(-f_phi) * sin(-f_psi);  // Euler transformation for arbitrary axis
            yy = (int)ro * -sin(-f_psi) * cos(-f_phi);
            zz = (int)ro * cos(-f_psi);

            // here we check if CUBE's surface is reached to place new particle
        while(iarr_space[L / 2 + xx][M / 2 + yy][N / 2 + zz] != 0){
            ro++;
            d_phi = (float)rand()/32768 * 0.05235; /* noise introduced for the angle +-2 degree */
            d_phi = ((rand() % 2) == 0) ? -d_phi : d_phi;
            d_psi = (float)rand()/32768 * 0.0698; /* noise introduced for the angle +-4 degree */
            d_psi = ((rand() % 2) == 0) ? -d_psi : d_psi;

            xx = (int)ro * sin(-f_phi + d_phi) * sin(-f_psi + d_psi);
```

```
            yy = (int)ro * -sin(-f_psi + d_psi) * cos(-f_phi + d_phi);
            zz = (int)ro * cos(-f_psi + d_psi);

        }
        iarr_space[L / 2 + xx][M / 2 + yy][N / 2 + zz] = 1;

return iarr_space[L][M][N];
}
/*AAAAAAAAAAAAAAAAAAAAAAAAAAAAAAAAAAAAAAAAAAAAAAAAa*/
/* R E - A R R A N G E M E N T */
/*AAAAAAAAAAAAAAAAAAAAAAAAAAAAAAAAAAAAAAAAAAAAAAAAa*/
short rearrangement(int iarr_space[L][M][N]){
    short ii, jj, kk, xx, yy, zz, ro, s_check, xy_mean, z_mean, hold_x, hold_y, new_ro, hold_z, hold_ro;
    short keep_i, keep_j, keep_k;
    float f_ro, f_phi, d_psi, d_phi, f_psi, div, f_mean, fz_mean, f_rand ;

        ofstream surf_x("x_data.dat", ios::ate);
        ofstream surf_y("y_data.dat", ios::ate);
        ofstream surf_z("z_data.dat", ios::ate);
            /*  take particle from random spot */
        f_phi = (float)rand()/32768 * (2 * Pi + 0.01745); //0.01745 corresponds to ONE (1) degree
        f_psi = (float)rand()/32768 * (Pi + 0.01745) - Pi / 2;

        f_ro = (float)(pow((L*L + M*M + N*N),0.5)) / 5;
        ro = (int)f_ro;
        xx = (int)ro * cos(f_phi) * sin(f_psi);
        yy = (int)ro * sin(f_phi) * sin(f_psi);
        zz = (int)ro * cos(f_psi);

        while (iarr_space[L / 2 + xx][M / 2 + yy][N / 2 + zz] == 0){
                ro--;
            d_phi = (float)rand()/32768 * 0.05235; /* noise introduced for the angle +-2 degree */
            d_phi = ((rand() % 2) == 0) ? -d_phi : d_phi;
            d_psi = (float)rand()/32768 * 0.0698; /* noise introduced for the angle +-4 degree */
            d_psi = ((rand() % 2) == 0) ? -d_psi : d_psi;

            xx = (int)ro * cos(f_phi + d_phi) * sin(f_psi + d_psi);
            yy = (int)ro * sin(f_phi + d_phi) * sin(f_psi + d_psi);
            zz = (int)ro * cos(f_psi + d_psi);
        }
        iarr_space[L / 2 + xx][M / 2 + yy][N / 2 + zz] = 0;

        /* place particle randomly into another */
        f_phi = (float)rand()/32768 * (2 * Pi + 0.01745);
        f_psi = (float)rand()/32768 * (Pi + 0.01745) - Pi / 2;
        ro = 14;
        xx = (int)ro * cos(f_phi) * sin(f_psi);
        yy = (int)ro * sin(f_phi) * sin(f_psi);
        zz = (int)ro * cos(f_psi);

        while (iarr_space[L / 2 + xx][M / 2 + yy][N / 2 + zz] != 0){
                ro++;
            d_phi = (float)rand()/32768 * 0.05235; /* noise introduced for the angle +-2 degree */
            d_phi = ((rand() % 2) == 0) ? -d_phi : d_phi;
            d_psi = (float)rand()/32768 * 0.0698; /* noise introduced for the angle +-4 degree */
            d_psi = ((rand() % 2) == 0) ? -d_psi : d_psi;

            xx = (int)ro * cos(f_phi + d_phi) * sin(f_psi + d_psi);
            yy = (int)ro * sin(f_phi + d_phi) * sin(f_psi + d_psi);
            zz = (int)ro * cos(f_psi + d_psi);
        }

        iarr_space[L / 2 + xx][M / 2 + yy][N / 2 + zz] = 1;
return iarr_space[L][M][N];
}
```

Appendix B

Tables of Constants and Reference Materials

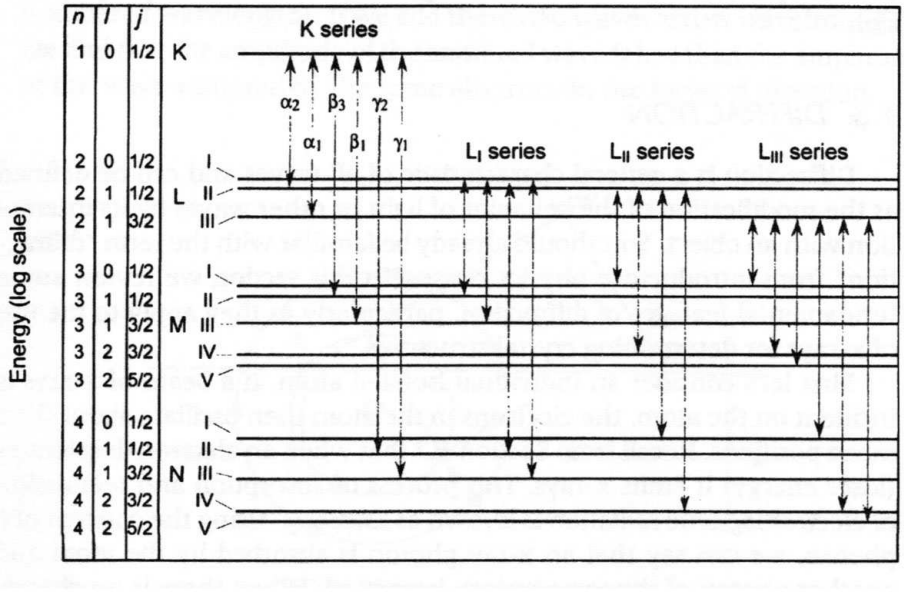

Figure B.1: Energy level diagram showing all allowed electron transitions in a molybdenum atom [99]

Table B.1: Some commonly used X-Ray K wavelengths (in nm) [99]

Element	Kα (weight average)	Kα1 (strong)	Kα2 (very strong)	Kβ (weak)
Cr	0.229100	0.229361	0.228970	0.208487
Fe	0.193736	0.193998	0.193604	0.175661
Co	0.179026	0.179285	0.178897	0.162079
Cu	0.154184	0.154439	0.154056	0.139222
Mo	0.071073	0.071359	0.070930	0.063229

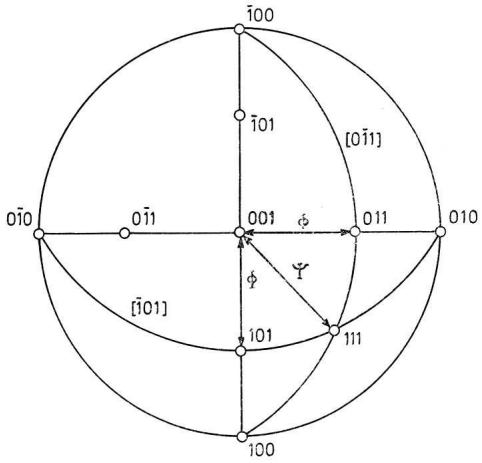

Figure B.2: Stereographic projection for tetragonal crystals showing principal poles and angles [95]

Table B.2: Formulae for determination of interplanar spacings, interplanar angles and interzonal angles [95]

Crystal system	Interplanar spacing of the (hkl) plane	Angle ϕ between $(h_1k_1l_1)$ and $(h_2k_2l_2)$	Angle ρ between $(u_1v_1w_1)$ and $(u_2v_2w_2)$
Cubic $a = b = c$ $\alpha = \beta = \gamma = 90°$	$\frac{1}{d^2} = \frac{1}{a^2}(h^2+k^2+l^2)$	$\cos\phi = \frac{h_1h_2+k_1k_2+l_1l_2}{\sqrt{[(h_1^2+k_1^2+l_1^2)(h_2^2+k_2^2+l_2^2)]}}$	$\cos\rho = \frac{u_1u_2+v_1v_2+w_1w_2}{\sqrt{[(u_1^2+v_1^2+w_1^2)(u_2^2+v_2^2+w_2^2)]}}$
Tetragonal $a = b \neq c$ $\alpha = \beta = \gamma = 90°$	$\frac{1}{d^2} = \frac{1}{a^2}(h^2+k^2)+\frac{1}{c^2}(l^2)$	$\cos\phi = \frac{\frac{1}{a^2}(h_1h_2+k_1k_2)+\frac{1}{c^2}(l_1l_2)}{\sqrt{\left\{\left[\frac{1}{a^2}(h_1^2+k_1^2)+\frac{1}{c^2}l_1^2\right]\left[\frac{1}{a^2}(h_2^2+k_2^2)+\frac{1}{c^2}l_2^2\right]\right\}}}$	$\cos\rho = \frac{a^2(u_1u_2+v_1v_2)+c^2w_1w_2}{\sqrt{\{[a^2(u_1^2+v_1^2)+c^2w_1^2][a^2(u_2^2+v_2^2)+c^2w_2^2]\}}}$
Orthorhombic $a \neq b \neq c$ $\alpha = \beta = \gamma = 90°$	$\frac{1}{d^2} = \frac{1}{a^2}(h^2)+\frac{1}{b^2}(k^2)+\frac{1}{c^2}(l^2)$	$\cos\phi = \frac{\frac{1}{a^2}h_1h_2+\frac{1}{b^2}k_1k_2+\frac{1}{c^2}l_1l_2}{\sqrt{\left[\left(\frac{1}{a^2}h_1^2+\frac{1}{b^2}k_1^2+\frac{1}{c^2}l_1^2\right)\left(\frac{1}{a^2}h_2^2+\frac{1}{b^2}k_2^2+\frac{1}{c^2}l_2^2\right)\right]}}$	$\cos\rho = \frac{a^2u_1u_2+b^2v_1v_2+c^2w_1w_2}{\sqrt{[(a^2u_1^2+b^2v_1^2+c^2w_1^2)(a^2u_2^2+b^2v_2^2+c^2w_2^2)]}}$
Hexagonal $a = b \neq c$ $\alpha = \beta = 90°;\ \gamma = 120°$	$\frac{1}{d^2} = \frac{4}{3a^2}(h^2+hk+k^2)+\frac{1}{c^2}(l^2)$	$\cos\phi = \frac{h_1h_2+k_1k_2+\frac{1}{2}(h_1k_2+k_1h_2)+\frac{3}{4}\frac{a^2}{c^2}l_1l_2}{\sqrt{\left[\left(h_1^2+k_1^2+h_1k_1+\frac{3}{4}\frac{a^2}{c^2}l_1^2\right)\left(h_2^2+k_2^2+h_2k_2+\frac{3}{4}\frac{a^2}{c^2}l_2^2\right)\right]}}$	$\cos\rho = \frac{u_1u_2+v_1v_2-\frac{1}{2}(u_1v_2+v_1u_2)+\frac{c^2}{a^2}w_1w_2}{\sqrt{\left[\left(u_1^2+v_1^2-u_1v_1+\frac{c^2}{a^2}w_1^2\right)\left(u_2^2+v_2^2-u_2v_2+\frac{c^2}{a^2}w_2^2\right)\right]}}$
Rhombohedral $a = b = c$ $\alpha = \beta = \gamma < 120° \neq 90°$	$\frac{1}{d^2} = \frac{1}{a^2}\left\{\frac{(1+\cos\alpha)[(h^2+k^2+l^2)-(1-\tan^2\frac{1}{2}\alpha)(hk+kl+lh)]}{(1+\cos\alpha-2\cos^2\alpha)}\right\}$	Convert to corresponding hexagonal indices (see p. 78) and use the above two formulae.	
Monoclinic $a \neq b \neq c$ $\alpha = \gamma = 90° \neq \beta$	$\frac{1}{d^2} = \frac{1}{a^2}\left(\frac{h^2}{\sin^2\beta}\right)+\frac{1}{b^2}(k^2)+\frac{1}{c^2}\left(\frac{l^2}{\sin^2\beta}\right)-\frac{2hl\cos\beta}{ac\ \sin^2\beta}$	$\cos\phi = \frac{\frac{1}{a^2}h_1h_2+\frac{1}{b^2}k_1k_2\sin^2\beta+\frac{1}{c^2}l_1l_2-\frac{1}{ac}(l_1h_2+l_2h_1)\cos\beta}{\sqrt{\left[\begin{array}{l}\left(\frac{1}{a^2}h_1^2+\frac{1}{b^2}k_1^2\sin^2\beta+\frac{1}{c^2}l_1^2-\frac{2h_1l_1}{ac}\cos\beta\right)\ \times \\ \left(\frac{1}{a^2}h_2^2+\frac{1}{b^2}k_2^2\sin^2\beta+\frac{1}{c^2}l_2^2-\frac{2h_2l_2}{ac}\cos\beta\right)\end{array}\right]}}$	$\cos\rho = \frac{a^2u_1u_2+b^2v_1v_2+c^2w_1w_2+ac(w_1u_2+u_1w_2)\cos\beta}{\sqrt{\left[\begin{array}{l}(a_2u_1^2+b^2v_1^2+c^2w_1^2+2acu_1w_1\cos\beta)\ \times \\ (a^2u_2^2+b^2v_2^2+c^2w_2^2+2acu_2w_2\cos\beta)\end{array}\right]}}$
Triclinic $a \neq b \neq c$ $\alpha \neq \beta \neq \gamma$	$\frac{1}{d^2} = \frac{1}{V^2}\{s_{11}h^2+s_{22}k^2+s_{33}l^2+2s_{12}hk+2s_{23}kl+2s_{31}lh\}$ where $V^2 = a^2b^2c^2(1-\cos^2\alpha-\cos^2\beta-\cos^2\gamma+2\cos\alpha\cos\beta\cos\gamma)$ and $s_{11} = b^2c^2\sin^2\alpha$ $s_{22} = a^2c^2\sin^2\beta$ $s_{33} = a^2b^2\sin^2\gamma$ $s_{12} = abc^2(\cos\alpha\cos\beta-\cos\gamma)$ $s_{23} = a^2bc(\cos\beta\cos\gamma-\cos\alpha)$ $s_{31} = ab^2c(\cos\gamma\cos\alpha-\cos\beta)$	$\cos\phi = \frac{F}{A_{h_1k_1l_1}\cdot A_{h_2k_2l_2}}$ where $F = h_1h_2b^2c^2\sin^2\alpha+k_1k_2a^2c^2\sin^2\beta+l_1l_2a^2b^2\sin^2\gamma$ $+abc^2(\cos\alpha\cos\beta-\cos\gamma)(k_1h_2+h_1k_2)$ $+ab^2c(\cos\gamma\cos\alpha-\cos\beta)(h_1l_2+l_1h_2)$ $+a^2bc(\cos\beta\cos\gamma-\cos\alpha)(k_1l_2+l_1k_2)$ and $A_{hkl} = \sqrt{\left[\begin{array}{l}h^2b^2c^2\sin^2\alpha+k^2a^2c^2\sin^2\beta+l^2a^2b^2\sin^2\gamma \\ +2hkabc^2(\cos\alpha\cos\beta-\cos\gamma) \\ +2hlab^2c(\cos\gamma\cos\alpha-\cos\beta) \\ +2kla^2bc(\cos\beta\cos\gamma-\cos\alpha)\end{array}\right]}$	$\cos\rho = \frac{L}{I_{u_1v_1w_1}\cdot I_{u_2v_2w_2}}$ where $L = a^2u_1u_2+b^2v_1v_2+c^2w_1w_2$ $+bc(v_1w_2+w_1v_2)\cos\alpha$ $+ac(w_1u_2+u_1w_2)\cos\beta$ $+ab(u_1v_2+v_1u_2)\cos\gamma$ and $I_{uvw} = \sqrt{\left[\begin{array}{l}a^2u^2+b^2v^2+c^2w^2 \\ +2bcvw\cos\alpha \\ +2cawu\cos\beta \\ +2abuv\cos\gamma)\end{array}\right]}$

Appendix C

Double Layer Thickness

The double layer thickness is defined by the following equation

$$K^{-1} = \frac{\epsilon k_B T}{\sqrt{2e^2 1000.I_c N_a}} \tag{C.1}$$

where ϵ – Permittivity of Liquid; k_B – Boltzmann's Constant; T – Temperature in Kelvin (K); e – Electronic Charge in Coulombs; I_c – Ionic Strength in units of mol/dm3 (mol/L or M, molar); N_a – Avogadro Number.

The permittivity of the liquid is equal to where ϵ_r, the relative permittivity, is 78.54 for water at 298.15 K. The permittivity of vacuum, ϵ_0, is $8.8542 \times 10^{-12} Fm^{-1}$. The extra factor of 1000 in the denominator converts I_c from mol/dm^3 to mol/m^3. Substituting these values into the equation, one obtains:

$$K^{-1} = 0.3043/\sqrt{I_c} \quad (nm) \tag{C.2}$$

The double layer thickness decreases inversely as the square root of the ionic strength. The ionic strength depends on the concentration of free ions and also on

their charge. For simple salts, the double layer thickness in water at 25 °C as a function of concentration is given in the following table:

Double Layer Thickness in Nanometers

Conc.(M)	10^{-7}	10^{-6}	10^{-5}	10^{-4}	10^{-3}	10^{-2}	10^{-1}
1:1	962	304	96.27	30.4	9.62	73.04	0.962
1:2,2:1	555	176	55.5	17.6	5.55	1.76	0.555
2:2	481	152	48.1	15.2	74.81	1.52	0.481
1:3,3:1	393	124	39.3	12.4	3.93	1.24	0.393
3:3	321	101	32.1	10.1	3.21	1.01	0.321
2:3,3:2	248	78.5	24.8	7.85	2.48	0.785	0.248

Appendix D

Powder Diffraction File Data

Figure D.1: Neighborite ($NaMgF_3$) Power Diffraction Data

PDF Card Info - TracesV6 6

Card Number:	13-0303 CAS Number:
PDF Index Name:	Sodium Magnesium Fluoride
Mineral Name:	Neighborite
Chemical Name:	
Chemical Formula:	Na Mg F3

References

AMMIAY Vol.46, p379 1961 Chao, E., Evans, H., Skinner, B., Milton, C.

Unit Cell			H	K	L	d-Space	Int
Space Group:	Pnma (62)		0	2	0	3.8300	35
Quality Code:	B		1	1	1	3.4400	4
Molecular Weight:	104.29		0	0	2	2.7500	4
Cell Volume:	226.54		1	2	1	2.7100	50
Measured Density:	3.030		2	0	0	2.6800	4
Calc. Density:	3.060		1	0	2	2.4400	4
			2	0	1	2.4100	10
a: 5.363	Alpha:		1	1	2	2.3300	4
b: 7.676	Beta:		2	1	1	2.3000	25
c: 5.503	Gamma:		0	2	2	2.2300	18
			2	2	0	2.2000	14
			1	3	1	2.1300	6
			1	2	2	2.0600	6
Data Collection			2	2	1	2.0400	2
			0	4	0	1.9180	100
Instrument:	Debye-Scherrer		2	1	2	1.8620	4
SS/FOM:	Beta Filter		1	3	2	1.7650	2
Filter:	Ni		1	0	3	1.7320	4
Ref. Int. Ratio:			1	4	1	1.7130	10
Radiation:	CuKa		1	1	3	1.6890	6
Wavelength:	1.5418		3	1	1	1.6610	2
			0	4	2	1.5750	14
			3	2	1	1.5560	25
			2	3	2	1.5300	2
			3	0	2	1.4990	2
			3	1	2	1.4730	2
			1	3	3	1.4340	2
			3	3	1	1.4150	2
			2	2	3	1.4040	2
			0	0	4	1.3710	4
			2	4	2	1.3560	14
			0	5	2	1.3400	2
			1	0	4	1.3270	2
			1	5	2	1.3000	4
			3	0	3	1.2820	4
			4	2	0	1.2680	2
			1	2	4	1.2560	2
			4	2	1	1.2340	2
			2	0	4	1.2200	2
			1	6	1	1.2130	4

Figure D.2: Sellaite (MgF_2) Powder Diffraction Data

Pattern : 01-070-2269

MgF_2

Magnesium Fluoride
Sellaite, syn

Lattice : Tetragonal
S.G. : P42/mnm (136)

a = 4.62800
c = 3.04500

Z = 2

Mol. weight = 62.30
Volume [CD] = 65.22
Dx = 3.173
Dm = 3.150
I/Icor = 1.53

Radiation = 1.540600

d (Å)	*i*	*h*	*k*	*l*
3.27249	999	1	1	0
2.54378	173	1	0	1
2.31400	7	2	0	0
2.22923	767	1	1	1
2.06970	247	2	1	0
1.71173	641	2	1	1
1.63625	234	2	2	0
1.52250	144	0	0	2
1.46350	41	3	1	0
1.44133	18	2	2	1
1.38042	101	1	1	2
1.37614	311	3	0	1
1.31906	42	3	1	1
1.28358	9	3	2	0
1.27189	1	2	0	2
1.22642	40	2	1	2
1.18278	4	3	2	1
1.15700	26	4	0	0
1.12245	30	4	1	0
1.11461	80	2	2	2
1.09083	39	3	3	0

ICSD collection code: 008121
Temperature factor: ATF
Temperature of data collection: REM TEM 27 C.
Additional pattern: See PDF 00-041-1443 and 01-072-1150.
General comments: R(isotropic)=0.024.
Cancel:
Data collection flag: Ambient.

Vidal-Valat, G., Vidal, J.P., Zeyen, C.M.E., Kurki-Suonio, K., Acta Crystallogr., Sec. B, volume 35, page 1584 (1979)
Calculated from ICSD using POWD-12++ (1997)

Radiation : CuKa1
Lambda : 1.54060
SS/FOM : F21=1000(0.0000,21)

Filter : Not specified
d-sp : Calculated spacings

Figure D.3: Galena (PbS) Powder Diffraction Data

```
PDF Card Info - TracesV6 6
~~~~~~~~~~~~~~~~~~~~~~~~~~
     Card Number:  01-0880              CAS Number:
  PDF Index Name:  Lead Sulfide
    Mineral Name:  Galena
   Chemical Name:
Chemical Formula:  Pb S


References
~~~~~~~~~~
ANCHAM  Vol.10, p475  1938 Hanawalt et al.
DANASG  Vol., p


Unit Cell
~~~~~~~~~
     Space Group:  Fm-3m (225)
    Quality Code:  B
Molecular Weight:  239.26
     Cell Volume:  208.53
Measured Density:  7.580
   Calc. Density:

   a:  5.93        Alpha:
   b:               Beta:
   c:              Gamma:
```

H	K	L	d-Space	Int	H
1	1	1	3.4300	80	
2	0	0	2.9700	100	
2	2	0	2.0900	60	
3	1	1	1.7900	32	
2	2	2	1.7100	16	
4	0	0	1.4800	8	
3	3	1	1.3600	8	
4	2	0	1.3300	16	
4	2	2	1.2100	8	
5	1	1	1.1400	8	
4	4	0	1.0500	4	
5	3	1	1.0000	4	

```
Data Collection
~~~~~~~~~~~~~~~
      Instrument:
          SS/FOM:  Beta Filter
          Filter:  ZrO2
 Ref. Int. Ratio:
       Radiation:  MoKa
      Wavelength:  0.709
```

Bibliography

[1] B. Derjaguin and L. Landau. Theory of the stability of strongly charged lyophobic sols and of the adhesion of strongly charged particles in solutions of electrolytes. *Acta Phys. Chim. Sin.*, 14:633, 1941.

[2] E. Barouch, E. Matijević, T.A. Ring, and J.M. Finlan. Heterocoagulation II interaction energy of two unequal spheres. *J. Colloid Interface Sci.*, 67(1):1–9, October 1978.

[3] E. Barouch and E. Matijević. Double-layer interactions of unequal spheres. *J. Chem. SOC., Faraahy Trans.*, 81(I):1797–1817, 1985.

[4] V. Kitaev and G.A. Ozin. Self-assembled surface patterns of binary colloidal crystals. *Adv. Mater.*, 15:75–78, 2003.

[5] J.Y. Lee, G.A. Buxton, and A.C. Balazs. Using nanoparticles to create self-healing composites. *J. Chem. Phys.*, 121:5531–5540, 2004.

[6] T. Sugimoto. *Fine Particles Synthesis, Characterization, and Mechanism of Growth.* Marcel Dekker, New York, 2000.

[7] E. Matijević. Preparation and properties of uniform size colloids. *Chem. Mater.*, 5(4):412–426, 1993.

[8] E. Matijević. Uniform inorganic colloid dispersions. achievements and challenges. *Langmuir*, 10:8–16, 1994.

[9] E. Matijević and D. Goia. Formation mechanisms of uniform colloid particles. *Croat. Chem. Acta*, 80:485–491, 2007.

[10] V.K. LaMer. Nucleation in phase transitions. *Industrial. Eng. Chem*, 44:1270–1277, 1952.

[11] S. Libert, V. Gorshkov, D. Goia, E. Matijević, and V. Privman. Model of controlled synthesis of uniform colloid particles: Cadmium sulfide. *Langmuir*, 19(26):10679–10683, 2003.

[12] V. Privman, D.V. Goia, J. Park, and E. Matijević. Mechanism of formation of monodispersed colloids by aggregation of nanosize precursors. *J. Colloid Interface Sci.*, 213:36–45, 1999.

[13] Z.A. Peng and X. Peng. Nearly monodispersed and shape-controlled cdse nanocrystals via alternative routes: Nucleation and growth. *J. Am. Chem. Soc.*, 124:3343–3353, 2002.

[14] J.H. Jean and T.A. Ring. Nucleation and growth of monosized ti02 powders from alcohol solution. *Langmuir*, 2:251–255, 1986.

[15] Z. Orel, E. Matijević, and D.V. Goia. Precipitation and recrystallization of uniform cucl particles formed by aggregation of nanosize precursors. *Colloid Polym. Sci.*, 281:754–759, 2003.

[16] T.S. Ahmadi, Z.L. Wang, and Henglein A. Green, T.C., and M.A. EI-Sayed. Shape-controlled synthesis of colloidal platinum nanoparticles. *Science*, 272:1924–1925, 1996.

[17] T. Teranishi and M. Miyake. Size control of palladium nanoparticles and their crystal structures. *Chem. Mater.*, 10:594–600, 1998.

[18] D.V. Goia and E. Matijević. Tailoring the particle size of monodispersed colloidal gold. *Colloids Surf., A*, 146:139–152, 1999.

[19] M.P. Morales, T. Gonzalez-Carreno, and C.J. Serna. The formation of alphafe2o3 monodispersed particles in solution. *J. Mater. Res.*, 7:2538, 1996.

[20] D. Martin, W.A. Crichton, et al. Phase transitions and compressibility of namgf$_3$ (neighborite) in perovskite- and post-perovskite-related structures. *Geophys. Research Let.*, 33:L11305, 2006.

[21] I. Sondi, O. Siiman, S. Koester, and E. Matijević. Preparation of aminodextran-cds nanoparticle complexes and biologically active antibody-aminodextran-cds nanoparticle conjugates. *Langmuir*, 16:3107–3118, 2000.

[22] F. Celestin. Diffusion of a liquid nanoparticle on a disordered substrate. *arXiv:condmat/ 0406625, 1, 25*, 2004.

[23] R. Lee Penn and J.F. Banfield. Morphology development and crystal growth in nanocrystalline aggregates under hydrothermal conditions: Insights from titania. *Geoch. Et Cosm. Acia*, 63:1549, 1999.

[24] R. Lee Penn and J.F. Banfield. Imperfect oriented attachment: Dislocation generation in defect-free nanocrystals. *Science*, 281:970, 1998.

[25] J.J. De Yoreo and P.M. Dove. Shaping crystals with biomolecules. *Science*, 306:1301, 2004.

[26] H.S. Shin, H.J. Yang, S.B. Kim, and M.S. Leeb. Mechanism of growth of colloidal silver nanoparticles stabilized polyvinyl pyrrolidone in irradiated silver nitrate solution. *J. Colloid Interface Sci.*, 274, 2004.

[27] B.J. McCoy. A new population balance model for crystal size distributions: Reversible, size-dependent growth and dissolution. *J. Colloid Interface Sci.*, 240:139–149, 2001.

[28] V.V. Slezov, J. Schmelzer, and Ya.Y. Tkatch. Number of clusters formed in nucleation-growth processes. *J. Chem. Phys.*, 105:8340–8351, 1996.

[29] T. Sugimoto. The theory of the nucleation of monodisperse particles in open systems and its application to agbr systems. *J. Colloid Interface Sci.*, 150:208–225, 1992.

[30] V. Privman, Doering, and Frisch. Crossover from rate-equation to diffusion-controlled kinetics in two-particle coagulation. *Phys Rev. E*, 48:846–851, 1993.

[31] I. Sevonkaev and V. Privman. Shape selection in synthesis of colloids and nanoparticles. *Proc. Conf.*, ICCM-17:909–910, 2009.

[32] D. Ouden and R. Thompson. Analysis of the formation of monodispersed populations by homogeneous nucleation. *J. Colloid Interface Sci.*, 143:77–84, 1991.

[33] N. Sasaki, Y. Murakami, D. Shindo, and T. Sugimoto. Computer simulations for the growth process of peanut-type hematite particles. *J. Colloid Interface Sci.*, 213:121–125, 1999.

[34] J.D. Shore and D. Perchak. Simulations of the nucleation of agbr from solution. *J. Chem. Phys.*, 113:6276–6284, 2000.

[35] J.F. Banfield, S.A. Welch, and H. Zhang. Aggregation-based crystal growth and microstructure development in natural iron oxyhydroxide biomineralization products. *Science*, 289:751–754, 2000.

[36] M.P. Morales, M. Ocana, and C.J. Serna. The growth mechanism of alphafe2o3 ellipsoidal particles in solution. *J. Colloid Inerface Sci.*, 171:85–91, 1995.

[37] J.K. Bailey, C.J. Brinkor, and M.L. Mecartney. Growth mechanisms of iron oxide particles of differing morphologies from the forced hydrolysis of ferric chloride solutions. *J. Colloid Interface Sci.*, 157:1–13, 1993.

[38] S. Kratohvil and E. Matijević. Preparation of copper compounds of different compositions and particle morphologies. *J. Mater. Res.*, 6:766–777, 1991.

[39] P. Botella, A. Corma, and M. T. Navarro. Single gold nanoparticles encapsulated in monodispersed regular spheres of mesostructured silica produced by pseudomorphic transformation. *Chem. Mater.*, 19(8):1979–1983, 2007.

[40] P. H. C. Camargo, Z. Y. Li, and Y. Xia. Colloidal building blocks with potential for magnetically configurable photonic crystals. *Soft Matter*, 3(10):1215–1222, 2007.

[41] Y. S. Cho, G. R. Yi, Y. S. Chung, S. Bin Park, and S. M. Yang. Complex colloidal microclusters from aerosol droplets. *Langmuir*, 23(24):12079–12085, 2007.

[42] Y. W. Chung, I. C. Leu, J. H. Lee, and M. H. Hon. Fabrication and characterization of core-shell photonic crystals via a dipping process. *Colloids Surf. A*, 290(1–3):256–262, 2006.

[43] J. L. Elechiguerra, L. Larios-Lopez, and M. Jose-Yacaman. Controlled synthesis of platinum submicron and nanometric particles with novel shapes. *Appl. Phys. A*, 84(1–2):11–19, 2006.

[44] W. H. Huang, J. A. Li, L. J. Xue, R. B. Xing, S. F. Luan, C. X. Luo, L. B. Liu, and Y. C. Han. Complex aggregates of spherical colloids via modified micromolding in capillaries. *Colloids Surf. A*, 278(1–3):144–148, 2006.

[45] Y. L. Luo. Formation of submicrometer-scale gold nanoparticle aggregates and their self-organization into "supracrystals". *Colloid J.*, 69(3):391–393, 2007. Luo, Yonglan.

[46] T. Nakamura, Y. Yamada, and K. Yano. Novel synthesis of highly monodispersed gamma-fe2o3/sio2 and epsilon fe2o3/sio2 nanocomposite spheres. *J. Mater. Chem.*, 16(25):2417–2419, 2006.

[47] H. L. Nguyen, L. E. M. Howard, S. R. Giblin, B. K. Tanner, I. Terry, A. K. Hughes, I. M. Ross, A. Serres, H. Burckstummer, and J. S. O. Evans. Synthesis of monodispersed fcc and fct fept/fepd nanoparticles by microwave irradiation. *J. Mater. Chem.*, 15(48):5136–5143, 2005.

[48] S. K. Panda, A. Datta, and S. Chaudhuri. Nearly monodispersed zns nanospheres: Synthesis and optical properties. *Chem. Phys. Lett.*, 440(4–6):235–238, 2007.

[49] V. K. Tzitzios, V. Georgakilas, D. Niarchos, and D. Petridis. Synthesis and characterization of monodispersed rhodium nanoparticles organized in 3-d symmetrical structures soluble in organic media. *J. Nanosci. Nanotechnol.*, 6(7):2081–2083, 2006.

[50] H. H. Wang, C. S. Xie, D. W. Zeng, and Z. H. Yang. Controlled organization of zno building blocks into complex nanostructures. *J. Colloid Interface Sci.*, 297(2):570–577, 2006.

[51] D. W. Wyrwa and G. Schmid. Metal nanoparticles on stainless steel surfaces as novel heterogeneous catalysts. *J. Cluster Sci.*, 18(3):476–493, 2007.

[52] H. Z. Zhong, Z. X. Wei, M. F. Ye, Y. Yan, Y. Zhou, Y. Q. Ding, C. H. Yang, and Y. F. Li. Monodispersed znse colloidal microspheres: Preparation, characterization, and their 2d arrays. *Langmuir*, 23(17):9008–9013, 2007.

[53] Y. F. Zhu, W. R. Zhao, H. R. Chen, and J. L. Shi. A simple one-pot self-assembly route to nanoporous and monodispersed fe3o4 particles with oriented attachment structure and magnetic property. *J. Phys. Chem. C*, 111(14):5281–5285, 2007.

[54] J. Park, V. Privman, and E. Matijević. Model of formation of monodispersed colloids. *J. Phys. Chem. B*, 105:11630–11635, 2001.

[55] E. Matijević. Nanosize precursors as building blocks for monodispersed colloids. *Colloid J.*, 69(1):29–38, February 2007.

[56] S. Libert, V. Gorshkov, V. Privman, D. Goia, and E. Matijević. *LANL Preprint Archive, Cond. Matter*, pages 1–18, 2002.

[57] S. Libert, D. Goia, and E. Matijević. Internally composite uniform colloidal cadmium sulfide spheres. *Langmuir*, 19(26):10673–10678, 2003.

[58] A.K. Misra. *J. Electrochem. Soc.*, 135:650, 1988.

[59] Y. Takahashi, A. Negishi, Y. Abe, K. Tanaka, and M. Kamimoto. *Phermochim. Acta*, 183:299, 1991.

[60] A.K. Misra and J.D. Whittenberger. *Proc. Intersociety Energy Conversion Engineering Conference*, 1:188, 1987.

[61] J.W. Mullin. *Crystallization*. Elsevier, New York, 2004.

[62] Alan G. Walton. *The Formation and Properties of Precipitates*. Interscience Publishers, 1967.

[63] Arne E. Nielsen. *Kinetics of Precipitation*. The MacMillan Company, 1964.

[64] V. Privman. Diffusional nucleation of nanocrystals and their self-assembly into uniform colloids. *J. Optoelectronics Adv. Mater.*, 10:2827–2839, 2008.

[65] V. Gorshkov, A. Zavalov, and V. Privman. Shape selection in diffusive growth of colloids and nanoparticles. *Langmuir*, 25:7940–7953, 2009.

[66] I. Sevonkaev, D. Goia, and E. Matijević. Formation and structure of cubic particles of sodium magnesium fluoride (neighborite). *J. Colloid Interface Sci.*, 317(1):130–136, 2008.

[67] I. Sevonkaev and E. Matijević. Formation of magnesium fluoride particles of different morphologies. *Langmuir*, 25 (18)(?):10534–10539, 2009.

[68] B. Gilbert, F. Huang, H.Z. Zhang, G.A. Waychunas, and J.F. Banfield. *Science*, 305:651, 2004.

[69] A.P. Alivisatos. Semiconductor clusters, nanocrystals, and quantum dots. *Science*, 271:933–937, 1996.

[70] D.J. Burleson and R.L. Penn. Two-step growth of goethite from ferrihydrite. *Langmuir*, 22:402–409, 2006.

[71] D. Robb and V. Privman. Model of nanocrystal formation in solution by burst nucleation and diffusional growth. *Langmuir*, 24:26–35, 2008.

[72] D. T. Robb, I. Halaciuga, V. Privman, and D. V. Goia. Computational model for the formation of uniform silver spheres by aggregation of nanosize precursors. *J. Chem. Phys.*, 129(18), 2008.

[73] C. N. Nanev. On the slow kinetics of protein crystallization. *Cryst. Growth Des.*, 7(8):1533–1540, 2007.

[74] A. Barnard, H. Xu, X. Li, N. Pradhan, and X. Peng. Modelling the formation of high aspect cdse quantum wires: axial-growth versus oriented-attachment mechanisms. *Nanotechnology*, 17(22):5707–5714, 2006.

[75] S. Libert, V. Gorshkov, V. Privman, D.V. Goia, and E. Matijević. Formation of monodispersed cadmium sulfide particles by aggregation of nanosize precursors. *Adv. Colloid. Interface Sci.*, 100:169–183, 2003.

[76] V. Privman. Growth of nanosize and colloid particles by controlled addition of singlets. *Mater. Res. Soc. Symp. Proc.*, 703:577–585, 2002.

[77] D. Horn and J. Rieger. Organic nanoparticles in the aqueous phase-theory, experiment, and use. *Angewandte Chemie International Edition*, 40(23):4330–4361, 2001.

[78] T. Sugimoto. *Monodispersed Particles*. Elsevier, New York, 2001.

[79] J. Park and V. Privman. Growth of monodispersed colloids by aggregation of nucleating subunits. *Rec. Res. Dev. Stat. Phys.*, 1:1–17, 2000.

[80] V. Privman and J. Park. *Processing by Centrifugation, Proceedings of the Fourth International Workshop on Materials Processing at High Gravity: New York*, 1, 2001.

[81] W. B. Russel, D. A. Saville, and W. R. Schowalter. *Colloidal Dispersions; Cambridge University Press: Oxford, U.K.*, 1989.

[82] D. Mozyrsky and V. Privman. Diffusional growth of colloids. *J. Chem. Phys*, 110:9254–9258, 1999.

[83] G. Schmid. Large clusters and colloids. metals in the embryonic state. *Chem. Rev.*, 92(8):1709–1727, 1992.

[84] J. A. Dirksen, S. Benjelloun, and T. A. Ring. Precipitation of monosized spherical copper oxalate aggregates. *Colloid Polymer Sci*, 268:864–876, 1990.

[85] J.A. Dirksen and T.A. Ring. Fundamentals of crystallization: Kinetic effects on particle size distributions and morphology. *Chem. Eng. Sci.*, 46(10):2389–2427, 1991.

[86] D. Knuth. *The art of computer programming.* 2 [2ed.], AW, 1981.

[87] J. Farjoun. *Nucleation, Growth, and Coarsening A Global View on Aggregation.* PhD thesis, University of California at Berkeley, 2006.

[88] D.A. Barlowa, J.K. Bairda, and C. Su. Theory of the von weimarn rules governing the average size of crystals precipitated from a supersaturated solution. *J. Crystal Growth*, 264:417–423, 2004.

[89] J. B. Zeldovich. On the theory of new phase formation; cavitation. *Acta Physiochim, USSR*, 18:1–22, 1943.

[90] W.P. Hsu, Q. Zhong, and E. Matijević. The formation of uniform colloidal particles of magnesium fluoride and sodium magnesium fluoride. *J. Colloid Interface Sci.*, 181:142–148, 1996.

[91] B.M. Wilhemly and E. Matijević. Preparation of uniform colloidal particles of lead sulfide and of mixed sulfides of cadmium + zinc and cadmium + lead. *Colloids Surf.*, 16:1–8, 1985.

[92] D.J. O'Connor, B.A. Sexton, and R.C. Smart. *Surface Analysis Methods in Material Science*. Springer, 2003.

[93] B. Fultz and J.M. Howe. *Transmission Electron Microscopy and Diffractometry of Materials*. Springer, 2nd ed. edition, 2002.

[94] Shindo Daisuke and Oikawa Tetsuo. *Analytical Electron Microscopy for Materials Science*. Springer, 2002.

[95] K.W. Andrews, D. Phil, and S.R. Keown. *Interpretation of Electron Diffraction Patterns*. Plenum Press, New York, 1967.

[96] J.I. Goldstein, D.E. Newbury, P. Echlin, D.C. Joy, C. Fiori, and E. Lifshin. *Scanning Electron Microscopy and X-ray Microanalysis*. Plenum, New York, 1981.

[97] L. Reimer. *Scanning Electron Microscopy (2nd Ed.)*. Springer.

[98] J.L. Pouchou and F. Pichoir. *Scanning Microscopy*, 212(12), 1990.

[99] C. Suryanarayana and M. Grant Norton. *X-Ray Diffraction a Practical Approach*. Plenum Press, 1998.

[100] P. Scherrer. *Kolloidchemie (3rd Ed. 1920)*. Gottinger Nachrichten, 1918.

[101] B. Chu. *Laser light scattering.* Academic Press, New York, 1974.

[102] B. Berne and R. Pecora. *Dynamic light scattering with applications to chemistry, biology and physics.* Wiley-Interscience, New York, 1976.

[103] H. Dhadwal, R. Ansari, and W. Meyer. A fiber optic probe for particle sizing in concentrated suspensions. *Rev. Sci. Instruments*, 12(62):2963, 1991.

[104] H. Dhadwal and et al. *Proc. S.P.I.E.*, 16:1884, 1993.

[105] E.H Swift and A. Butler. Precipitation of sulfides from homogeneous solutions by thioacetamide. *J. Anal. Chem.*, 28(2):146–153, 1956.

[106] R.C. Weast. *Handbook of Chemistry and Physics.* The Cmemical Rubber Co., 1968.

[107] E. Rudzitis, H.M. Feder, and W.N. Hubbard. Fluorine bomb calorimetry. ix. the enthalpy of formation of magnesium difluoride. *J. Phys. Chem*, 68:2978–2981, 1964.

[108] L. Topor, A. Navrotsky, Y. Zhao, and D.J. Weidner. Thermochemistry of fluoride perovskites: Heat capacity, enthalpy of formation, and phase transition of namgf$_3$. *J. Solid State CHEM.*, 132:131–138, 1997.

[109] V. V. Dolivo-Dobrovolski. Tetragonal packings of spheres. *Crystallogr. Reports*, 47:723–726, 2002.

[110] S.V. Ostanova, A.V. Chubarov, S.V. Drozdov, V.V. Patrushev, and A.A. Tatarenko. Solubility of lead nitrate in aqueous solutions of nitric acid and zinc nitrate. *Russian Journal of Applied Chemistry*, 75:1024–1025(2), June 2002.

[111] R. Shuttleworth. The surface tension of solids. *Proc. Phys. Soc. London, Sect. A*, 63(5):444–457, 1950.

[112] M. M. Nicolson. Surface tension in ionic crystals. *Proceedings of the Royal Society of London. Series A, Mathematical and Physical Sciences (1934-1990)*, 228(1175):490–510, 1955.

[113] A. M. Stoneham. Measurement of surface tension by lattice parameter changes: theory for faceted microcrystals. *J. Phys. C: Solid State Phys.*, 10(8):1175–1179, 1977.

[114] J. Haines, J. M. L'eger, F. Gorelli, D. D. Klug, J. S. Tse, and Z. Q. Li. X-ray diffraction and theoretical studies of the high-pressure structures and phase transitions in magnesium fluoride. *Phys. Rev. B*, 64(13):134110, 2001.

[115] G. Vidal-Valat, J.-P. Vidal, C. M. E. Zeyen, and K. Kurki-Suonio. Neutron diffraction study of magnesium fluoride single crystals. *Acta Crystallogr., Sect. B: Struct. Sci*, 35(7):1584–1590, 1979.

[116] I. Sevonkaev, I. Halaciugaa, D.V. Goia, and E. Matijević. Distribution of density in spherical colloidal particles by transmission electron microscopy. *Colloids Surf., A*, in press:doi:10.1016/j.colsurfa.2009.05.013, 2009.

[117] W. Stöber, A. Fink, and E. Bohn. Controlled growth of monodisperse silica spheres in the micron size range. *J. Colloid Interface Sci.*, 26:62, 1968.

[118] I. Halaciuga and D.V. Goia. Preparation of silver spheres by aggregation of nanosize subunits. *J. Mater. Res.*, 26(6):1776–1784, 2008.

[119] Dale O. Kipp. *Plastic Material Data Sheets*. MatWeb - Division of Automation Creation, Inc., 2004.

[120] M.D. Abramoff, P.J. Magelhaes, and S.J. Ram. Image processing with imagej. *Biophotonics Inter.*, 11(7):36–42, 2004.

[121] W.S. Rasband. Imagej. *U. S. National Institutes of Health, Bethesda, Maryland, USA, http://rsb.info.nih.gov/ij/*, 1997–2007.

[122] V. A. Fok. Fresnel diffraction from convex bodies. *Uspekhi Fizicheskikh Nauk*, 43(4):587–599, 1950.

[123] E. Matijević. Nanosize precursors as building blocks for monodispersed colloids. *Colloid J.*, 69(1):29–39, 2007.